The Dissertation Committee for Mingfeng Wu
certifies that this is the approved version of the following dissertation:

MULTIPLE-GRID ADAPTIVE INTEGRAL METHOD FOR GENERAL MULTI-REGION PROBLEMS

Committee:

Ali E. Yılmaz, Supervisor

Hao Ling

John Pearce

Andrea Alu

Lexing Ying

MULTIPLE-GRID ADAPTIVE INTEGRAL METHOD FOR GENERAL MULTI-REGION PROBLEMS

by

Mingfeng Wu, M.E.; B.E.

Dissertation

Presented to the Faculty of the Graduate School of
The University of Texas at Austin
in Partial Fulfillment
of the Requirements
for the Degree of

Doctor of Philosophy

The University of Texas at Austin
August 2011

Dedicated to Mom, Dad, and Brother

Acknowledgements

I would like to thank my supervisor, Dr. Ali E. Yılmaz. His profound knowledge of physics and mathematics and his enthusiasm in research have inspired me and broadened my vision. During the past four years, he provided invaluable guidance, mentorship, and constant support. It has been a pleasant journey learning from and working with him.

I would also like to thank the members of my doctoral committee, Dr. Hao Ling, Dr. John Pearce, Dr. Andrea Alu, and Dr. Lexing Ying for their time, effort, and insightful suggestions.

A special thanks to all of my colleagues in the Electromagnetics and Acoustics track, especially Fangzhou (Max) Wei, Kai Yang, Guneet Kaur, Vivek Subramanian, and Tahir Malas. I would especially like to thank Yang Li and Xing-Xiang Liu for many helpful technical discussions and substantial collaborations. My studies at the University of Texas at Austin were enriched immeasurably by the friendship and technical knowledge of my colleagues.

I also wish to thank many friends and colleagues outside of the track who provided so much support and encouragement over the years. There are too many to name them all; however, I would like to acknowledge my friends: Xuan Guan, Xiaoxiao Gao, Ling Huang, Wenyuan Li, Xiang Li, Yumin Li, Ligang Long, Zhan Shi, Wenhao Wang, Xiaoxiao Wang, Fei Yan, and Zhixing Zhang.

Finally, I would like to express my deepest gratitude to my parents and brother for their constant love, understanding, encouragement, and support.

MULTIPLE-GRID ADAPTIVE INTEGRAL METHOD FOR GENERAL MULTI-REGION PROBLEMS

Mingfeng Wu, Ph.D.
The University of Texas at Austin, 2011

Supervisor: Ali E. Yılmaz

Efficient electromagnetic solvers based on surface integral equations (SIEs) are developed for the analysis of scattering from large-scale and complex composite structures that consist of piecewise homogeneous magnetodielectric and perfect electrically/magnetically conducting (PEC/PMC) regions. First, a multiple-grid extension of the adaptive integral method (AIM) is presented for multi-region problems. The proposed method accelerates the iterative method-of-moments solution of the pertinent SIEs by employing multiple auxiliary Cartesian grids: If the structure of interest is composed of K homogeneous regions, it introduces K different auxiliary grids. It uses the k^{th} auxiliary grid first to determine near-zones for the basis functions and then to execute AIM projection/anterpolation, propagation, interpolation, and near-zone pre-correction stages in the k^{th} region. Thus, the AIM stages are executed a total of K times using different grids and different groups of basis functions. The proposed multiple-grid AIM scheme requires a total of $O(N^{\mathrm{nz,near}} + \sum_k N_k^{\mathrm{C}} \log N_k^{\mathrm{C}})$ operations per iteration, where $N^{\mathrm{nz,near}}$ denotes the total number of near-zone interactions in all regions and N_k^{C} denotes the number of nodes of the k^{th} Cartesian grid. Numerical results validate the method's accuracy and reduced complexity for large-scale canonical structures with large numbers of regions (up to $\sim 10^6$ degrees of freedom and $\sim 10^3$

regions). Then, a Green function modification approach and a scheme of Hankel- to Teoplitz-matrix conversions are efficiently incorporated to the multiple-grid AIM method to account for a PEC/PMC plane. Theoretical analysis and numerical examples show that, compared to a brute-force imaging scheme, the Green function modification approach reduces the simulation time and memory requirement by a factor of (almost) two or larger if the structure of interest is terminated on or resides above the plane, respectively. In addition, the SIEs are extended to cover structures composed of metamaterial regions, PEC regions, and PEC-material junctions. Moreover, recently introduced well-conditioned SIEs are adopted to achieve faster iterative solver convergence. Comprehensive numerical tests are performed to evaluate the accuracy, computational complexity, and convergence of the novel formulation which is shown to significantly reduce the number of iterations and the overall computational work. Lastly, the efficiency and capabilities of the proposed solvers are demonstrated by solving complex scattering problems, specifically those pertinent to analysis of wave propagation in natural forested environments, the design of metamaterials, and the application of metamaterials to radar cross section reduction.

Table of Contents

List of Tables

List of Figures

Chapter I Introduction

Many wave propagation and antenna radiation applications require efficient analysis of scattering from electrically large composite structures consisting of piecewise homogeneous and perfect electrically/magnetically conducting (PEC/PMC) regions. Consider two examples: (i) To generate models for high fidelity high-frequency (HF) communication channels in forest environments, multiple scattering effects from hundreds to thousands of trees, whose trunks and branches can be modeled as homogeneous dielectric regions, need to be evaluated [1]. (ii) To engineer radar absorbing materials, scattering from complex PEC targets covered by a wide variety/shape of materials, including materials with magnetic losses [2] and metamaterials [3] with negative constitutive parameters, must be evaluated. While scattering from such complex structures can be analyzed using a variety of computational electromagnetics methods [4], those based on surface integral equation (SIE) formulations have appealing properties for large-scale analysis: Unlike volume integral- or differential-equation formulations, SIE formulations result in a smaller set of equations for fewer (surface-bound) unknowns and are essentially dispersion-free as they propagate fields using closed-form Green functions with correct phase velocities (as opposed to using a free-space Green function or a computational grid).

The most popular SIE formulation for analyzing scattering from piecewise homogeneous structures is the Poggio-Miller-Chang-Harrington-Wu-Tsai (PMCHWT) formulation [5-7] that generates a series of equivalent problems by introducing electric and magnetic currents on the surfaces of homogeneous regions, constructs tangential electric- and magnetic-field integral equations (T-EFIEs and T-MFIEs) for each equivalent problem, and linearly combines T-EFIEs and T-MFIEs for different problems to formulate a set of equations for the unknown surface currents. If the currents are discretized by N basis functions and the SIEs are weighted by N testing functions then the classical iterative method-of-moments (MOM) solution can require $O(N^2)$ operations per iteration for special cases, e.g., for a PEC structure (a one-region problem) or for a homogeneous structure (a two-region problem). For general multi-region problems, however, the MOM solution involves sparse matrices with N^{nz} non-zero entries and requires $O(N^{\mathrm{nz}})$ operations per iteration (the null entries correspond to basis-testing function pairs on surfaces that do not bound a common region)—in general $N^{\mathrm{nz}} < N^2$ and for some structures $N^{\mathrm{nz}} \ll N^2$ (see Section 2.1.5 for examples). Despite the sparsity of the resulting matrices, the classical MOM solution of the PMCHWT equations is limited to the analysis of small and simple structures composed of a few regions; this is because (i) its computational complexity scales unfavorably with the electrical size, geometrical complexity, and number of regions of the structure of interest (see Section 2.1.3 for a detailed accounting of the MOM computational cost) and (ii) the system of equations suffers from poor conditioning, which results in slow convergence of iterative solvers.

To reduce the computational complexity of the MOM solution, this dissertation presents a fast Fourier transform (FFT)-based method for multi-region problems that is a natural generalization of the adaptive integral method (AIM) for the one-region problem [8]. The one-region AIM scheme encloses a PEC structure of interest with an auxiliary three-dimensional Cartesian grid of N^{C} nodes, identifies the $N^{\mathrm{nz,near}}$ testing-basis function pairs that are in the near-zone of each other, and executes grid-based projection, propagation, interpolation, and near-zone pre-correction stages. In the propagation stage, this method results in (three level) block-Toeplitz “propagation matrices” and uses (three dimensional) FFTs to efficiently multiply them with trial vectors at each iteration [8].

Because the projection and interpolation stages involve only $O(N)$ operations and because the propagation stage is accelerated by FFTs, AIM requires $O(N^{\text{nz,near}} + N^{\text{C}} \log N^{\text{C}})$ operations per iteration. The auxiliary grid must be carefully selected for optimizing the AIM performance as there is a trade-off between $N^{\text{nz,near}}$ and N^{C} (the near-zone size is a function of the auxiliary-grid spacing [8]). It is well known that the AIM grid size can be chosen such that $N^{\text{nz,near}} \sim N$ for single-scale (sub- or multi-wavelength) structures devoid of features at multiple length scales and that the smaller the ratio of the volume enclosed by the Cartesian grid to the surface area of the PEC structure, the smaller N^{C} is, e.g., $N^{\text{C}} \sim N^{1.5}$ if the structure is a sphere, $N^{\text{C}} \sim N$ if it is a plate. To successfully generalize AIM to multi-region problems, four complications must be addressed: (i) There are null interactions among basis and testing functions on surfaces that bound different regions. (ii) The SIEs employ different Green functions for regions with different constitutive parameters. (iii) The SIEs must be solved for both electric- and magnetic-current unknowns. (iv) Both EFIE and MFIE type kernels are present. Various multi-region AIM extensions that address complications (ii)-(iv) have been proposed recently [9-12]. These extensions, however, all rely on a single auxiliary Cartesian grid that encloses the entire structure of interest, which limits their appeal for multi-region problems as single-grid AIM schemes cannot overcome complication (i) in general: For a K-region problem, these schemes require $O(N^{\text{nz,near}} + KN^{\text{C}} \log N^{\text{C}})$ operations per iteration; furthermore, for large K, it is seldom possible to ensure that KN^{C} is small *and* $N^{\text{nz,near}} \ll N^{\text{nz}}$ with a single grid. This dissertation proposes a "multiple-grid AIM" that introduces *multiple auxiliary Cartesian grids*; thus, the proposed scheme employs K *grids with different size, location, and spacing* for a K-region problem to execute standard grid-based projection, propagation, interpolation, and near-zone pre-correction stages, i.e., each grid is associated with/optimized for a different homogeneous region. The multiple-grid AIM scheme requires $O(N^{\mathrm{nz,near}}+\sum_k N_k^{\mathrm{C}}\log N_k^{\mathrm{C}})$ operations per iteration, where N_k^{C} denotes the number of nodes of the k^{th} Cartesian grid. The grids can be chosen such that $\sum_k N_k^{\mathrm{C}}$ is small *and* $N^{\mathrm{nz,near}} \ll N^{\mathrm{nz}}$ for various multi-region problems (see Section 2.1.4.2 and Section 2.1.5 for details and exceptions).To address the ill-conditioning problem of the classical PMCHWT formulation, henceforth referred to as the EH-PMCHWT formulation, the recently introduced CC-PMCWHT formulation [13-18] is adopted in this dissertation. The CC-PMCWHT formulation uses the same linear combination as the EH-PMCHWT but for combined-field integral equations (CFIEs) and their rotated versions [19], i.e., for the so-called JCFIEs and MCFIEs [13], rather than for T-EFIEs and T-MFIEs. There are several advantages to adopting this formulation: (i) The iterative MOM solution of CC-PMCHWT equations requires significantly fewer iterations than that of EH-PMCHWT equations with little additional computational cost: Both require the same solution time per iteration and memory space while the former requires twice the matrix fill time because it also constructs rotated and scaled MFIEs and EFIEs (N-MFIEs and N-EFIEs) and adds them to T-EFIEs and T-MFIEs, respectively. (ii) The CC-PMCHWT formulation reduces to the standard CFIE formulation for PEC regions; thus, the treatment of material-PEC junctions [19-22] is straightforward when modeling composite structures. (iii) The CC-PMCHWT formulation is amenable to the proposed multiple-grid AIM acceleration. Indeed, because N-EFIEs and T-EFIEs (N-MFIEs and T-MFIEs) have the same projection and propagation operators, only a small additional cost is paid when the CC-PMCHWT is used: Only the pre-correction and interpolation stages are modified while the projection and propagation stages are unchanged (no additional FFTs are needed); the pre-correction stage requires double the matrix fill time (but the same storage space and the same number of operations per iteration); and the interpolation stage requires double the number of operations and memory.

The rest of this dissertation is organized as follows. Chapter II formulates the EH-PMCHWT equations, their classical MOM solution, and the multiple-grid AIM scheme. Chapter III presents the CC-PMCHWT equations and contrasts their classical and multiple-grid AIM accelerated solutions to those of the EH-PMCHWT ones. Chapter IV shows the application of the developed methods to various large-scale wave propagation and scattering problems.

Chapter II Multiple-Grid AIM for EH-PMCHWT Equations

This chapter presents the multiple-grid AIM acceleration for the iterative MOM solution of EH-PMCHWT equations. First, Section 2.1 presents the method for piecewise homogeneous structures composed of conventional magnetodielectric regions with positive permeability and permittivity. Then, various extensions are presented: Section 2.2 presents efficient incorporation of a PEC/PMC plane. Section 2.3 presents extensions for metamaterial regions with negative permittivity or permeability values. Section 2.4 presents extensions for composite structures that include PEC/PMC regions.

2.1. PIECEWISE HOMOGENEOUS STRUCTURES

In this section, the EH-PMCHWT equations for analyzing scattering from piecewise homogeneous structures are formulated and their solution by the MOM, including junction-resolution issues, is reviewed. Next, the proposed multiple-grid AIM scheme is introduced and its computational complexity and memory requirements are analyzed. Numerical results investigating the accuracy and efficiency of the method for canonical structures conclude the section.

2.1.1. Geometry Description and Notation

Consider a K -region scattering problem (Fig. 2.1.1(a)) that involves a piecewise homogeneous structure comprising $K-1$ volumetric regions (denoted as $R_1,\ldots,R_{K-1}$) residing in free space (denoted as R_0). These regions are bounded by M disjoint surfaces; each disjoint surface is either a closed surface or an open surface that is the intersection of two closed surfaces [1]. Let S_{kl} denote the disjoint surface that separates

---

[1] Open surfaces terminate at junctions of open surfaces; to enclose a region with them, at least two must be stitched together.

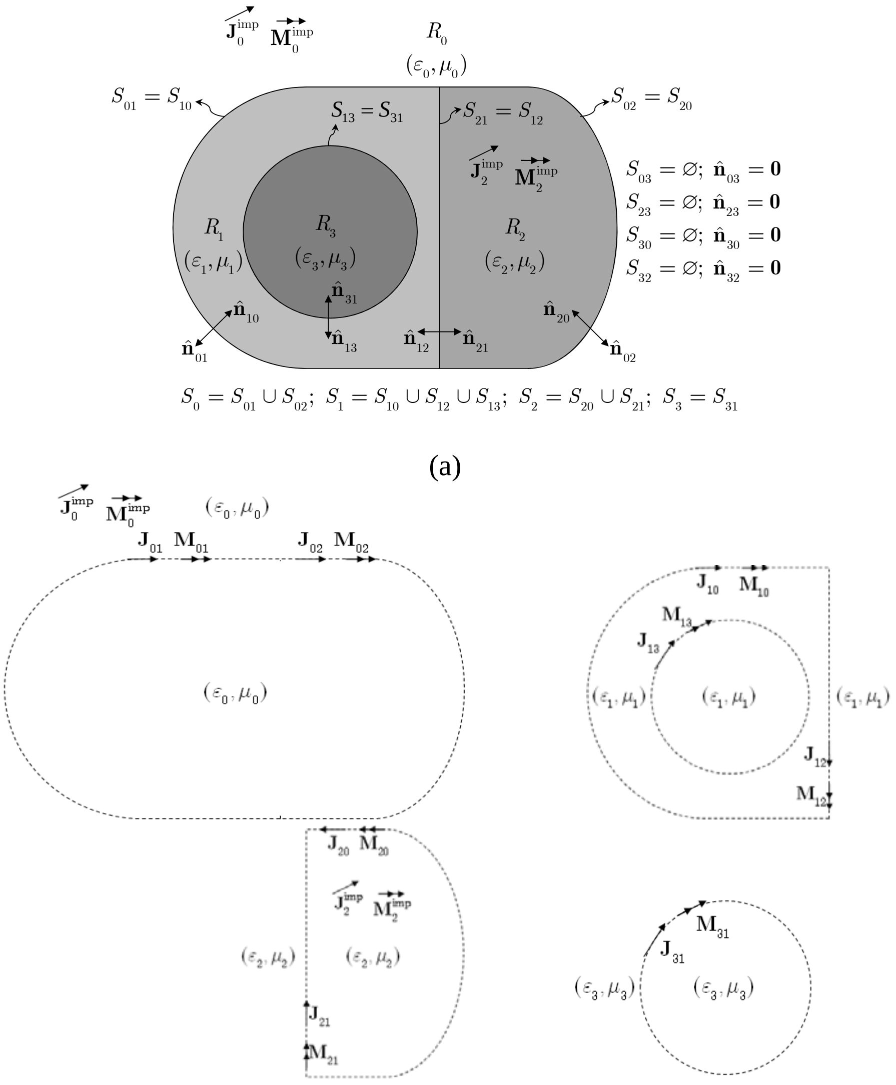

Figure 2.1.1: A sample scattering problem involving a piecewise homogeneous structure with $K=4$ regions and $M=4$ disjoint surfaces ($S_{01},\ S_{02},\ S_{21},\ S_{13}$) illuminated by impressed sources in regions 0 and 2. (a) Definition of regions, disjoint surfaces, and unit normals. (b) The equivalent problems for the fields in regions 0, 1, 2, 3 and the pertinent current densities from top right to bottom right, respectively.

R_k and R_l, i.e., $S_{kl}=S_k\cap S_l$, where S_k and S_l denote the entire boundary surfaces of R_k and R_l, respectively. (Here and throughout the section, unless otherwise stated, $0\le k<K$, $0\le l<K$, and notably $l\neq k$.) Clearly, $S_{lk}=S_{kl}$, $S_k=\bigcup_l S_{kl}$, and if

R_k and R_l do not share a common surface then $S_{kl} = \varnothing$. On each surface S_{kl}, $\hat{\mathbf{n}}_{kl}$ denotes the unit normal that points into R_k and $\hat{\mathbf{p}}_{kl}$ denotes the "preferred" unit normal that is set to either $\hat{\mathbf{n}}_{kl}$ or $\hat{\mathbf{n}}_{lk}$; thus, $\hat{\mathbf{n}}_{lk} = -\hat{\mathbf{n}}_{kl}$ while $\hat{\mathbf{p}}_{lk} = \hat{\mathbf{p}}_{kl}$. The preferred normals will be used to select and identify the unknown currents. It should be noted that $\hat{\mathbf{n}}_{kl} = \hat{\mathbf{p}}_{kl} = \mathbf{0}$ if $S_{kl} = \varnothing$ and that $\hat{\mathbf{n}}_k$ is interpreted as the inward-pointing normal on S_k, i.e., $\hat{\mathbf{n}}_k = \sum_l \hat{\mathbf{n}}_{kl}$.

2.1.2. EH-PMCHWT Formulation

The structure of interest is illuminated by a time-harmonic electromagnetic field due to impressed currents $\{\mathbf{J}_k^{\mathrm{imp}}, \mathbf{M}_k^{\mathrm{imp}}\}$ in R_k ($e^{j\omega t}$ time variation is assumed and suppressed). The pertinent integral equations are derived in four steps. First, K different equivalent problems are formulated: For each problem k, unknown surface currents $\{\mathbf{J}_k, \mathbf{M}_k\} = \{\hat{\mathbf{n}}_k \times \mathbf{H}_k, \mathbf{E}_k \times \hat{\mathbf{n}}_k\}$ are introduced on S_k, where $\{\mathbf{E}_k, \mathbf{H}_k\}$ are the total fields in R_k. This choice of currents yields the true fields inside and zero fields outside R_k; thus, the equivalent problem k reduces to finding $\{\mathbf{J}_k, \mathbf{M}_k\}$ that radiate in an unbounded homogeneous medium with constitutive parameters ε_k and μ_k and sources $\{\mathbf{J}_k^{\mathrm{imp}}, \mathbf{M}_k^{\mathrm{imp}}\}$.

Second, the continuity of tangential fields is enforced on the disjoint surfaces and a subset of the currents in the equivalent problems is identified as follows: Each $\{\mathbf{J}_k, \mathbf{M}_k\}$ is expanded as a sum of the currents on the component surfaces S_{kl} (Fig. 2.1.1(b)) as

$$\{\mathbf{J}_k, \mathbf{M}_k\} = \sum_l \{\mathbf{J}_{kl}, \mathbf{M}_{kl}\}, \tag{2.1.1}$$

where $\{\mathbf{J}_{kl}, \mathbf{M}_{kl}\} = \{\hat{\mathbf{n}}_{kl} \times \mathbf{H}_k, \mathbf{E}_k \times \hat{\mathbf{n}}_{kl}\}$. The currents on the disjoint surfaces are related by the continuity of tangential electromagnetic fields:

$$\{\mathbf{J}_{kl}, \mathbf{M}_{kl}\} = \{-\mathbf{J}_{lk}, -\mathbf{M}_{lk}\} \tag{2.1.2}$$

Thus, integral equations need to be formulated and solved only for a subset of the currents in (2.1.1); these currents will be called "preferred currents" and denoted by $\{\mathbf{J}^p, \mathbf{M}^p\}$:

$$\{\mathbf{J}^p, \mathbf{M}^p\} = \sum_{k=0}^{K-1} \sum_{l=k+1}^{K-1} \{\mathbf{J}_{kl}^p, \mathbf{M}_{kl}^p\}, \tag{2.1.3}$$

where $\{\mathbf{J}_{kl}^p, \mathbf{M}_{kl}^p\} = \{\hat{\mathbf{p}}_{kl} \times \mathbf{H}_k, \mathbf{E}_k \times \hat{\mathbf{p}}_{kl}\}$. The remaining currents can be deduced directly from (2.1.2); the currents on disjoint surfaces are related to the preferred currents as

$$\{\mathbf{J}_{kl}, \mathbf{M}_{kl}\} = \alpha_{kl} \{\mathbf{J}_{kl}^p, \mathbf{M}_{kl}^p\}, \tag{2.1.4}$$

where $\alpha_{kl} = \hat{\mathbf{p}}_{kl} \bullet \hat{\mathbf{n}}_{kl}$.

Third, the fields are decomposed as

$$\{\mathbf{E}_k, \mathbf{H}_k\} = \{\mathbf{E}_k^{\text{inc}}, \mathbf{H}_k^{\text{inc}}\} + \{\mathbf{E}_k^{\text{sca}}, \mathbf{H}_k^{\text{sca}}\}, \tag{2.1.5}$$

where $\{\mathbf{E}_k^{\text{inc}}, \mathbf{H}_k^{\text{inc}}\}$ are the incident fields in R_k due to impressed sources in the same region and $\{\mathbf{E}_k^{\text{sca}}, \mathbf{H}_k^{\text{sca}}\}$ are the scattered fields [23]:

$$\begin{aligned}
\mathbf{E}_k^{\text{sca}}(\mathbf{r}) &= -\eta_k \mathcal{L}_k(\mathbf{J}_k, \mathbf{r}) - \mathcal{K}_k(\mathbf{M}_k, \mathbf{r}) \\
\mathbf{H}_k^{\text{sca}}(\mathbf{r}) &= \mathcal{K}_k(\mathbf{J}_k, \mathbf{r}) - \mathcal{L}_k(\mathbf{M}_k, \mathbf{r}) / \eta_k \\
\mathcal{L}_k\left(\mathbf{v}, \mathbf{r}\right) &= \gamma_k \iint_{S_k} \mathbf{v}(\mathbf{r}') g_k(d) ds' - \frac{\nabla}{\gamma_k} \iint_{S_k} \nabla' \cdot \mathbf{v}(\mathbf{r}') g_k(d) ds' \\
\mathcal{K}_k\left(\mathbf{v}, \mathbf{r}\right) &= \nabla \times \iint_{S_k} \mathbf{v}(\mathbf{r}') g_k(d) ds' \\
g_k\left(d\right) &= e^{-\gamma_k d} / (4\pi d)
\end{aligned} \tag{2.1.6}$$

Here, $\mathbf{v}$ represents either $\mathbf{J}_k$ or $\mathbf{M}_k$ in R_k, $d = \left|\mathbf{r} - \mathbf{r}'\right|$ is the distance between the observer point $\mathbf{r}$ and source point $\mathbf{r}'$, and ε_k, μ_k, $\gamma_k = jw\sqrt{\varepsilon_k \mu_k}$, and $\eta_k = \sqrt{\mu_k / \varepsilon_k}$ are the permittivity, permeability, propagation constant, and intrinsic impedance of region k, respectively.

Fourth, and finally, a tangential electric- and a magnetic-field integral equation (T-EFIE and T-MFIE) are formulated for each surface S_{kl} [5-7]:

$$\begin{aligned} -\hat{\mathbf{n}}_{kl}\times\hat{\mathbf{n}}_{kl}\times\mathbf{E}_k-\hat{\mathbf{n}}_{kl}\times\mathbf{M}_{kl}&=\mathbf{0} \quad (\text{T-EFIE}_{kl}) \\ -\hat{\mathbf{n}}_{kl}\times\hat{\mathbf{n}}_{kl}\times\mathbf{H}_k+\hat{\mathbf{n}}_{kl}\times\mathbf{J}_{kl}&=\mathbf{0} \quad (\text{T-MFIE}_{kl}) \end{aligned} \tag{2.1.7}$$

which are linearly combined following the EH-PMCHWT recipe:

$$\begin{aligned} &\sum_k\sum_l \beta_{kl}\text{T-EFIE}_{kl} \quad (\text{E})\text{PMCHWT} \\ &\sum_k\sum_l \beta_{kl}\text{T-MFIE}_{kl} \quad (\text{H})\text{PMCHWT} \end{aligned} \tag{2.1.8}$$

where $\beta_{kl}=\hat{\mathbf{p}}_{kl}\bullet\hat{\mathbf{n}}_{kl}$.

2.1.3. MOM

Substituting (2.1.1), (2.1.5) and (2.1.6) in (2.1.8) and enforcing (2.1.4) results in a set of integral equations for the preferred currents. These equations are converted to a system of linear equations by the usual MOM steps: The surfaces are meshed, the currents are approximated using RWG [24] and half-RWG [19-22] functions, and the SIEs are weighted by testing functions.

2.1.3.1. Mesh

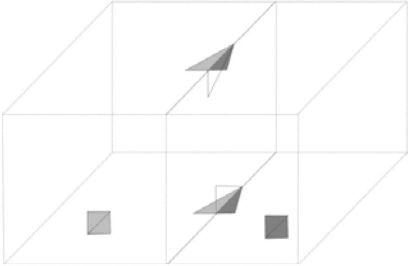

Figure 2.1.2: An example showing regular edges (left and right), which are shared by two patches on the same disjoint surface, and junction edges (top and bottom), which are shared by at least three patches on different disjoint surfaces.

The surfaces of the structure are meshed with triangular patches and each edge on the surface mesh is classified as either a regular edge or a junction edge; a regular edge is shared by two patches on the same disjoint surface whereas a junction edge is shared by at least three patches on different disjoint surfaces (Fig. 2.1.2). Each edge is labeled by a global index as $e_{n'}$, which represents the n'^{th} edge on the entire mesh, and by several local indices as $e_{kl,n}$, which represents the n^{th} edge on the mesh of S_{kl}, i.e., regular edges are assigned two local indices (one for each side of the surface they reside on) and junction edges are assigned at least three local indices (one for each surface that intersects at the junction). It is assumed that there are N_{kl}^{r}, N_{k}^{r}, and N^{r} regular edges and N_{kl}^{j}, N_{k}^{j}, and N^{j} junction edges for a total of N_{kl}, N_{k}, and N edges on the mesh of S_{kl}, S_{k}, and the entire structure, respectively. Obviously, $N_{kl} = 0$ if $S_{kl} = \varnothing$. Moreover, it follows from the definitions that $N_{k}^{r} = \sum_{l} N_{kl}^{r}$, $N^{r} = \sum_{k} N_{k}^{r} / 2$ (regular edges are counted twice: Once for each side of disjoint surfaces); that $N_{k}^{j} = \sum_{l} N_{kl}^{j} / 2$, $N^{j} \le \sum_{k} N_{k}^{j} / 3$ (the equality holds if all junction edges are on junctions of three surfaces); and that $N_{k} \le \sum_{l} N_{kl}$, $N \le \sum_{k} N_{k} / 2$ (the two equalities hold when there are no junctions).

2.1.3.2. Discretization

The discretization procedure is formulated using the local and a global numbering scheme for the edge indices. Using the global notation, the preferred currents are represented as

$$\{\mathbf{J}^{p}(\mathbf{r}), \mathbf{M}^{p}(\mathbf{r})\} \cong \sum_{n'=1}^{N} \{\mathbf{I}[n'], \mathbf{V}[n']\} \mathbf{S}_{n'}(\mathbf{r}) \tag{2.1.9}$$

where $\mathbf{I}$ ($\mathbf{V}$) is an unknown vector of size N; its n'^{th} entry $\mathbf{I}[n']$ ($\mathbf{V}[n']$) represents the electric (magnetic) current coefficient associated with $\mathbf{S}_{n'}$, the basis function assigned to $e_{n'}$. Using the local notation, the preferred currents on S_{kl} are discretized as

$$\{\mathbf{J}_{kl}^{p}(\mathbf{r}), \mathbf{M}_{kl}^{p}(\mathbf{r})\} \cong \sum_{n=1}^{N_{kl}} \{\mathbf{I}_{kl}[n], \mathbf{V}_{kl}[n]\} \mathbf{S}_{kl,n}(\mathbf{r}) \tag{2.1.10}$$

where $\mathbf{I}_{kl}$ ($\mathbf{V}_{kl}$) is an unknown vector of size N_{kl}; its n^{th} entry $\mathbf{I}_{kl}[n]$ ($\mathbf{V}_{kl}[n]$) represents the electric (magnetic) current coefficient associated with $\mathbf{S}_{kl,n}$, the basis function assigned to $e_{kl,n}$.

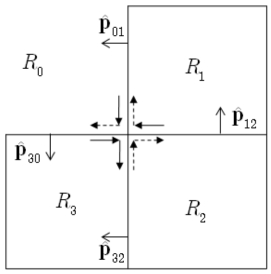

Figure 2.1.3: A consistent choice of directions of half-RWG functions at a junction. Solid and dashed arrows identify the preferred and non-preferred currents at the junction edge.

The global notation in (2.1.9) is related to the local notation in (2.1.10) as follows. If $e_{kl,n} = e_{n'}$ is not a junction edge, then both $\mathbf{S}_{kl,n}$ and $\mathbf{S}_{n'}$ represent the same RWG function [24] defined on the pair of patches that share the edge, i.e., $\mathbf{S}_{kl,n} = \mathbf{S}_{n'}$. If $e_{kl,n} = e_{n'}$ is a junction edge, then $\mathbf{S}_{kl,n}$ represents the half-RWG function defined on the one patch on S_{kl} that shares the edge, whereas $\mathbf{S}_{n'}$ represents the sum of all such half-RWG functions (at least three) that share the junction edge. It should be emphasized that the continuity of currents normal to an edge, which is automatically enforced for non-junction edges by RWG functions, is explicitly enforced for junction edges by assigning the appropriate signs/directions to the half-RWG functions [19-22] (Fig. 2.1.3). Based on the above relation between $\mathbf{S}_{kl,n}$ and $\mathbf{S}_{n'}$, the global and local notations for the unknown current coefficient are related by:

$$\begin{bmatrix} \mathbf{I}_{kl} \\ \mathbf{V}_{kl} \end{bmatrix} = \begin{bmatrix} \mathbf{C}_{kl}\mathbf{I} \\ \mathbf{C}_{kl}\mathbf{V} \end{bmatrix} \tag{2.1.11}$$

where $\mathbf{C}_{kl}$ is a sparse selection-matrix of size $N_{kl} \times N$ that has N_{kl} non-zero entries, i.e., each row n of the matrix has one non-zero entry that is equal to 1; the non-zero entry is at the n'^{th} column if $e_{kl,n} = e_{n'}$.

2.1.3.3. Testing Procedure and Matrix Assembly

Using Galerkin testing, (2.1.7) and (2.1.8) are converted to a matrix equation. On each surface S_{kl}, $\left\langle \mathbf{S}_{kl,n}, \text{T-EFIE}_{kl} \right\rangle$ and $\left\langle \mathbf{S}_{kl,n}, \text{T-MFIE}_{kl} \right\rangle$ are computed for each edge $e_{kl,n}$; these equations are then assembled into a global system of equations according to the EH-PMCHWT recipe in (2.1.8), which results in $2N$ equations for $2N$ unknowns:

$$^{\text{EH}}\mathbf{Z}\begin{bmatrix} \mathbf{I} \\ \mathbf{V} \end{bmatrix} = \begin{bmatrix} ^{\text{EH}}\mathbf{V}^{\text{inc}} \\ ^{\text{EH}}\mathbf{I}^{\text{inc}} \end{bmatrix} \tag{2.1.12}$$

The MOM matrix assembly can be formulated using the local notation as

$$\begin{gathered} ^{\text{EH}}\mathbf{Z} = \sum_k \sum_l \beta_{kl} \begin{bmatrix} \mathbf{C}_{kl}^T & \mathbf{0} \\ \mathbf{0} & \mathbf{C}_{kl}^T \end{bmatrix} {}^{\text{EH}}\mathbf{Z}_{kl} \\ \begin{bmatrix} ^{\text{EH}}\mathbf{V}^{\text{inc}} \\ ^{\text{EH}}\mathbf{I}^{\text{inc}} \end{bmatrix} = \sum_k \sum_l \beta_{kl} \begin{bmatrix} \mathbf{C}_{kl}^T & \mathbf{0} \\ \mathbf{0} & \mathbf{C}_{kl}^T \end{bmatrix} \begin{bmatrix} ^{\text{EH}}\mathbf{V}_{kl}^{\text{inc}} \\ ^{\text{EH}}\mathbf{I}_{kl}^{\text{inc}} \end{bmatrix} \end{gathered} \tag{2.1.13}$$

Clearly,

$$^{\text{EH}}\mathbf{Z}_{kl}\begin{bmatrix} \mathbf{I} \\ \mathbf{V} \end{bmatrix} = \begin{bmatrix} ^{\text{EH}}\mathbf{V}_{kl}^{\text{inc}} \\ ^{\text{EH}}\mathbf{I}_{kl}^{\text{inc}} \end{bmatrix} \tag{2.1.14}$$

The vectors $^{\text{EH}}\mathbf{V}_{kl}^{\text{inc}}$ and $^{\text{EH}}\mathbf{I}_{kl}^{\text{inc}}$, which are of size $N_{kl} \times 1$, store the incident fields tested on surface S_{kl}. The matrix $^{\text{EH}}\mathbf{Z}_{kl}$, which is a sparse $2N_{kl} \times 2N$ matrix with $4N_{kl}N_k$ non-zero entries, relates the scattered fields tested on surface S_{kl} to the currents on the entire structure. It can be expanded as

$$
{}^{\mathrm{EH}}\mathbf{Z}_{kl} = \sum_{l'=0,l'\neq k}^{K-1} \underbrace{\begin{bmatrix} \eta_k \mathbf{L}_{kll'} & \mathbf{K}_{kll'} \\ -\mathbf{K}_{kll'} & \mathbf{L}_{kll'} / \eta_k \end{bmatrix}}_{{}^{\mathrm{EH}}\mathbf{Z}_{kll'}} \alpha_{kl'} \begin{bmatrix} \mathbf{C}_{kl'} & \mathbf{0} \\ \mathbf{0} & \mathbf{C}_{kl'} \end{bmatrix} \tag{2.1.15}
$$

Here, ${}^{\mathrm{EH}}\mathbf{Z}_{kll'}$, which is a $2N_{kl} \times 2N_{kl'}$ dense matrix, relates the scattered fields tested on surface S_{kl} to the currents only on $S_{kl'}$. The entries of ${}^{\mathrm{EH}}\mathbf{Z}_{kll'}$, ${}^{\mathrm{EH}}\mathbf{V}_{kl}^{\mathrm{inc}}$ and ${}^{\mathrm{EH}}\mathbf{I}_{kl}^{\mathrm{inc}}$ can be found in [23] as:

$$
\begin{aligned}
{}^{\mathrm{EH}}\mathbf{V}_{kl}^{\mathrm{inc}}[n] &= \iint_{S_{kl}} \mathbf{S}_{kl,n}(\mathbf{r}) \bullet \mathbf{E}_k^{\mathrm{inc}}(\mathbf{r}) ds \\
{}^{\mathrm{EH}}\mathbf{I}_{kl}^{\mathrm{inc}}[n] &= \iint_{S_{kl}} \mathbf{S}_{kl,n}(\mathbf{r}) \bullet \mathbf{H}_k^{\mathrm{inc}}(\mathbf{r}) ds
\end{aligned} \tag{2.1.16}
$$

$$
\begin{aligned}
\mathbf{L}_{kll'}[n,n'] &= \iint_{S_{kl}} \mathbf{S}_{kl,n}(\mathbf{r}) \bullet \mathcal{L}_k(\mathbf{S}_{kl',n'}, \mathbf{r}) ds \\
&= \gamma_k \iint_{S_{kl}} \iint_{S_{kl'}} \mathbf{S}_{kl,n}(\mathbf{r}) \bullet \mathbf{S}_{kl',n'}(\mathbf{r}') g_k(d) ds' ds \\
&\quad + \frac{1}{\gamma_k} \iint_{S_{kl}} \iint_{S_{kl'}} \nabla \bullet \mathbf{S}_{kl,n}(\mathbf{r}) \nabla' \bullet \mathbf{S}_{kl',n'}(\mathbf{r}') g_k(d) ds' ds \\
\mathbf{K}_{kll'}[n,n'] &= \iint_{S_{kl}} \mathbf{S}_{kl,n}(\mathbf{r}) \bullet \mathcal{K}_k(\mathbf{S}_{kl',n'}, \mathbf{r}) ds \\
&= \iint_{S_{kl}} \mathbf{S}_{kl,n}(\mathbf{r}) \bullet \nabla \times \iint_{S_{kl'}} \mathbf{S}_{kl',n'}(\mathbf{r}') g_k(d) ds' ds
\end{aligned} \tag{2.1.17}
$$

2.1.3.4. Computational Complexity

In marked contrast to the dense MOM matrices that result for one- or two-region problems, the MOM matrix ${}^{\mathrm{EH}}\mathbf{Z}$ for multi-region problems is sparse in general, i.e., $N^{\mathrm{nz}} \leq 4N^2$, where N^{nz} is the number of non-zero entries in ${}^{\mathrm{EH}}\mathbf{Z}$. Indeed, $N^{\mathrm{nz}} = 4\sum_k \sum_{l>k} N_{kl} N_{kl}^{\mathrm{b}}$, where $N_{kl}^{\mathrm{b}} = N_k + N_l - N_{kl}$ is the total number of edges on all surfaces bounding regions R_k and R_l, i.e., fields radiated by the N_{kl} basis functions on the mesh of S_{kl} are observed by N_{kl}^{b} testing functions (via the equivalent problem for either region R_k or region R_l).

Three metrics quantify the computational cost of the MOM solution: The number of operations needed for assembling matrices (the setup cost), the number of operations needed for solving (2.1.12) (the solution cost), and the space needed for storing ${}^{\mathrm{EH}}\mathbf{Z}$ (the memory cost). If an iterative solver that needs ${}^{\mathrm{EH}}N^{\mathrm{I}}$ iterations to converge is used then the setup, solution, and memory costs scale as $O(N^{\mathrm{nz}})$, $O({}^{\mathrm{EH}}N^{\mathrm{I}}N^{\mathrm{nz}})$, and $O(N^{\mathrm{nz}})$, respectively.

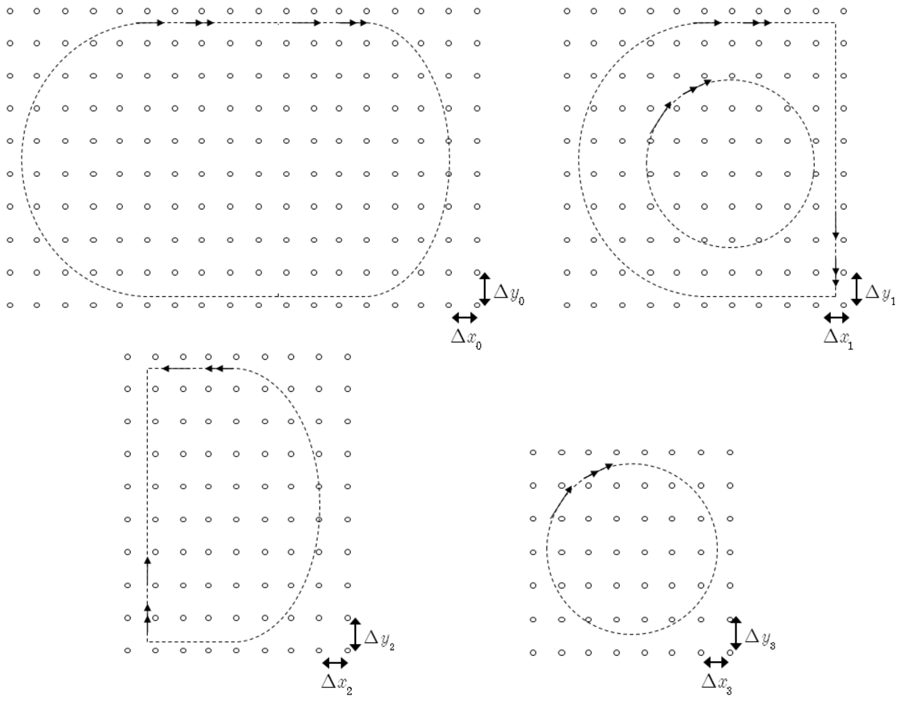

Figure 2.1.4: The multiple auxiliary grids for the structure in Fig. 2.1.2 (z dimension is not shown). The grids used for different equivalent problems have different locations, sizes and spacing.

2.1.4. AIM

Next, the computational cost of the MOM solution is reduced by generalizing the AIM [8] to multi-region problems.

2.1.4.1. Multiple-Grid AIM

Just like the classical (single-grid) AIM, the proposed multiple-grid AIM separates the MOM matrix entries into near-zone and far-zone terms, accelerates far-zone calculations by exploiting the translational invariance of Green functions, and pre-corrects the near-zone calculations by using the original MOM matrix entries. Unlike existing AIM schemes that rely on a single auxiliary grid [9-12], however, the proposed method achieves computational savings by employing multiple auxiliary grids, i.e., it employs K different auxiliary grids $C_0,\ldots,C_{K-1}$ for a K-region problem (Fig. 2.1.4). Each auxiliary grid C_k is a Cartesian grid that encloses S_k (but not necessarily any other surface) and consists of N_k^{C} nodes separated by $\Delta x_k, \Delta y_k, \Delta z_k$ in the three coordinate directions. Using grid C_k, the proposed scheme approximates the MOM matrices pertinent to the equivalent problem k as ${}^{\mathrm{EH}}\mathbf{Z}_{kl'} \approx {}^{\mathrm{EH}}\mathbf{Z}_{kl'}^{\mathrm{near}} + {}^{\mathrm{EH}}\mathbf{Z}_{kl'}^{\mathrm{FFT}}$, where

$$
\begin{aligned}
{}^{\mathrm{EH}}\mathbf{Z}_{kl'}^{\mathrm{FFT}} &= \begin{bmatrix} \boldsymbol{\Lambda}_{kl}^{T} & \mathbf{0} \\ \mathbf{0} & \boldsymbol{\Lambda}_{kl}^{T} \end{bmatrix} \underbrace{\begin{bmatrix} \eta_k \mathbf{L}_k^{\mathrm{FFT}} & \mathbf{K}_k^{\mathrm{FFT}} \\ -\mathbf{K}_k^{\mathrm{FFT}} & \mathbf{L}_k^{\mathrm{FFT}} / \eta_k \end{bmatrix}}_{\mathbf{Z}_k^{\mathrm{FFT}}} \begin{bmatrix} \boldsymbol{\Lambda}_{kl'} & \mathbf{0} \\ \mathbf{0} & \boldsymbol{\Lambda}_{kl'} \end{bmatrix} \\
{}^{\mathrm{EH}}\mathbf{Z}_{kl'}^{\mathrm{near}} &= \begin{bmatrix} \eta_k \mathbf{L}_{kl'}^{\mathrm{near}} & \mathbf{K}_{kl'}^{\mathrm{near}} \\ -\mathbf{K}_{kl'}^{\mathrm{near}} & \mathbf{L}_{kl'}^{\mathrm{near}} / \eta_k \end{bmatrix}
\end{aligned}
\qquad (2.1.18)
$$

Here, the projection matrix $\boldsymbol{\Lambda}_{kl'}$, which is a sparse $N_k^{\mathrm{C}} \times N_{kl'}$ matrix with $O(N_{kl'})$ non-zero entries, relates currents on the auxiliary grid C_k to the currents on surface $S_{kl'}$; the propagation matrices $\mathbf{L}_k^{\mathrm{FFT}}$ and $\mathbf{K}_k^{\mathrm{FFT}}$, which are composed of dense but Toeplitz blocks of size $N_k^{\mathrm{C}} \times N_k^{\mathrm{C}}$, relate fields at observation points on C_k to sources on C_k, the interpolation matrix $\boldsymbol{\Lambda}_{kl}^{T}$, which is the transpose of the sparse projection matrix $\boldsymbol{\Lambda}_{kl}$, interpolates fields at observation points on C_k onto the testing functions on S_{kl}, and the pre-correction matrix ${}^{\mathrm{EH}}\mathbf{Z}_{kl'}^{\mathrm{near}}$, which is a sparse matrix with ideally $O(N_{kl'})$ non-zero entries, corrects near-zone errors (see the discussion on computational complexity below). The projection and propagation matrices in (2.1.18) are

$$\boldsymbol{\Lambda}_{kl} = \begin{bmatrix} \boldsymbol{\Lambda}_{kl}^{\mathrm{x}} \\ \boldsymbol{\Lambda}_{kl}^{\mathrm{y}} \\ \boldsymbol{\Lambda}_{kl}^{\mathrm{z}} \\ \boldsymbol{\Lambda}_{kl}^{\nabla} \end{bmatrix}, \ \mathbf{L}_{k}^{\mathrm{FFT}} = \begin{bmatrix} \mathbf{G}_{k}^{\mathrm{A}} & \mathbf{0} & \mathbf{0} & \mathbf{0} \\ \mathbf{0} & \mathbf{G}_{k}^{\mathrm{A}} & \mathbf{0} & \mathbf{0} \\ \mathbf{0} & \mathbf{0} & \mathbf{G}_{k}^{\mathrm{A}} & \mathbf{0} \\ \mathbf{0} & \mathbf{0} & \mathbf{0} & \mathbf{G}_{k}^{\phi} \end{bmatrix}, \mathbf{K}_{k}^{\mathrm{FFT}} = \begin{bmatrix} \mathbf{0} & -\mathbf{G}_{k}^{z} & \mathbf{G}_{k}^{y} & \mathbf{0} \\ \mathbf{G}_{k}^{z} & \mathbf{0} & -\mathbf{G}_{k}^{x} & \mathbf{0} \\ -\mathbf{G}_{k}^{y} & \mathbf{G}_{k}^{x} & \mathbf{0} & \mathbf{0} \\ \mathbf{0} & \mathbf{0} & \mathbf{0} & \mathbf{0} \end{bmatrix} \quad (2.1.19)$$

Here, each column n of the projection matrices $\boldsymbol{\Lambda}_{kl}^{\mathrm{x}}, \boldsymbol{\Lambda}_{kl}^{\mathrm{y}}, \boldsymbol{\Lambda}_{kl}^{\mathrm{z}}, \boldsymbol{\Lambda}_{kl}^{\nabla}$ contain $M_{k,n} = M_{k,n}^{\mathrm{x}} M_{k,n}^{\mathrm{y}} M_{k,n}^{\mathrm{z}}$ non-zero entries at the rows that correspond to the $M_{k,n}$ points on the auxiliary grid C_{k} associated with the basis function $\mathbf{S}_{kl,n}$. These coefficients are filled by matching the multipole moments of the $M_{k,n}$ point sources on C_{k} to those of the functions $\hat{\mathbf{x}} \cdot \mathbf{S}_{kl,n}, \hat{\mathbf{y}} \cdot \mathbf{S}_{kl,n}, \hat{\mathbf{z}} \cdot \mathbf{S}_{kl,n}, \nabla \cdot \mathbf{S}_{kl,n}$, respectively [8, 25]. The entries of the $N_{k}^{\mathrm{C}} \times N_{k}^{\mathrm{C}}$ block-Toeplitz Green function matrices are

$$\begin{aligned} &\{\mathbf{G}_{k}^{\mathrm{x}}[u,u'], \mathbf{G}_{k}^{\mathrm{y}}[u,u'], \mathbf{G}_{k}^{\mathrm{z}}[u,u'], \mathbf{G}_{k}^{\mathrm{A}}[u,u'], \mathbf{G}_{k}^{\phi}[u,u']\} \\ &= \{\partial_{x}, \partial_{y}, \partial_{z}, \gamma_{k}, \frac{1}{\gamma_{k}}\} \frac{e^{-\gamma\left|\mathbf{r}_{u}-\mathbf{r}_{u'}\right|}}{4\pi\left|\mathbf{r}_{u}-\mathbf{r}_{u'}\right|} \end{aligned} \quad (2.1.20)$$

for nodes u and u' on the auxiliary grid C_{k}. To avoid singularities, $\mathbf{G}_{k}^{\mathrm{x,y,z,A},\phi}(u,u) = 0$; to minimize the number of FFTs, the spatial derivatives in $\mathbf{K}_{k}^{\mathrm{FFT}}$ are approximated by finite differences [25, 26]. Thus, only 8 block-Toeplitz matrix-vector multiplications are calculated via FFTs to multiply $\mathbf{Z}_{k}^{\mathrm{FFT}}$ with a trial vector; these correspond to the multiplications of $\eta_{k}\mathbf{L}_{k}^{\mathrm{FFT}}$ with electric and $\mathbf{L}_{k}^{\mathrm{FFT}} / \eta_{k}$ with magnetic current coefficients.

For $1 \le n \le N_{kl}$ and $1 \le n' \le N_{kl'}$, the entries of the near-zone correction matrices in (2.1.18) are either

$$\begin{bmatrix} \mathbf{L}_{kll'}^{\mathrm{near}}[n,n'] \\ \mathbf{K}_{kll'}^{\mathrm{near}}[n,n'] \end{bmatrix} = \begin{bmatrix} \mathbf{L}_{kll'}[n,n'] - \mathbf{L}_{kll'}^{\mathrm{FFT}}[n,n'] \\ \mathbf{K}_{kll'}[n,n'] - \mathbf{K}_{kll'}^{\mathrm{FFT}}[n,n'] \end{bmatrix} \quad (2.1.21)$$

when the testing function $\mathbf{S}_{kl,n}$ is in the near-zone of the basis function $\mathbf{S}_{kl',n'}$ or zero otherwise. A testing function is in the near zone of a basis function if the minimum distance among the nodes assigned to them is less than $\gamma_k^{\mathrm{x}}\Delta x_k$, $\gamma_k^{\mathrm{y}}\Delta y_k$, and $\gamma_k^{\mathrm{z}}\Delta z_k$ in the x, y, and z directions, respectively. The number of nodes N_k^{C}, the grid spacings $\Delta x_k, \Delta y_k, \Delta z_k$, the near-zone thresholds $\gamma_k^{\mathrm{x}}, \gamma_k^{\mathrm{y}}, \gamma_k^{\mathrm{z}}$, and the moment matching orders $M_{k,n}^{\mathrm{x}}, M_{k,n}^{\mathrm{y}}, M_{k,n}^{\mathrm{z}}$ are key AIM parameters that establish a trade-off between the accuracy and efficiency of the method. For each grid C_k, these parameters are chosen according to the wavelength in the equivalent problem k and the surface mesh of S_k.

Assembling the ${}^{\mathrm{EH}}\mathbf{Z}_{kll'}$ matrices as in (2.1.12)-(2.1.15), the method approximates the MOM matrix equation (2.1.12) as

$$\left({}^{\mathrm{EH}}\mathbf{Z}^{\mathrm{FFT}} + {}^{\mathrm{EH}}\mathbf{Z}^{\mathrm{near}}\right)\begin{bmatrix}\mathbf{I}\\ \mathbf{V}\end{bmatrix} \approx \begin{bmatrix}{}^{\mathrm{EH}}\mathbf{V}^{\mathrm{inc}}\\ {}^{\mathrm{EH}}\mathbf{I}^{\mathrm{inc}}\end{bmatrix} \tag{2.1.22}$$

where

$${}^{\mathrm{EH}}\mathbf{Z}^{\mathrm{FFT}} = \sum_k \sum_l \beta_{kl} \begin{bmatrix}\mathbf{C}_{kl}^T\mathbf{\Lambda}_{kl}^T & \mathbf{0}\\ \mathbf{0} & \mathbf{C}_{kl}^T\mathbf{\Lambda}_{kl}^T\end{bmatrix} \mathbf{Z}_k^{\mathrm{FFT}} \sum_{l'=0,l'\neq k}^{K-1} \alpha_{kl'} \begin{bmatrix}\mathbf{\Lambda}_{kl'}\mathbf{C}_{kl'} & \mathbf{0}\\ \mathbf{0} & \mathbf{\Lambda}_{kl'}\mathbf{C}_{kl'}\end{bmatrix} \tag{2.1.23}$$

$${}^{\mathrm{EH}}\mathbf{Z}^{\mathrm{near}} = \sum_k \sum_l \beta_{kl} \begin{bmatrix}\mathbf{C}_{kl}^T & \mathbf{0}\\ \mathbf{0} & \mathbf{C}_{kl}^T\end{bmatrix} \sum_{l'=0,l'\neq k}^{K-1} {}^{\mathrm{EH}}\mathbf{Z}_{kll'}^{\mathrm{near}} \alpha_{kl'} \begin{bmatrix}\mathbf{C}_{kl'} & \mathbf{0}\\ \mathbf{0} & \mathbf{C}_{kl'}\end{bmatrix} \tag{2.1.24}$$

The matrix ${}^{\mathrm{EH}}\mathbf{Z}^{\mathrm{FFT}}$ is multiplied with a trial vector region by region: For each region k, first (as represented by the last summation term in (2.1.23)), the currents on all the surfaces $S_{kl'}$ bounding the region k are identified (represented by $\mathbf{C}_{kl'}$) with their correct sign (+1 if they are on the preferred side of the surfaces and -1 if they or on the non-preferred side, represented by $\alpha_{kl'}$) and projected onto the auxiliary grid C_k (represented by $\mathbf{\Lambda}_{kl'}$). Second, the propagation matrices in $\mathbf{Z}_k^{\mathrm{FFT}}$ are multiplied with the projected currents using the appropriate FFT size for that region. Third, (as represented by the second summation term in (2.1.16)), the testing functions on all the surfaces S_{kl}

bounding the region k are identified (represented by $\mathbf{C}_{kl}^{T}$) and the fields on grid C_{k} are interpolated onto them (represented by $\mathbf{\Lambda}_{kl}^{T}$). Last, the first summation in (2.1.23) linearly combines the tested fields according to the EH-PMCHWT formulation, i.e., the fields on the preferred side of surfaces are multiplied with +1 and the other side with -1 (represented by β_{kl}).

2.1.4.2. Computational Complexity

The multiple-grid AIM, as is typical of AIM schemes, stores the correction matrix ${}^{\mathrm{EH}}\mathbf{Z}^{\mathrm{near}}$ but does not store the dense and non-Toeplitz matrix ${}^{\mathrm{EH}}\mathbf{Z}^{\mathrm{FFT}}$. Rather, it stores the sparse matrices $\mathbf{\Lambda}_{kl}$ and $\mathbf{C}_{kl}$ and unique parts of the block-Toeplitz matrices $\mathbf{Z}_{k}^{\mathrm{FFT}}$. Thus, the multiple-grid AIM requires $O(N^{\mathrm{nz,near}})$ and $O(\sum_{k}[N_{k}^{\mathrm{C}}+\sum_{l}N_{kl}])$ operations/bytes in order to fill/store the near- and far-zone matrices, respectively. Here, $N^{\mathrm{nz,near}}$ denotes the number of non-zero entries in ${}^{\mathrm{EH}}\mathbf{Z}^{\mathrm{near}}$; if there are an average number of $N_{kl}^{\mathrm{b,near}}$ edges that are in the near-zone of the basis functions on S_{kl}, then $N^{\mathrm{nz,near}}=4\sum_{k}\sum_{l>k}N_{kl}N_{kl}^{\mathrm{b,near}}$. To multiply ${}^{\mathrm{EH}}\mathbf{Z}^{\mathrm{near}}$ with a trial vector, the multiple-grid AIM requires $O(N^{\mathrm{nz,near}})$ operations; to multiply ${}^{\mathrm{EH}}\mathbf{Z}^{\mathrm{FFT}}$ with a trial vector, each $\mathbf{Z}_{k}^{\mathrm{FFT}}$ is multiplied with a vector and each such multiplication, which involves block Toeplitz matrices, is efficiently calculated by multi-dimensional FFTs in $O(N_{k}^{\mathrm{C}}\log N_{k}^{\mathrm{C}})$ operations (a precise count of the number of FFTs is given in Section 2.1.4.1). Thus, the setup, solution, and memory costs of the multiple-grid AIM scale as $O(N^{\mathrm{nz,near}}+\sum_{k}N_{k}^{\mathrm{C}})$, $O({}^{\mathrm{EH}}N^{\mathrm{I}}[N^{\mathrm{nz,near}}+\sum_{k}N_{k}^{\mathrm{C}}\log N_{k}^{\mathrm{C}}])$, and $O(N^{\mathrm{nz,near}}+\sum_{k}N_{k}^{\mathrm{C}})$, respectively.

It is not straightforward to express the number of auxiliary grid nodes N_{k}^{C} and the number of near-zone interactions $N^{\mathrm{nz,near}}$ in terms of the number of surface edges N for a general piecewise homogeneous structure. This is because they are dependent non-trivially on the shape and material constitution of the structure, as well as the desired accuracy level. Nevertheless, it should be clear that the performance and shortcomings of multiple-grid AIM reflect those of the classical one- or two-region AIM, as it is a repeated application of the algorithm for each homogeneous region R_k using an appropriately chosen auxiliary grid, e.g., the larger the ratio of the volume enclosed by C_k to the area of S_k is, or the more inhomogeneous the mesh of S_k is, the less efficient the scheme becomes for region R_k. As noted in the motivation section, the proposed multiple-grid AIM scheme outperforms existing single-grid AIM schemes [9-12] for multi-region problems because it has the flexibility of optimizing a different auxiliary grid for each equivalent problem. The efficiency gains resulting from this flexibility are investigated next.

2.1.5. Numerical Results

This section validates the accuracy and computational complexity of the multiple-grid AIM by analyzing scattering from canonical piecewise-homogeneous structures and comparing the performance and scalability of the method to those of the MOM. All the results in this section are obtained on a cluster of 2.66-GHz Xeon quad-core processors that have 2 GB of memory per core using an MPI-based parallel implementation similar to [25]. The total computation times (number of processors times the wall-clock time) and total memory requirements are reported; to minimize the effect of parallelization overheads and inefficiencies, performance data are reported only for the simulations that use the minimum number of processors dictated by the memory requirements. For all multiple-grid AIM simulations, the near-zone thresholds and the number of auxiliary points used for moment matching in all regions are set to $\gamma_k^{\mathrm{x}} = \gamma_k^{\mathrm{y}} = \gamma_k^{\mathrm{z}} = 3$ and $M_{k,n} = 4 \times 4 \times 4$. The accuracy of the method is measured by computing the relative root-mean-square error in the HH- or VV-polarized bistatic radar cross section (RCS) $\sigma_{\theta\theta}$ or $\sigma_{\phi\phi}$:

$$err_{\{\theta\theta,\phi\phi\}} = \left(\frac{\int_0^{2\pi} \int_0^{\pi} \left| \sigma_{\{\theta\theta,\phi\phi\}}^{\text{MG-AIM}} - \sigma_{\{\theta\theta,\phi\phi\}}^{\text{ref}} \right|^2 \sin\theta d\theta d\phi}{\int_0^{2\pi} \int_0^{\pi} \left| \sigma_{\{\theta\theta,\phi\phi\}}^{\text{ref}} \right|^2 \sin\theta d\theta d\phi} \right)^{1/2} \tag{2.1.25}$$

In all simulations, a diagonal preconditioner is used and the iterative solver is terminated when the relative residual error is less than the tolerance tol.

2.1.5.1. *Computational Complexity Validation*

Here, the practical efficiency and accuracy of the multiple-grid AIM scheme for piecewise homogeneous structures are systematically evaluated as the number of edges N increases. The size of multi-region problems can be scaled in several ways; depending on the scaling method, the number of homogeneous regions K may be constant, e.g., if the permittivity of the regions or the analysis frequency is scaled, or K may increase, e.g., as additional regions or layers are added to the structure, as N increases. In the following, the focus is on the latter case to clearly exhibit the advantages of the proposed scheme over single-grid AIM schemes. (In the former case, the computational demands of the multiple-grid AIM scheme are less than but scale identically to those of the single-grid AIM schemes; while the performance improvement can be dramatic if K is large, it would not scale with N). Depending on the application, the number of regions might scale in complicated ways that can be considered a linear combination of two extreme scenarios. On the one extreme, new regions can be added recursively; on the other extreme, they can be added in parallel. In the following, these two scaling methods are exemplified by a layered sphere and a dielectric-rod array as the number of layers and rods are increased, respectively.

2.1.5.2. Layered Sphere

Consider a $K-1$ layered sphere that is centered at the origin and illuminated by an $\hat{x}$-polarized plane wave propagating in the $-\hat{z}$ direction. The sphere's outermost layer (denoted as layer/region 1) has an outer radius of r_1 and permittivity of $\varepsilon_1 = 2\varepsilon_0$ and the inner layer k, $1 < k < K$, has outer radius $r_k = r_{k-1} / \sqrt{2}$ and permittivity $\varepsilon_k = 2\varepsilon_{k-1}$ (Fig. 2.1.5(a)). In the following, the number of layers is increased from 1 to 8 (K from 2 to 9) and r_1 from λ_0 to $4\lambda_0$, where λ_0 denotes the free-space wavelength. The sphere surfaces are meshed such that the average edge length on the outer surface of each layer is ~1/10th of the wavelength in that region; therefore, the number of edges on each surface is the same ($N_0 = ... = N_{K-1}$) and $N = (K-1)N_0$. The multiple-grid AIM parameters are chosen to minimize the computational requirements subject to the constraint that $err_{\theta\theta}$ is less than 2% with respect to the reference Mie series solution. The AIM parameters used in the simulations and the observed RCS errors are given in Table 2.1.1. Figs. 2.1.5(b)-(d) show the setup, solution, and memory costs of the multiple-grid AIM and MOM solutions. For this structure, the number of non-zero entries in the MOM matrix should scale as $N^{\mathrm{nz}} \sim (2K-3)N_0^2$ and the total number of non-zero near-zone entries and Cartesian grid points for multiple-grid AIM should scale as $N^{\mathrm{nz,near}} \sim (K-1)N_0$ and $\sum_k N_k^{\mathrm{C}} \sim KN_0^{1.5}$ according to the analysis in Section 2.1.4.2. The computational costs observed in Fig. 2.1.5(b)-(d) show very good agreement with these predicted trends, e.g., all multiple-grid AIM and MOM computational requirements scale linearly with the number of layers and the multiple-grid AIM outperforms MOM in all metrics for $r_1 \geq \lambda_0$ and $K \geq 2$ $(N_0 \text{ ~ } 2500)$.

Table 2.1.1: Parameters for layered spheres

Sphere, MOM, and Multiple-Grid AIM Parameters		Number of Layers $K-1$	Reference	$err_{\theta\theta}$ $(\%)$
$\varepsilon_1 = 2\varepsilon_0$ $r_k = r_1 / 2^{(k-1)/2}, \varepsilon_k = \varepsilon_1 2^{k-1}$ $N = (K-1)N_0$ $N_1 = \ldots = N_{K-3} = 2N_0$ $N_1^{\mathrm{C}} = \ldots = N_{K-1}^{\mathrm{C}}$ $tol = 10^{-3}$	$r_1 = \lambda_0$ $N_{K-2} = N_0 = 2\ 766$ $N_0^{\mathrm{C}} = 24 \times 24 \times 24$ $N_1^{\mathrm{C}} = 24 \times 24 \times 24$	1	Mie	0.72
			MOM	0.74
		2	Mie	1.58
			MOM	1.57
		4	Mie	1.40
			MOM	1.56
		8	Mie	1.76
			MOM	0.89
	$r_1 = 2\lambda_0$ $N_{K-2} = N_0 = 10\ 947$ $N_0^{\mathrm{C}} = 40 \times 40 \times 40$ $N_1^{\mathrm{C}} = 48 \times 48 \times 48$	1	Mie	0.82
			MOM	0.98
		2	Mie	1.03
			MOM	1.20
		4	Mie	1.82
			MOM	1.84
		8	Mie	1.34
			MOM	-
	$r_1 = 4\lambda_0$ $N_{K-2} = N_0 = 44\ 595$ $N_0^{\mathrm{C}} = 80 \times 80 \times 80$ $N_1^{\mathrm{C}} = 96 \times 96 \times 96$	1	Mie	0.61
			MOM	-
		2	Mie	0.72
			MOM	-
		4	Mie	1.79
			MOM	-
		8	Mie	1.44
			MOM	-

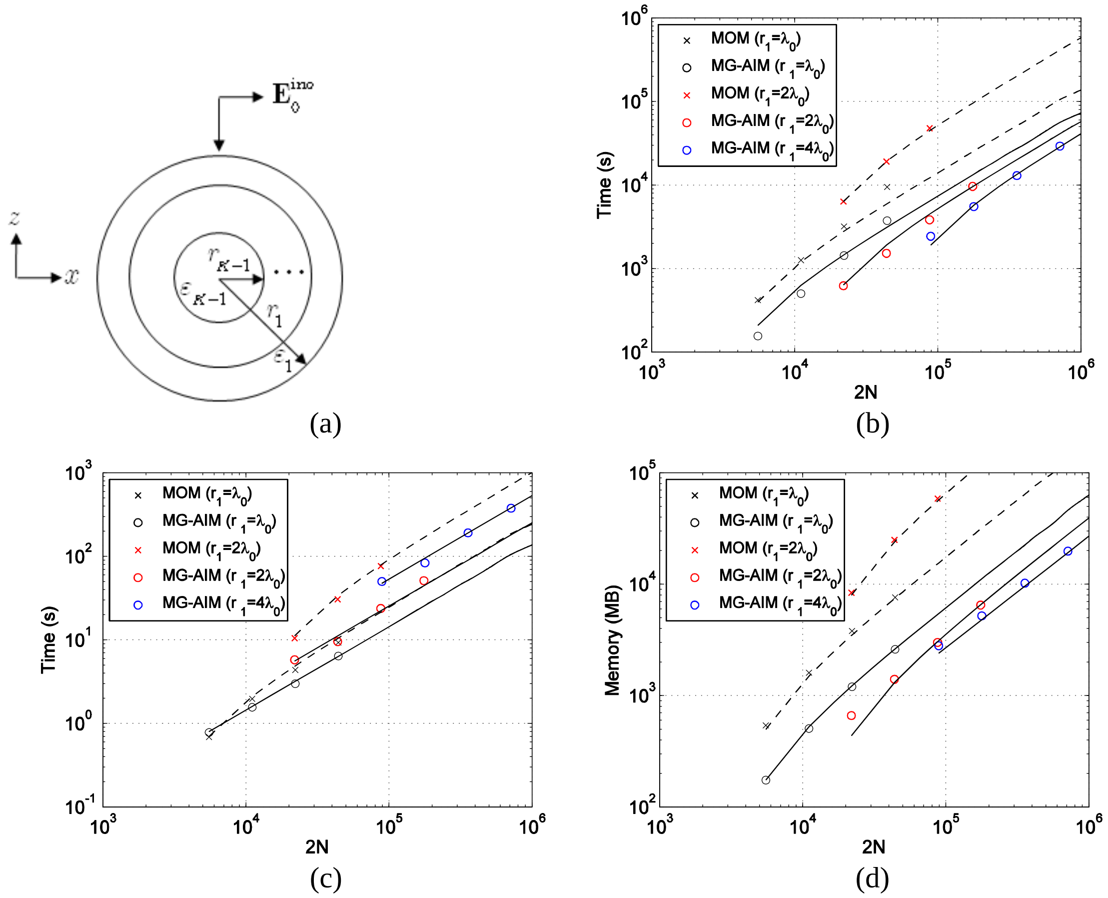

(a) (b) (c) (d)

Figure 2.1.5: Multiple-grid AIM vs. MOM for the layered dielectric sphere as the number of layers is increased. (a) Configuration of the layered sphere. (b) The setup cost. (c) The solution cost per iteration. (d) The memory cost. All dashed and straight lines are parallel to $2K-3$ except the straight lines in (c) that are parallel to $K-1$.

Notice that, even though $N_0^{\mathrm{C}} \approx N_1^{\mathrm{C}} \approx \ldots \approx N_{K-1}^{\mathrm{C}}$ for the layered spheres, a single-grid AIM scheme would not be efficient here because the auxiliary grid spacing for the innermost region is much smaller than that of the outermost region for each sphere, e.g., ~11 times for $K = 8$: (i) If the single grid's spacing was set to that of grid 0, then the approach would result in significantly larger number of near-zone corrections than the multiple-grid AIM scheme for the inner regions, e.g., the innermost region would have $\sim N_0^2$ instead of $\sim N_0$ near-zone terms. (ii) If the single grid's spacing was set to that of grid $K-1$, then the approach would result in significantly larger number of grid points than the multiple-grid AIM scheme for the outer regions, e.g., the outermost region would have $\sim 11^3 N_0^{1.5}$ instead of $\sim N_0^{1.5}$ grid points for $K=8$. This comparison shows that the single-grid AIM approach would quickly become ineffective as the number of regions is scaled recursively, while the multiple-grid AIM scheme remains effective.

2.1.5.3. Dielectric-Rod Array

Consider a uniform two-dimensional array of $K-1$ thin dielectric cylinders on the $x-y$ plane illuminated by a plane wave polarized along $(\theta,\phi)=(120^o, 30^o)$ and propagating in the direction $(\theta,\phi)=(30^o, 30^o)$. The array spacing is $0.36\lambda_0$ and each cylinder has a height of $2/3\,\lambda_0$, radius of $0.01\lambda_0$ and permittivity of $44\varepsilon_0$ (Fig. 2.1.6(a)). In the following, the number of cylinders is scaled from 1 to 32×32 (K from 2 to 1025). Each cylinder circumference is divided into 8 subsections to resolve the circular cross section and meshed such that the average vertical edge length is ~1/10th of the wavelength in the cylinder (Fig. 2.1.6(a)); thus, the number of edges on each cylinder is the same ($N_1 = ... = N_{K-1} = N_0/(K-1)$) and $N=(K-1)N_1$. The multiple-grid AIM parameters are chosen to minimize the computational requirements subject to the constraint that $err_{\theta\theta}$ is less than 0.5% with respect to a reference MOM solution using the same mesh. The AIM parameters used in the simulations and the resulting RCS errors are given in Table 2.1.2. Figs. 2.1.6(b)-(d) show the setup, solution, and memory costs of the multiple-grid AIM and MOM solutions. For this structure, the MOM matrix is dense and its number of non-zero entries should scale as $N^{\mathrm{nz}}=(K-1)^2 N_1^2$ and the total number of non-zero near-zone entries and Cartesian grid points for multiple-grid AIM should scale as $N^{\mathrm{nz,near}} \sim (K-1)N_1$ and $\sum_k N_k^{\mathrm{C}} \sim KN_1$. The computational costs observed in Fig. 2.1.6(b)-(d) agree with these predicted trends, e.g., all MOM and multiple-grid AIM computational requirements scale quadratically and linearly with the number of cylinders, respectively, and the multiple-grid AIM outperforms MOM in all metrics for $K \geq 2\ (N_0 \sim 1000)$. Note that, the auxiliary grid spacing for all regions of the dielectric-rod array are the same; however, the multiple-grid AIM scheme requires significantly smaller number of grid points for the internal regions compared to the external region, e.g., ~1225 times for $K = 1025$. A single-grid AIM scheme would not be efficient here because it would have to use the largest grid in all regions; e.g., to compute the FFTs, it would require $KN_0^{\mathrm{C}} \log N_0^{\mathrm{C}} / \sum_k N_k^{\mathrm{C}} \log N_k^{\mathrm{C}} \sim K$ times more operations than the multiple-grid AIM scheme. This comparison shows that the single-grid AIM approach would quickly become ineffective as the number of regions is scaled in parallel, while the multiple-grid AIM scheme remains effective.

Table 2.1.2: Parameters for dielectric-rod arrays

Dielectric Rod Array, MOM, and Multiple-Grid AIM Parameters		Number of Rods $K-1$	Reference	$err_{\theta\theta}$ $(\%)$
$\varepsilon_k = 44\varepsilon_0$ $N = N_0 = (K-1)N_1$ $N_1 = \ldots = N_{K-1} = 1224$ $N_1^{\mathrm{C}} = \ldots = N_{K-1}^{\mathrm{C}} = 6\times 6\times 32$ $tol = 10^{-4}$	$N_0^{\mathrm{C}} = 6\times 6\times 32$	1×1	MOM	0.11
	$N_0^{\mathrm{C}} = 14\times 14\times 32$	2×2	MOM	0.28
	$N_0^{\mathrm{C}} = 25\times 25\times 32$	4×4	MOM	0.22
	$N_0^{\mathrm{C}} = 54\times 54\times 32$	8×8	MOM	0.19
	$N_0^{\mathrm{C}} = 105\times 105\times 32$	16×16	-	-
	$N_0^{\mathrm{C}} = 210\times 210\times 32$	32×32	-	-

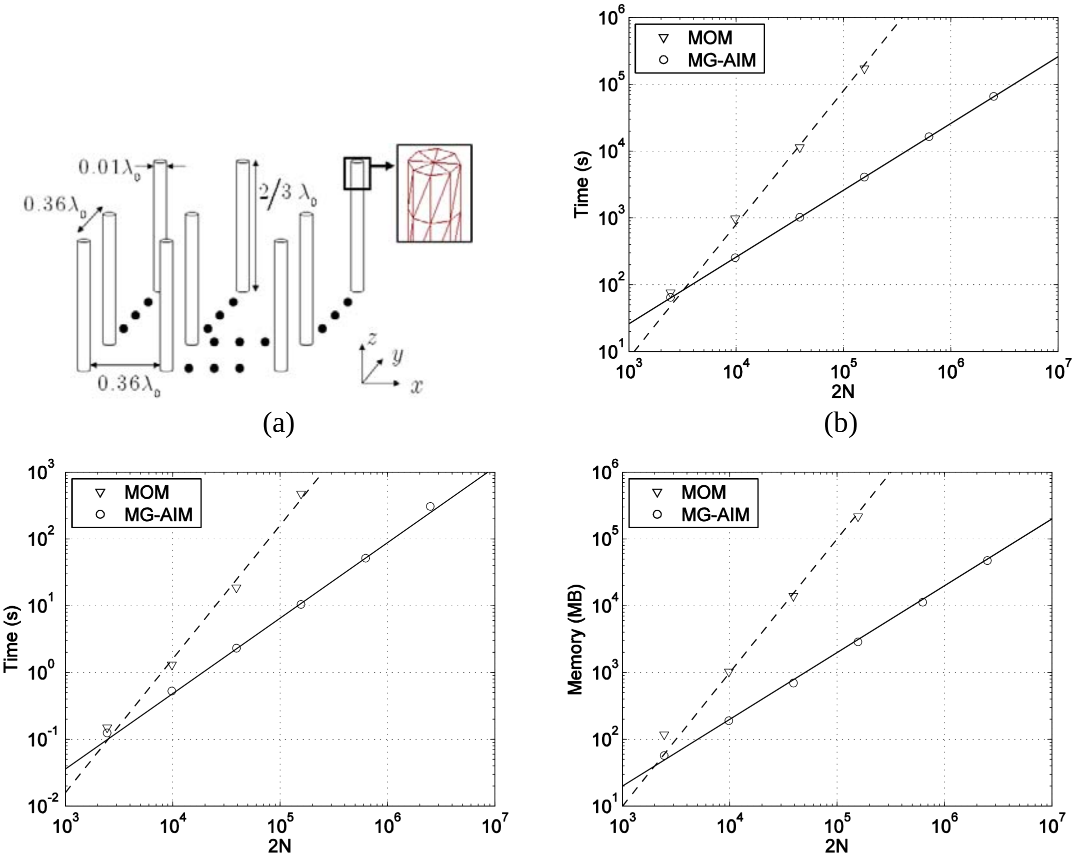

(a)

(b)

(c)

(d)

Figure 2.1.6: Multiple-grid AIM vs. MOM for the dielectric cylinder array as the number of cylinders is increased. (a) Configuration of the dielectric rod-array and part of the mesh. (b) The setup cost. (c) The solution cost per iteration. (d) The memory cost. Dashed lines are parallel to K^2 and straight lines are parallel to K.

2.1.6. Summary

This section presented the multiple-grid AIM scheme for accelerating the MOM analysis of scattering from piecewise homogeneous structures. The method employs multiple auxiliary grids that have different locations, grid spacings, and associated projection, propagation, and interpolation operators. Numerical results demonstrated that the availability of multiple grids enables the scheme to be effective for a variety of structures with large number of regions, e.g., an 8-layered sphere and a 1024-element dielectric-rod array, for which single-grid AIM schemes are not effective.

2.2. MODELING A PEC/PMC PLANE

PEC/PMC planes are used in many scattering applications to reduce the analysis complexity and to simplify/emphasize part of the wave physics, e.g., the earth is often modeled as a PEC plane as a first approximation when characterizing communication channels in forests [1]. Surface integral equation based simulators can model a PEC/PMC plane using two approaches based on the method of images: The “brute-force imaging” approach removes the plane, introduces the image of the structure of interest (and the excitation), and finds unknown currents on the actual structure and its image. The “Green-function modification” approach adds appropriate reflection terms to the homogeneous-medium Green functions (and to the excitation) and finds unknown currents on the actual structure. Brute-force imaging is more straightforward because it does not require any changes to an existing simulator (only a pre-processing step to image the structure mesh is needed); yet, it is less efficient: It doubles the number of homogeneous regions not terminated on the plane and it doubles the volume and the bounding-surface area of regions terminated on the plane; thus, it produces (almost) twice as many unknowns as Green-function modification. (The ratio is strictly less than two when the plane terminates regions because of junction treatment, see Section 2.2.2). As a result, a classical iterative method of moments (MOM) solver using Green-function modification would require (almost) half of the memory space, half of the matrix-fill time, and half of the matrix-solve time per iteration for general multi-region problems. For important special cases, e.g., two-region problems, it can even require (almost) a quarter of the memory space and matrix-solve time per iteration compared to brute-force imaging (Section 2.2.1). Moreover, iterative MOM solvers using Green-function modification generally require smaller numbers of iterations for convergence. No attempt is made to quantify this gain here because the number of iterations depends non-trivially on the structure, excitation, solver type, etc.; henceforth, the matrix-solve time refers to the time per iteration. While Green-function modification is easy to implement for classical MOM solvers, it requires more substantial changes for fast algorithms that rely on various properties of homogeneous-medium Green functions [27, 28].

This section presents the efficient incorporation of a PEC/PMC plane to the multiple-grid AIM. Both imaging approaches pose problems for multiple-grid AIM. On the one hand, brute-force imaging can be extremely inefficient for “space filling” methods like multiple-grid AIM when the structure is high above the PEC/PMC plane: Because the auxiliary grid for a given region must enclose all the (finite) surfaces bounding that region, the grid for the outer-most region would cover any empty space between the actual structure and its image; the corresponding FFT sizes would increase; and the performance of the method would decrease with the distance of the structure from the PEC/PMC plane. On the other hand, Green-function modification cannot be used directly: The added reflection terms, which are in correlation form in the direction normal to the PEC/PMC plane, give rise to Hankel-(two level)block-Toeplitz “reflection matrices”. Fortunately, FFT-based methods for multiplying Hankel matrices (calculating correlations) [29, 30] can be seamlessly combined with those for multiplying Toeplitz matrices (calculating convolutions) to efficiently multiply Hankel-block-Toeplitz matrices. Separate FFT-based multiplication of Hankel and Toeplitz matrices, however, doubles the FFT cost and can slow the method to the same level as brute-force imaging for structures near the plane. To improve efficiency, the FFTs computed for multiplying propagation matrices are reused when multiplying reflection matrices. For general multi-region problems, multiple-grid AIM with the proposed modifications requires (almost) half as much memory space, matrix-fill time, and matrix-solve time as multiple-grid AIM with brute-force imaging, even when the structure is on the PEC/PMC plane.

For the sake of brevity, the formulation in this section is specialized to a two-region problem involving a PEC plane. The methods easily generalize to multi-region problems or a PMC plane; the implications of these generalizations are explicitly noted when they are not trivial. The rest of this section is organized as follows. Section 2.2.1 formulates the two imaging approaches for MOM; Section 2.2.2 analyzes the MOM computational complexity; Section 2.2.3 formulates the two imaging approaches for multiple-grid AIM; Section 2.2.4 analyzes their computational complexity; and Section 2.2.5 presents numerical results that validate the approaches and compare their efficiency.

2.2.1. Green Function Modification for MOM

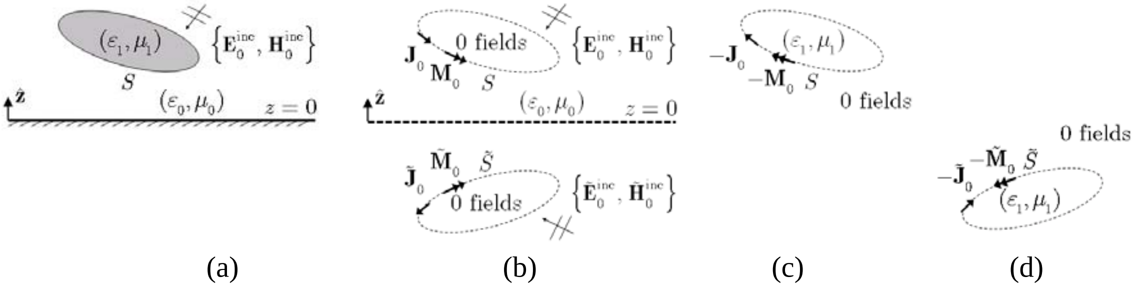

Figure 2.2.1: (a) A homogeneous structure above a PEC plane at $z=0$ and (b) external-, (c) actual internal-, and (d) image internal-equivalent problems.

Consider a homogeneous structure with surface S residing above a PEC plane at $z=0$ excited by an external time-harmonic electromagnetic field $\{\mathbf{E}_0^{\rm inc},\mathbf{H}_0^{\rm inc}\}$ (Fig. 2.2.1). The scattered fields can be found by brute-force imaging as follows: (i) Apply method of images: Remove the plane; introduce the image structure with surface $\tilde{S}$; and excite the new structure with the sum of $\{\mathbf{E}_0^{\rm inc},\mathbf{H}_0^{\rm inc}\}$ and its image $\{\tilde{\mathbf{E}}_0^{\rm inc},\tilde{\mathbf{H}}_0^{\rm inc}\}$. (ii) Formulate integral equations: Construct equivalent problems (Fig. 2.2.1); formulate electric- and magnetic-field integral equations for each problem; and combine them using the EH-PMCHWT recipe. (iii) Apply the MOM procedure with RWG basis functions and Galerkin testing: Mesh S with triangle patches with N edges and $\tilde{S}$ with the images of these patches; and expand the electric and magnetic current densities $\{\mathbf{J}, \mathbf{M}\}$ on S ("actual currents") and $\{\tilde{\mathbf{J}}, \tilde{\mathbf{M}}\}$ on $\tilde{S}$ ("image currents") as

$$\begin{aligned} \{\mathbf{J}(\mathbf{r}), \mathbf{M}(\mathbf{r})\} &\cong \sum_{n'=1}^{N} \{\mathbf{I}[n'], \mathbf{V}[n']\} \mathbf{S}^{\mathrm{a}}_{n'}(\mathbf{r}) \\ \{\tilde{\mathbf{J}}(\mathbf{r}), \tilde{\mathbf{M}}(\mathbf{r})\} &\cong \sum_{n'=1}^{N} \{\tilde{\mathbf{I}}[n'], \tilde{\mathbf{V}}[n']\} \mathbf{S}^{\mathrm{i}}_{n'}(\mathbf{r}) \end{aligned} \tag{2.2.26}$$

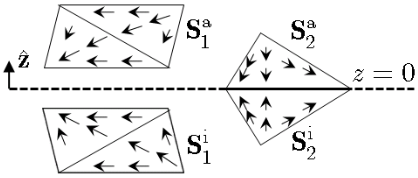

Figure 2.2.2: An actual RWG and a half-RWG basis function and their images.

Here, $\mathbf{I}, \mathbf{V}, \tilde{\mathbf{I}},$ and $\tilde{\mathbf{V}}$ are vectors of unknown coefficients, $\mathbf{S}^{\mathrm{a}}_{n'}$ (an actual RWG) is an RWG function on the actual structure, and $\mathbf{S}^{\mathrm{i}}_{n'}$ (an image RWG) is the image of $\mathbf{S}^{\mathrm{a}}_{n'}$ with the same transverse and opposite vertical vector components (Fig. 2.2.2):

$$\{\hat{\mathbf{t}}, \hat{\mathbf{z}}\} \bullet \mathbf{S}^{\mathrm{i}}_{n'}(\tilde{\mathbf{r}}) = \{\hat{\mathbf{t}}, -\hat{\mathbf{z}}\} \bullet \mathbf{S}^{\mathrm{a}}_{n'}(\mathbf{r}) \tag{2.2.27}$$

where $\mathbf{r}$ is the position vector, $\tilde{\mathbf{r}} = \mathbf{r} - 2(\mathbf{r} \bullet \hat{\mathbf{z}})\hat{\mathbf{z}}$ is its image, and $\hat{\mathbf{t}}$ ($\hat{\mathbf{z}}$) is a unit vector parallel (normal) to the PEC plane. Galerkin testing yields the brute-force imaging (BFI) equations

$$\sum_{k=0}^{2} \begin{bmatrix} \eta_k \mathbf{L}_k & \mathbf{K}_k \\ -\mathbf{K}_k & \mathbf{L}_k / \eta_k \end{bmatrix} \begin{bmatrix} \mathbf{I} \\ \tilde{\mathbf{I}} \\ \mathbf{V} \\ \tilde{\mathbf{V}} \end{bmatrix} = \begin{bmatrix} {}^{\mathrm{EH}}\mathbf{V}^{\text{a-inc}}_0 \\ {}^{\mathrm{EH}}\mathbf{V}^{\text{i-inc}}_0 \\ {}^{\mathrm{EH}}\mathbf{I}^{\text{a-inc}}_0 \\ {}^{\mathrm{EH}}\mathbf{I}^{\text{i-inc}}_0 \end{bmatrix} \text{(BFI)} \tag{2.2.28}$$

Here and throughout this section, the subscript of a matrix or vector shows the equivalent problem (0 for external-, 1 for actual internal-, and 2 for image internal-equivalent) and the superscript above a vector shows the testing function ("a-inc" for actual and "i-inc" for image RWG) used to fill it. The entries of the right-hand-side vectors are (for $1 \le n \le N$)

$$\begin{aligned} \{{}^{\mathrm{EH}}\mathbf{V}_0^{\text{a-inc}}[n], {}^{\mathrm{EH}}\mathbf{V}_0^{\text{i-inc}}[n]\} &= \iint \{\mathbf{S}_n^{\mathrm{a}}, \mathbf{S}_n^{\mathrm{i}}\}\bullet(\mathbf{E}_0^{\mathrm{inc}} + \tilde{\mathbf{E}}_0^{\mathrm{inc}})ds \\ \{{}^{\mathrm{EH}}\mathbf{I}_0^{\text{a-inc}}[n], {}^{\mathrm{EH}}\mathbf{I}_0^{\text{i-inc}}[n]\} &= \iint \{\mathbf{S}_n^{\mathrm{a}}, \mathbf{S}_n^{\mathrm{i}}\}\bullet(\mathbf{H}_0^{\mathrm{inc}} + \tilde{\mathbf{H}}_0^{\mathrm{inc}})ds \end{aligned} \quad (2.2.29)$$

$\mathbf{X}_k \in \{\mathbf{L}_k, \mathbf{K}_k\}$, then the entries of these $2N \times 2N$ matrices can be found by expressing them as

$$\mathbf{X}_k = \begin{bmatrix} \mathbf{X}_k^{\mathrm{aa}} & \mathbf{X}_k^{\mathrm{ai}} \\ \mathbf{X}_k^{\mathrm{ia}} & \mathbf{X}_k^{\mathrm{ii}} \end{bmatrix} \quad (2.2.30)$$

It is important to note that some of these $N \times N$ sub-matrices can be zero (e.g., $\mathbf{X}_1^{\mathrm{ai,ia,ii}} = \mathbf{X}_2^{\mathrm{aa,ai,ia}} = \mathbf{0}$ when the structure does not intersect the PEC plane); otherwise, their entries are

$$\begin{aligned} \mathbf{L}_k^{\mathrm{ts}}[n,n'] &= \gamma_k \iint \iint \mathbf{S}_n^{\mathrm{t}}(\mathbf{r})\bullet\mathbf{S}_{n'}^{\mathrm{s}}(\mathbf{r}')g_k(\mathbf{r},\mathbf{r}')ds'ds \\ &\quad + \frac{1}{\gamma_k}\iint \iint \nabla\bullet\mathbf{S}_n^{\mathrm{t}}(\mathbf{r})\nabla'\bullet\mathbf{S}_{n'}^{\mathrm{s}}(\mathbf{r}')g_k(\mathbf{r},\mathbf{r}')ds'ds \\ \mathbf{K}_k^{\mathrm{ts}}[n,n'] &= \iint \mathbf{S}_n^{\mathrm{t}}(\mathbf{r})\bullet\nabla\times\iint \mathbf{S}_{n'}^{\mathrm{s}}(\mathbf{r}')g_k(\mathbf{r},\mathbf{r}')ds'ds \\ g_k(\mathbf{r},\mathbf{r}') &= e^{-\gamma_k|\mathbf{r}-\mathbf{r}'|} / (4\pi\,|\,\mathbf{r}-\mathbf{r}'\,|) \end{aligned} \quad (2.2.31)$$

for $1 \le n,n' \le N$ and $\mathrm{t,s} \in \{\mathrm{a,i}\}$. In the above equations, $g_k(\mathbf{r},\mathbf{r}')$ is the homogeneous-medium Green function and ε_k, μ_k, γ_k, and η_k are the permittivity, permeability, propagation constant, and intrinsic impedance for free space ($k = 0$) or dielectric structure ($k = 1,2$), respectively. The MOM matrix equation (2.2.28) can be simplified by enforcing that the image and actual electric (magnetic) currents have opposite (identical) tangential components and identical (opposite) vertical components, i.e.,

$$\begin{aligned} \hat{\mathbf{t}}\bullet\{\mathbf{J}(\mathbf{r}), \mathbf{M}(\mathbf{r})\} &= \hat{\mathbf{t}}\bullet\{-\tilde{\mathbf{J}}(\tilde{\mathbf{r}}), \tilde{\mathbf{M}}(\tilde{\mathbf{r}})\} \\ \hat{\mathbf{z}}\bullet\{\mathbf{J}(\mathbf{r}), \mathbf{M}(\mathbf{r})\} &= \hat{\mathbf{z}}\bullet\{\tilde{\mathbf{J}}(\tilde{\mathbf{r}}), -\tilde{\mathbf{M}}(\tilde{\mathbf{r}})\} \end{aligned} \quad (2.2.32)$$

Substituting (2.2.26) in (2.2.32) and comparing to (2.2.27), it is clear that

$$\{\tilde{\mathbf{I}}, \tilde{\mathbf{V}}\} = \{-\mathbf{I}, \mathbf{V}\} \quad (2.2.33)$$

Substituting (2.2.33) in (2.2.28), two sets of equations are obtained for $\mathbf{I}$ and $\mathbf{V}$: One using actual and the other using image testing functions. Either set or their linear combination can be solved uniquely for $\mathbf{I}$, $\tilde{\mathbf{I}}$, $\mathbf{V}$ and $\tilde{\mathbf{V}}$; here, the first set is chosen:

$$\sum_{k=0}^{1}\begin{bmatrix}\eta_k(\mathbf{L}_k^{\mathrm{aa}}-\mathbf{L}_k^{\mathrm{ai}}) & \mathbf{K}_k^{\mathrm{aa}}+\mathbf{K}_k^{\mathrm{ai}} \\ -\mathbf{K}_k^{\mathrm{aa}}+\mathbf{K}_k^{\mathrm{ai}} & (\mathbf{L}_k^{\mathrm{aa}}+\mathbf{L}_k^{\mathrm{ai}})\big/\eta_k\end{bmatrix}\begin{bmatrix}\mathbf{I} \\ \mathbf{V}\end{bmatrix}=\begin{bmatrix}{}^{\mathrm{EH}}\mathbf{V}_0^{\text{a-inc}} \\ {}^{\mathrm{EH}}\mathbf{I}_0^{\text{a-inc}}\end{bmatrix}\ (\mathrm{GFM}) \tag{2.2.34}$$

This is called the Green-function modification (GFM) approach because the entries of $\mathbf{X}_k^{\mathrm{ai}}$ (when $\mathbf{X}_k^{\mathrm{ai}}\neq\mathbf{0}$) are the same as those of $\mathbf{X}_k^{\mathrm{aa}}$ with $g_k(\mathbf{r},\mathbf{r}')$ replaced by $g_k(\mathbf{r},\tilde{\mathbf{r}}')$.

2.2.2. MOM Computational Complexity and Extensions

There are 12 unique matrices ($\mathbf{X}_0^{\mathrm{aa,ai,ia,ii}},\mathbf{X}_1^{\mathrm{aa}}$, and $\mathbf{X}_2^{\mathrm{ii}}$) in (2.2.28) and 6 unique matrices ($\mathbf{X}_0^{\mathrm{aa,ai}}$ and $\mathbf{X}_1^{\mathrm{aa}}$) in (2.2.34) that are dense. BFI and GFM approaches solve for $2N$ and N unknowns and require $O(12N^2)$ and $O(6N^2)$ bytes/operations to fill the unique matrices and $O(24N^2)$ and $O(12N^2)$ operations per iteration to calculate non-zero matrix-vector multiplications, respectively[2]. Thus, GFM finds half the number of unknowns and requires half the memory space, matrix-fill operations, and matrix-solve operations compared to BFI.

When the PEC plane intersects the homogeneous structure, there are 2 equivalent problems, 16 unique matrices ($\mathbf{X}_{0,1}^{\mathrm{aa,ai,ia,ii}}$) in (2.2.28), and 8 unique matrices ($\mathbf{X}_{0,1}^{\mathrm{aa,ai}}$) in (2.2.34). Moreover, junction edges must be treated carefully: Let N^{r} and N^{j} denote the number of regular edges that reside on the mesh of S but not on the PEC plane and junction edges that reside at the intersection of the PEC plane and S, respectively. In

---

[2] These expressions assume that each unique matrix is stored separately; alternatively, the summations in (2.2.28) and (2.2.34) can be executed first and one $4N\times4N$ and one $2N\times2N$ dense matrix can be stored, respectively. This is appealing for two-region problems as it can halve the number of multiplications per iteration. The cost reduction is not as pronounced and the implementation is not as simple, however, for multi-region problems where $\mathbf{X}_k$ are sparse [20, 23].

this case, BFI and GFM approaches use $2N^{\mathrm{r}}+N^{\mathrm{j}}$ RWG functions and $N=N^{\mathrm{r}}+N^{\mathrm{j}}$ functions of which N^{r} are RWG and N^{j} are half-RWG functions (Fig. 2.2.2); because $N^{\mathrm{j}} \ll N^{\mathrm{r}}$ in general, they require $O(16N^2)$ and $O(8N^2)$ bytes/ operations to fill the unique matrices and $O(32N^2)$ and $O(16N^2)$ operations per iteration, respectively. Thus, GFM still solves for (almost) half the number of unknowns and requires (almost) half the resources compared to BFI.

When the structure is piecewise homogeneous and some of its regions are terminated on the plane, the analysis can be generalized. Let K denote the number of regions of the structure *and* its image; and let N_k and $\alpha_k N_k$ denote the number of equations/ unknowns used for region k by BFI and GFM, respectively. If region k is terminated on the plane, then $\alpha_k \sim 0.5$; if it resides above the plane, then $\alpha_k = 1$; if it resides below the plane, then $\alpha_k = 0$. Thus, BFI and GFM require $O(2N_k^2)$ and $O(4\alpha_k^2 N_k^2)$ bytes/operations to fill the unique matrices and $O(4N_k^2)$ and $O(8\alpha_k^2 N_k^2)$ operations per iteration for region k, respectively. Because each region k where $\alpha_k = 1$ has an image region $\tilde{k}$ where $\alpha_{\tilde{k}} = 0$, the above complexity estimates hold true in general and GFM (almost) halves all computational requirements.

When the structure is on/above a PMC plane, $\{\tilde{\mathbf{E}}_0^{\mathrm{inc}}, \tilde{\mathbf{H}}_0^{\mathrm{inc}}\}$ in (2.2.29) and the signs of the $\mathbf{X}^{\mathrm{ai}}$ terms in (2.2.34) must be modified according to duality (i.e., $\{\tilde{\mathbf{I}}, \tilde{\mathbf{V}}\} = \{\mathbf{I}, -\mathbf{V}\}$ for a PMC plane).

2.2.3. Green Function Modification for Multiple-Grid AIM

When brute-force imaging is used, the multiple-grid AIM defines three auxiliary grids $C_{0,1,2}$ with $N_{0,1,2}^{\mathrm{C}}$ grid points that enclose $S_0 = S \cup \tilde{S}$, $S_1 = S$, and $S_2 = \tilde{S}$ to speed up the calculations stemming from the external-, actual internal-, and image

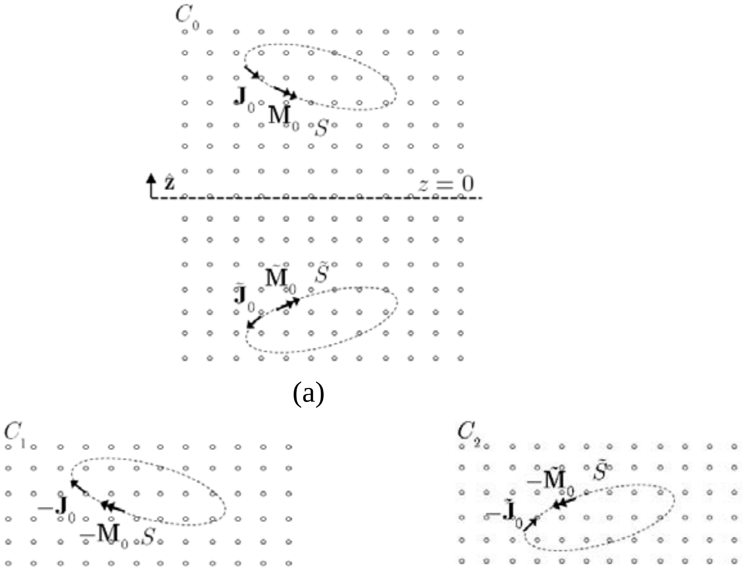

(a)

(b) (c)

Figure 2.2.3: The three multiple-grid AIM auxiliary grids used for brute-force imaging: (a) C_0, (b) C_1, and (c) C_2.

internal-equivalent problem, respectively (Fig. 2.2.3). Using these auxiliary grids, the multiple-grid AIM approximates the MOM matrices in (2.2.28) as (for $0 \le k \le 2$)

$$\mathbf{X}_k \approx \mathbf{X}_k^{\text{near}} + \mathbf{\Lambda}_k^{\dagger} \mathbf{X}_k^{\text{FFT}} \mathbf{\Lambda}_k \tag{2.2.35}$$

where $\mathbf{\Lambda}_k$ are projection matrices that map the currents on S_k to point sources on C_k, $\mathbf{X}_k^{\text{FFT}} \in \{\mathbf{L}_k^{\text{FFT}}, \mathbf{K}_k^{\text{FFT}}\}$ are propagation matrices that relate fields at observation points on C_k to point sources on C_k, $\mathbf{X}_k^{\text{near}} \in \{\mathbf{L}_k^{\text{near}}, \mathbf{K}_k^{\text{near}}\}$ are correction matrices that adjust near-zone entries, and $\dagger$ denotes transpose. The projection matrices are expressed as

$$\mathbf{\Lambda}_k = \begin{bmatrix} \mathbf{\Lambda}_k^{\text{a}} & \mathbf{\Lambda}_k^{\text{i}} \end{bmatrix} = \begin{bmatrix} \mathbf{\Lambda}_k^{\text{a,x}} & \mathbf{\Lambda}_k^{\text{i,x}} \\ \mathbf{\Lambda}_k^{\text{a,y}} & \mathbf{\Lambda}_k^{\text{i,y}} \\ \mathbf{\Lambda}_k^{\text{a,z}} & \mathbf{\Lambda}_k^{\text{i,z}} \\ \mathbf{\Lambda}_k^{\text{a},\nabla} & \mathbf{\Lambda}_k^{\text{i},\nabla} \end{bmatrix} \tag{2.2.36}$$

where the $4N_k^{\text{C}} \times N$ projection matrices $\mathbf{\Lambda}_k^{\text{a}}$ and $\mathbf{\Lambda}_k^{\text{i}}$ are sparse with $O(N)$ non-zero entries ($\mathbf{\Lambda}_1^{\text{i}} = \mathbf{\Lambda}_2^{\text{a}} = \mathbf{0}$ when the PEC plane does not intersect the structure). The $4N_k^{\text{C}} \times 4N_k^{\text{C}}$ propagation matrices are constructed as

$$\begin{aligned}\mathbf{L}_k^{\mathrm{FFT}} &= \mathrm{diag}(\mathbf{G}_k^{\mathrm{A}}, \mathbf{G}_k^{\mathrm{A}}, \mathbf{G}_k^{\mathrm{A}}, \mathbf{G}_k^{\phi}) \\ \mathbf{K}_k^{\mathrm{FFT}} &= \begin{bmatrix} \mathbf{0} & -\mathbf{G}_k^{\mathrm{z}} & \mathbf{G}_k^{\mathrm{y}} & \mathbf{0} \\ \mathbf{G}_k^{\mathrm{z}} & \mathbf{0} & -\mathbf{G}_k^{\mathrm{x}} & \mathbf{0} \\ -\mathbf{G}_k^{\mathrm{y}} & \mathbf{G}_k^{\mathrm{x}} & \mathbf{0} & \mathbf{0} \\ \mathbf{0} & \mathbf{0} & \mathbf{0} & \mathbf{0} \end{bmatrix}\end{aligned} \tag{2.2.37}$$

where the entries of the $N_k^{\mathrm{C}} \times N_k^{\mathrm{C}}$ Green function matrices are

$$\mathbf{G}_k^{\mathrm{x,y,z,A,}\phi}[u,u'] = \{\partial_x, \partial_y, \partial_z, \gamma_k, 1/\gamma_k\} g_k(\mathbf{r}_u, \mathbf{r}_{u'}) \tag{2.2.38}$$

for nodes u and u' on C_k ($\mathbf{G}_k^{\mathrm{x,y,z,A,}\phi}[u,u] = 0$). These are dense (three level) block Toeplitz matrices of size $N_k^{\mathrm{C}} \times N_k^{\mathrm{C}}$ that can be multiplied with (projected) coefficient vectors in $O(N_k^{\mathrm{C}} \log N_k^{\mathrm{C}})$ operations using (three dimensional) FFTs[3]. In (2.2.35), the $2N \times 2N$ correction matrices $\mathbf{X}_k^{\mathrm{near}}$ are sparse with $N_k^{\mathrm{nz,near}}$ entries and can be formulated as

$$\mathbf{X}_k^{\mathrm{near}} = \begin{bmatrix} \mathbf{X}_k^{\mathrm{near,aa}} & \mathbf{X}_k^{\mathrm{near,ai}} \\ \mathbf{X}_k^{\mathrm{near,ia}} & \mathbf{X}_k^{\mathrm{near,ii}} \end{bmatrix} \tag{2.2.39}$$

Some of these sub-matrices are zero similar to (2.2.30); the entries of the non-zero sub-matrices are

$$\mathbf{X}_k^{\mathrm{near,ts}}[n,n'] = \begin{cases} (\mathbf{X}_k^{\mathrm{ts}} - \mathbf{\Lambda}_k^{\mathrm{t}\dagger} \mathbf{X}_k^{\mathrm{FFT}} \mathbf{\Lambda}_k^{\mathrm{s}})[n,n'] & \text{if } \mathbf{S}_n^{\mathrm{t}} \text{ near } \mathbf{S}_{n'}^{\mathrm{s}} \\ 0 & \text{otherwise} \end{cases} \tag{2.2.40}$$

for $1 \le n, n' \le N$ and $\mathrm{t,s} \in \{\mathrm{a,i}\}$.

When Green-function modification is used, the multiple-grid AIM must approximate the $\mathbf{X}_k^{\mathrm{aa}}$ and (when they exist) $\mathbf{X}_k^{\mathrm{ai}}$ matrices in (2.2.34). A simple approach is to use the same auxiliary grids as in the brute-force imaging approach but map only the actual currents for $\mathbf{X}_k^{\mathrm{aa}}$ and image currents for $\mathbf{X}_k^{\mathrm{ai}}$ (for $0 \le k \le 1$):

---

[3] Precisely, the FFT of a zero-padded coefficient vector, the FFT of a vector containing unique entries of the Toeplitz matrix, their multiplication, and the inverse FFT of the result are computed in $O(8N_k^{\mathrm{C}} \log 8N_k^{\mathrm{C}})$, $O(8N_k^{\mathrm{C}} \log 8N_k^{\mathrm{C}})$, $O(8N_k^{\mathrm{C}})$, and $O(8N_k^{\mathrm{C}} \log 8N_k^{\mathrm{C}})$ operations, respectively. By pre-computing and storing the FFT for the matrix, each Green function matrix is multiplied in $O(16N_k^{\mathrm{C}} \log 8N_k^{\mathrm{C}} + 8N_k^{\mathrm{C}})$ operations per iteration [8].

$$\begin{aligned}\mathbf{X}_k^{\mathrm{aa}} &\approx \mathbf{X}_k^{\mathrm{near,aa}} + \mathbf{\Lambda}_k^{\mathrm{a}\dagger}\mathbf{X}_k^{\mathrm{FFT}}\mathbf{\Lambda}_k^{\mathrm{a}} \\ \mathbf{X}_k^{\mathrm{ai}} &\approx \mathbf{X}_k^{\mathrm{near,ai}} + \mathbf{\Lambda}_k^{\mathrm{a}\dagger}\mathbf{X}_k^{\mathrm{FFT}}\mathbf{\Lambda}_k^{\mathrm{i}}\end{aligned} \tag{2.2.41}$$

Compared to brute-force imaging, this approach halves the cost of near-zone corrections but it does not change the FFT costs for regions where the auxiliary grid encloses both an actual and an image structure, e.g., the free-space region in Fig. 2.2.1. It is more efficient to modify the Green functions and approximate the MOM matrices as:

$$\mathbf{X}_k^{\mathrm{aa}} \mp \mathbf{X}_k^{\mathrm{ai}} \approx \mathbf{X}_k^{\mathrm{near,aa}} \mp \mathbf{X}_k^{\mathrm{near,ai}} + \mathbf{\Lambda}_k^{\mathrm{a}\dagger}(\mathbf{X}_{k,\mathrm{T}}^{\mathrm{FFT}} \mp \mathbf{X}_{k,\mathrm{H}}^{\mathrm{FFT}})\mathbf{\Lambda}_k^{\mathrm{a}} \tag{2.2.42}$$

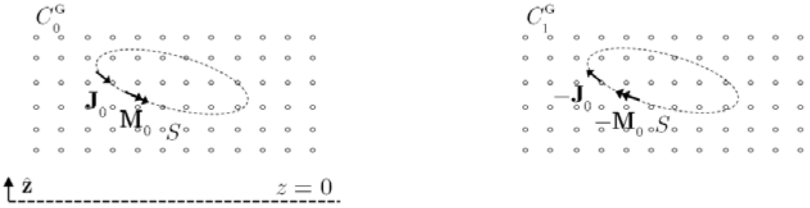

(a) (b)

Figure 2.2.4: The two multiple-grid AIM auxiliary grids used for Green-function modification: (a) C_0^{G} and (b) C_1^{G}.

In this approach, the propagation and reflection matrices ($\mathbf{X}_{k,\mathrm{T}}^{\mathrm{FFT}}$ and $\mathbf{X}_{k,\mathrm{H}}^{\mathrm{FFT}}$) are constructed using identical auxiliary grids, which enclose only actual structures (Fig. 2.2.4). Let C_k^{G} denote this smaller auxiliary grid with $N_k^{\mathrm{G}} = \delta_k N_k^{\mathrm{C}}$ grid points for region k; if region k is terminated on the plane, then $\delta_k \le 0.5$; if it resides above the plane, then $\delta_k = 1$; if it resides below the plane, then $\delta_k = 0$ (i.e., C_k^{G} is not defined); e.g., $\delta_0 < 0.5$, $\delta_1 = 1$ and $\delta_2 = 0$ for the problem in Fig. 2.2.1. The propagation and reflection matrices are constructed as in (2.2.37) using the $N_k^{\mathrm{G}} \times N_k^{\mathrm{G}}$ Green function matrices

$$\mathbf{G}_{k,\mathrm{P}}^{\mathrm{x,y,z,A},\phi}[u,u'] = \{\partial_x, \partial_y, \partial_z, \gamma_k, 1/\gamma_k\} g_{k,\mathrm{P}}(\mathbf{r}_u, \mathbf{r}_{u'}) \tag{2.2.43}$$

for $\mathrm{P} \in \{\mathrm{T}, \mathrm{H}\}$ and nodes u and u' on C_k^{G} ($\mathbf{G}_{k,\mathrm{P}}^{\mathrm{x,y,z,A},\phi}[u,u] = 0$). Here, $g_{k,\mathrm{T}}(\mathbf{r},\mathbf{r}') = g_k(\mathbf{r},\mathbf{r}')$ is in convolution form in all directions and $g_{k,\mathrm{H}}(\mathbf{r},\mathbf{r}') = g_k(\mathbf{r},\tilde{\mathbf{r}}')$ is in correlation form in the direction normal to the PEC plane; thus, $\mathbf{G}_{k,\mathrm{T}}$ is a (three level) block-Toeplitz matrix and $\mathbf{G}_{k,\mathrm{H}}$ is a Hankel-(two level)block-Toeplitz matrix. FFTs can be used for fast multiplication of these matrices as detailed next [29, 30].

For example, consider $\mathbf{G}_{k,\mathrm{H}}^{\phi}$ when C_k^{G} is just a one-dimensional grid along the *z* axis. Then,

$$\mathbf{G}_{k,\mathrm{H}}^{\phi} = \begin{bmatrix} 0 & g_{k,\mathrm{H}}(\mathbf{r}_1, \mathbf{r}_2) & \cdots & g_{k,\mathrm{H}}(\mathbf{r}_1, \mathbf{r}_{N_k^{\mathrm{G}}}) \\ g_{k,\mathrm{H}}(\mathbf{r}_2, \mathbf{r}_1) & & \iddots & g_{k,\mathrm{H}}(\mathbf{r}_2, \mathbf{r}_{N_k^{\mathrm{G}}}) \\ \vdots & & \iddots & \vdots \\ g_{k,\mathrm{H}}(\mathbf{r}_{N_k^{\mathrm{G}}}, \mathbf{r}_1) & g_{k,\mathrm{H}}(\mathbf{r}_{N_k^{\mathrm{G}}}, \mathbf{r}_2) & \cdots & 0 \end{bmatrix} \tag{2.2.44}$$

is a Hankel matrix (it has constant skew-diagonals). A Hankel matrix-vector multiplication can be converted to a Toeplitz one by using the anti-diagonal permutation matrix $\mathbf{P}$ [30]; e.g., $\mathbf{G}_{k,\mathrm{H}}^{\phi}\mathbf{\Lambda}_k^{\mathrm{a},\nabla}\mathbf{I} = (\mathbf{G}_{k,\mathrm{H}}^{\phi}\mathbf{P})(\mathbf{P}^{-1}\mathbf{\Lambda}_k^{\mathrm{a},\nabla}\mathbf{I})$, where $\mathbf{P}^{-1}\mathbf{\Lambda}_k^{\mathrm{a},\nabla}\mathbf{I}$ simply re-orders the vector $\mathbf{\Lambda}_k^{\mathrm{a},\nabla}\mathbf{I}$ upside down and $\mathbf{G}_{k,\mathrm{H}}^{\phi}\mathbf{P}$ is a Toeplitz matrix that can be multiplied as usual. A similar approach is applicable when C_k^{G} is three dimensional (by using a block-anti-diagonal permutation matrix) and the multiplication can be calculated in $O(16N_k^{\mathrm{G}} \log 8N_k^{\mathrm{G}} + 8N_k^{\mathrm{G}})$ operations if the FFT for the matrix is pre-computed. Even fewer operations are needed if the FFTs used for calculating $\mathbf{\Lambda}_k^{\mathrm{a}\nabla\dagger}\mathbf{G}_{k,\mathrm{T}}^{\phi}\mathbf{\Lambda}_k^{\mathrm{a}\nabla}\mathbf{I}$ are recycled: (i) Calculate the FFT of a zero-padded vector for $\mathbf{\Lambda}_k^{\mathrm{a},\nabla}\mathbf{I}$ and store it in $\overline{\mathbf{I}}_k^{\mathrm{a},\nabla}$. (ii) Multiply $\overline{\mathbf{I}}_k^{\mathrm{a},\nabla}$ element-by-element with the pre-computed FFT for $\mathbf{G}_{k,\mathrm{T}}^{\phi}$. (iii) Find the FFT for the re-ordered vector $\mathbf{P}^{-1}\mathbf{\Lambda}_k^{\mathrm{a},\nabla}\mathbf{I}$ by multiplying each element of $\overline{\mathbf{I}}_k^{\mathrm{a},\nabla}$ with the pre-computed FFT for $\mathbf{G}_{k,\mathrm{H}}^{\phi}\mathbf{P}$ that is multiplied by a phase shift term (to account for the re-ordering). (iv) Combine the vectors found in (ii) and (iii) according to (2.2.34) and calculate the inverse FFT of the resulting vector. These require $O(8N_k^{\mathrm{G}} \log 8N_k^{\mathrm{G}})$, $O(8N_k^{\mathrm{G}})$, $O(8N_k^{\mathrm{G}})$ and $O(8N_k^{\mathrm{G}} \log 8N_k^{\mathrm{G}})$ operations, respectively; thus, only $O(8N_k^{\mathrm{G}})$ extra operations produce $\mathbf{\Lambda}_k^{\mathrm{a}\nabla\dagger}(\mathbf{G}_{k,\mathrm{T}}^{\phi} \mp \mathbf{G}_{k,\mathrm{H}}^{\phi})\mathbf{\Lambda}_k^{\mathrm{a}\nabla}\mathbf{I}$.

2.2.4. Multiple-Grid AIM Computational Complexity

When BFI is used, the multiple-grid AIM requires, for each region k, $O(N_k^{\mathrm{nz,near}} + 8N_k^{\mathrm{C}})$ bytes/operations to fill the non-zero and unique entries of $\mathbf{X}_k^{\mathrm{near}}$ and $\mathbf{X}_k^{\mathrm{FFT}}$ and $O(N_k^{\mathrm{nz,near}} + 8[16N_k^{\mathrm{C}} \log 8N_k^{\mathrm{C}} + 8N_k^{\mathrm{C}}] + 12N_k^{\mathrm{C}})$ operations per iteration to multiply them[4]. When GFM is used, only $\mathbf{X}_k^{\mathrm{near,aa}}$ and $\mathbf{X}_{k,\mathrm{T}}^{\mathrm{FFT}}$ exist if $\delta_k \in \{0,1\}$ and the multiple-grid AIM requires $O(\delta_k N_k^{\mathrm{nz,near}} + 8N_k^{\mathrm{G}})$ bytes/operations to fill the unique entries of these matrices and $O(\delta_k N_k^{\mathrm{nz,near}} + 8[16N_k^{\mathrm{G}} \log 8N_k^{\mathrm{G}} + 8N_k^{\mathrm{G}}] + 12N_k^{\mathrm{G}})$ operations per iteration to multiply them. Therefore, GFM exactly halves the computational costs for regions not terminated on the plane. For regions that are terminated on the plane ($\delta_k \leq 0.5$), GFM reduces the cost by a factor of $1/\delta_k$; this can be a very large factor if the structure is high above the plane (when $\delta_k \ll 0.5$). When $\delta_k \leq 0.5$, however, $\mathbf{X}_k^{\mathrm{near,ai}}$ and $\mathbf{X}_{k,\mathrm{H}}^{\mathrm{FFT}}$ also exist and an additional $O(8N_k^{\mathrm{G}})$ bytes/operations are needed to fill them and $O(64N_k^{\mathrm{G}})$ operations are needed to multiply them per iteration. While these additional costs reduce the $1/\delta_k$ gain, this is offset by several factors: (i) The correction cost is generally not negligible, i.e., rarely is $N_k^{\mathrm{nz,near}} \ll N_k^{\mathrm{G}}$. (ii) In the solution time, FFT cost dominates the multiplication cost by a logarithmic factor and the reduction in the FFT cost is greater than $1/\delta_k$ (by a logarithmic factor).

2.2.5. Numerical Results

This section presents numerical examples that contrast the two imaging approaches. In all simulations, the average edge length on a surface is set to ~1/10th of the smallest wavelength of (ordinary) waves in the regions bounded by that surface. All

---

[4] Here, it is assumed that only 8 block-Toeplitz matrix-vector multiplications are calculated via FFTs per iteration. This can be achieved by approximating the spatial derivatives in $\mathbf{K}_k^{\mathrm{FFT}}$ with finite differences, i.e., the multiplication of $\mathbf{K}_k^{\mathrm{FFT}}$ with a vector is computed from the multiplication of $\mathbf{L}_k^{\mathrm{FFT}}$ with that vector in $O(6N_k^{\mathrm{C}})$ operations [23].

the multiple-grid AIM simulation parameters, e.g., moment matching order, near-zone size, etc. are chosen as in Section 2.1.5. Each structure is excited by a plane wave polarized along $(\theta, \phi) = (45^o, 0^o)$ and propagating to $(\theta, \phi) = (135^o, 0^o)$ direction.

2.2.5.1. Accuracy, Efficiency, and Impact of Height

First, scattering of a 200 MHz plane wave from a 4 m diameter dielectric sphere of permittivity $\varepsilon_1 = 2\varepsilon_0$ that is located H meters above a PEC plane, illustrated in Fig. 2.2.5(a), is analyzed. The MOM and multiple-grid AIM using brute-force imaging and Green-function modification (MOM-BFI, MOM-GFM, MG-AIM-BFI, MG-AIM-GFM) are contrasted when the sphere is close to ($H = 0.25$) and far from ($H = 5$) the plane. The sphere surface is meshed using $N = 10\ 947$ edges and $N_0^{\mathrm{G}} = N_1^{\mathrm{G}} = N_0^{\mathrm{C}} = 40^3$ in either scenario but N_1^{C} increases from 40^3 to $40^2 \times 160$ in the latter case. Fig. 2.2.5(b)-(c) validate that the multiple-grid AIM acceleration produces visually identical RCS results with MOM; they also show that the two imaging approaches produce practically identical results. Table 2.2.1 summarizes their computational requirements and shows that (i) MOM performance is insensitive to the height above the PEC plane and Green-function modification reduces all costs by a factor of 2; (ii) MG-AIM-BFI becomes less efficient with larger H but remains more efficient than MOM in all performance measures; and (ii) MG-AIM-GFM is the most efficient method, is insensitive to H, and can reduce all costs by at least a factor of 2.

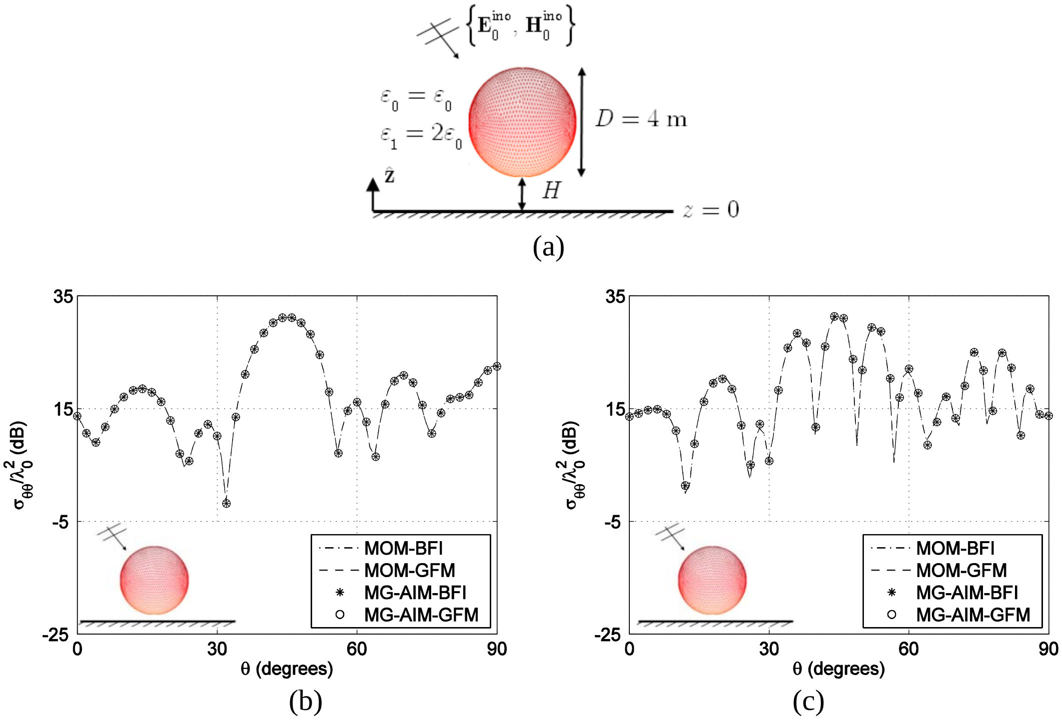

(a)

(b)

(c)

Figure 2.2.5: VV-polarized RCS in the $x-z$ plane for a dielectric sphere H m above the PEC plane: (a) Configuration. (b) $H = 0.25$. (c) $H = 5$.

Table 2.2.1: Performance of EH-PMCHWT solvers for a dielectric sphere above a PEC plane

Method		Fill Time (s)	Solve Time per Iteration (s)	Number of Iterations	Memory (GB)
MOM-BFI		23 784	35.12	320	24.2
MOM-GFM		11 818	17.35	311	12.0
MG-AIM-BFI	$H = 0.25$	1630	8.57	320	1.4
	$H = 5$	1620	11.70	385	1.5
MG-AIM-GFM	$H = 0.25$	814	4.20	311	0.72
	$H = 5$	811	4.19	349	0.71

2.2.5.2. Scalability with Number of Regions

Next, the scalability of the multiple-grid AIM imaging schemes are evaluated for multi-region problems as the number of regions increases. As in Section 2.1, two extreme scaling methods are used and new regions are added either recursively or in parallel exemplified by a layered hemisphere and a dielectric-rod array on a PEC plane as the number of layers and rods is increased, respectively. Notice that, these are best case scenarios for BFI because the space filling effect due to height is minimal and because GFM must introduce half basis functions. The geometrical (hemisphere radii and cylinder spacing), material (permittivity and conductivity), and mesh (edge length) parameters of the structures are chosen identical to those of the largest layered sphere and the dielectric-rod array in the scalability study in Section 2.1.5, i.e., once the plane is removed and the image of the structure is introduced, each scattering problem is identical (except for the incident field) to that in Section 2.1.5. As a result, the MG-AIM-BFI solves for identical number of unknowns using identical grids, etc. as in Section 2.1.5. Both problems are scaled up to $N > 10^6$ edges. Fig. 2.2.6 shows that all multiple-grid AIM computational costs scale linearly with the number of regions for these structures as Section 2.1.5 and GFM (almost) halves all costs compared to BFI as expected.

2.2.6. Summary

This section presented and contrasted two imaging approaches for multiple-grid AIM accelerated MOM analysis of scattering from piecewise homogeneous structures residing on or above a PEC/PMC plane. Analysis and numerical results showed that modifying Green functions reduces the simulation time and memory requirement by a factor of (almost) 2 or larger compared to the brute force approach if the structure of interest is terminated on or resides above the plane, respectively. This is attained by solving for fewer unknowns, using smaller auxiliary grids, and recycling FFTs.

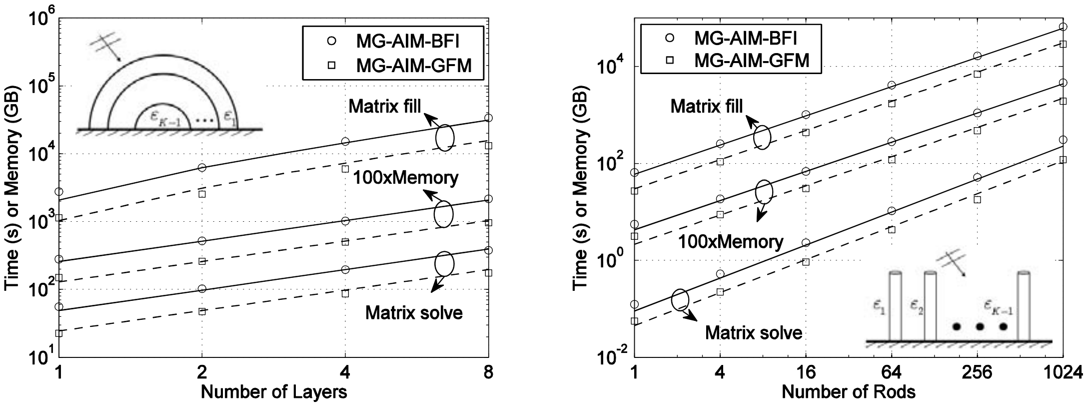

(a) (b)

Figure 2.2.6: Green function modification (GFM) vs. brute-force imaging (BFI) for the multiple-grid AIM as the number of regions K increases. (a) Layered hemispheres. All lines are parallel to $2K - 3$ except those for the solve time, which are parallel to $K - 1$. (b) Dielectric-rod arrays. All lines are parallel to K. In both figures, solid lines are drawn by fitting to the measured data and the dashed lines are drawn by halving the slope of the corresponding solid lines.

2.3. MODELING METAMATERIAL REGIONS

The above EH-PMCHWT formulation is applicable to metamaterial regions with negative permittivity or permeability, provided that the wave impedance and propagation constant are chosen carefully. Using the notation in Section 2.1, let region R_k be an arbitrary penetrable material in the above formulation, i.e., it can be a conventional double-positive (DPS) material, a double-negative (DNG) material, an epsilon-negative (ENG) material, or a mu-negative (MNG) material. This leads to complications when calculating $\gamma_k = j\omega\sqrt{\varepsilon_k \mu_k}$ and $\eta_k = \sqrt{\mu_k / \varepsilon_k}$ as the correct roots must be selected in these expressions to satisfy physical principles [31, 32], i.e., $\mathrm{Re}\{\gamma_k\} > 0$ to ensure conservation of energy and $\mathrm{Re}\{\eta_k\} > 0$ to ensure the material is passive. Moreover, for lossless DNG (DPS) materials, the condition that $\mathrm{Im}\{\gamma_k\} < 0$ $(\mathrm{Im}\{\gamma_k\} > 0)$ must be explicitly enforced since $\mathrm{Re}\{\gamma_k\} = 0$; similarly for lossless ENG (MNG) materials $\mathrm{Im}\{\eta_k\} > 0$ $(\mathrm{Im}\{\eta_k\} < 0)$ should be explicitly enforced since $\mathrm{Re}\{\eta_k\} = 0$.

2.3.1. Validation

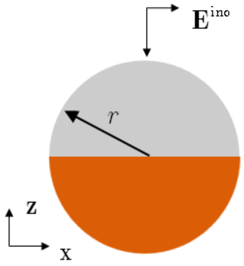

Figure 2.3.1: Scattering from a homogenous sphere of radius $r = 1\,\mathrm{m}$. The sphere is artificially modeled as composed of two different hemispherical regions (with the same constitutive parameters). Unnecessary regular and junction edges are introduced on the center plane and at the intersection of the hemispheres, respectively, in order to validate junction and multi-region implementations.

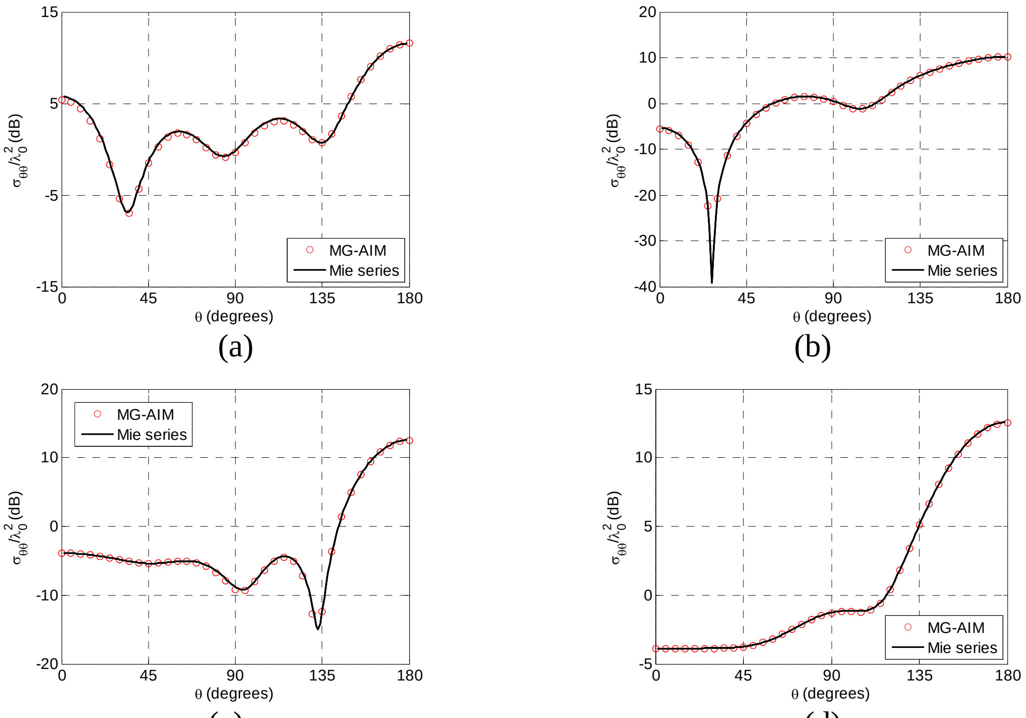

(a) (b)

(c) (d)

Figure 2.3.2: Validation for metamaterial regions for the EH-PMCHWT equations. VV-polarized RCS in the $x-z$ plane at 150 MHz for the homogeneous sphere in Fig. 2.3.1 for the (a) DPS-DPS, (b) DNG-DNG, (c) ENG-ENG, and (d) MNG-MNG configuration.

To validate the extension to metamaterial regions, consider a 1-m radius homogeneous sphere that is modeled as a 3-region structure as shown in Fig. 2.3.1. To test the junction implementation, the top-bottom hemispheres are filled with identical DPS-DPS, DNG-DNG, ENG-ENG, or MNG-MNG materials and the fields scattered by this sphere are compared to those scattered from a homogeneous DPS, DNG, ENG, and MNG sphere with constitutive parameters $\{4\varepsilon_0, \mu_0\}$, $\{-4\varepsilon_0, -\mu_0\}$, $\{(-1-j)\varepsilon_0, \mu_0\}$, and $\{\varepsilon_0, (-1-j)\mu_0\}$, respectively. The sphere is illuminated by a 150 MHz $\hat{x}$-polarized plane wave propagating in $-\hat{z}$-direction and is discretized using $N = 15\ 606$ edges of which 126 are junction edges. The AIM grids are chosen such that $N_0^{\mathrm{C}} = 24^3$ and $N_1^{\mathrm{C}} = N_2^{\mathrm{C}} = 40^2 \times 24$. Fig. 2.3.2 compares the RCS for the 3-region structures to the analytical Mie series results. Excellent agreement is observed in all cases, which validates the extension of the method to metamaterial regions.

In some cases, the scattering problem for piecewise homogeneous structures involving metamaterial regions might be ill-posed. This has been attributed to the so-called surface-plasmon resonance condition [33, 34]; for a half-space problem with an interface at the $z = 0$ plane, this condition is observed when the constitutive parameters of the two materials satisfy $\mu_1 k_{2z} + \mu_2 k_{1z} = 0$, where, $k_{iz} = \sqrt{k_i^2 - k_\rho^2}$, k_ρ is the radial propagation component, and $k_i^2 = \omega^2 \varepsilon_i \mu_i$ for $i = 1, 2$ [33]. To investigate this ill-posedness problem, scattering from a homogeneous DNG sphere is simulated. The sphere has a radius of 1 m and is excited by an $\hat{x}$-polarized plane wave propagating in $\hat{z}$-direction at 300 MHz and is discretized using $N = 8\ 007$ edges. Fig. 2.3.3 shows the RCS when the sphere parameters are $\{-3\varepsilon_0, -\mu_0\}$ or $\{-1.5\varepsilon_0, -1.5\mu_0\}$. In both scenarios, the results from the EH-PMCHWT solver agree with the analytical solution without adding any small losses. This is in stark contrast to the implementation in [33], which agrees well with the analytical solution in the first case but requires artificial small losses, i.e., changes the material parameters to $\{(-1.5 - j10^{-4})\varepsilon_0, (-1.5 - j10^{-4})\mu_0\}$, to avoid the ill-posedness problem in the second case. This example indicates that the EH-PMCHWT solution does not suffer from surface-plasmon resonance. Note that, if the sphere is filled with $\{-\varepsilon_0, -\mu_0\}$, the EH-PMCHWT solver will encounter the ill-posedness problem as all previous investigations [33, 35], but this is due to the fact that all diagonal entries from DPS and DNG regions are almost canceled during the combination step of EH-PMCHWT formulation, which deteriorates the conditioning of the matrix system.

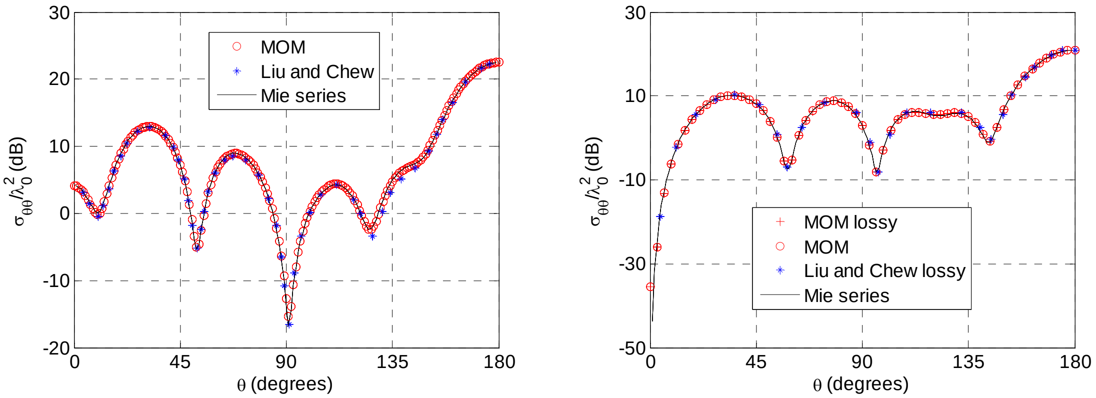

(a) (b)

Figure 2.3.3: Well-posedness of EH-PMCHWT solution for the DPS-DNG interface. VV-polarized RCS in the $x-z$ plane at 300 MHz for a 1-m radius DNG sphere: (a) $\{-3\varepsilon_0, -\mu_0\}$. (b) $\{-1.5\varepsilon_0, -1.5\mu_0\}$.

2.4. MODELING PEC/PMC REGIONS AND MATERIAL-PEC/PMC JUNCTIONS

For structures that include PEC/PMC regions and material-PEC/PMC junctions, the EH-PMCHWT formulation in Section 2.1 is not directly applicable and must be augmented. When closed PEC/PMC regions are present, the following modifications are implemented: No (internal) equivalent problems are formulated for them; only $\mathbf{J}_k$ or $\mathbf{M}_k$ is defined on S_k; and two additional integral equations, the rotated version of tangential electrical- and magnetic- integral equations (N-EFIE and N-MFIE), are formulated for S_k:

$$\begin{aligned} -\hat{\mathbf{n}}_{kl} \times \mathbf{E}_k - \mathbf{M}_{kl} &= \mathbf{0} \quad (\text{N-EFIE}_{kl}) \\ \hat{\mathbf{n}}_{kl} \times \mathbf{H}_k - \mathbf{J}_{kl} &= \mathbf{0} \quad (\text{N-MFIE}_{kl}) \end{aligned} \tag{2.4.1}$$

For a PEC (PMC) region, only J-CFIEs (M-CFIEs), which are the linear combination of T-EFIE_{kl} (T-MFIE_{kl}) with N-MFIE_{kl} (N-EFIE_{kl}), are enforced on S_k:

$$\begin{aligned} \text{J-CFIE}_{kl} &= 1/\eta_k \, \text{T-EFIE}_{kl} + \text{N-MFIE}_{kl} \quad \text{for PEC region} \\ \text{M-CFIE}_{kl} &= \text{N-EFIE}_{kl} + \eta_k \text{T-MFIE}_{kl} \quad \text{for PMC region} \end{aligned} \tag{2.4.2}$$

The J-CFIEs (M-CFIEs) formulated for PEC (PMC) regions are concatenated with the EH-PMCHWT equations for the magnetodielectric regions [21, 36].

$$\sum_k \sum_l \beta_{kl} \begin{cases} \text{J-CFIE}_{kl} & \text{if } R_l \text{ is a PEC region} \\ \text{M-CFIE}_{kl} & \text{if } R_l \text{ is a PMC region} \\ \text{T-EFIE}_{kl} & \multirow{2}{*}{else} \\ \text{T-MFIE}_{kl} & \end{cases} \tag{2.4.3}$$

where $\beta_{kl} = \hat{\mathbf{p}}_{kl} \bullet \hat{\mathbf{n}}_{kl}$.

The above combination of CFIEs for PEC/PMC regions and EH-PMCHWT equations for magnetodielectric ones is free of internal resonance problems [21]; however, it requires several modifications to the methods in Section 2.1-2.3: (i) Additional integral operators are needed because the presence of N-EFIE and N-MFIE, which requires additional integrations for MOM and modified interpolation and pre-correction stages for multiple-grid AIM that use new mapping/interpolation coefficients. (ii) Magnetic (Electrical) current unknowns should not be defined on the surfaces of PEC (PMC) regions because tangential electric (magnetic) fields are zero. (iii) J-CFIE (M-CFIE) should be enforced and M-CFIE (J-CFIE) must be removed at material-PEC (material-PMC) junctions because there are fewer degrees of freedom. These modifications are presented in more detail in Sections 3.1 and 3.4.

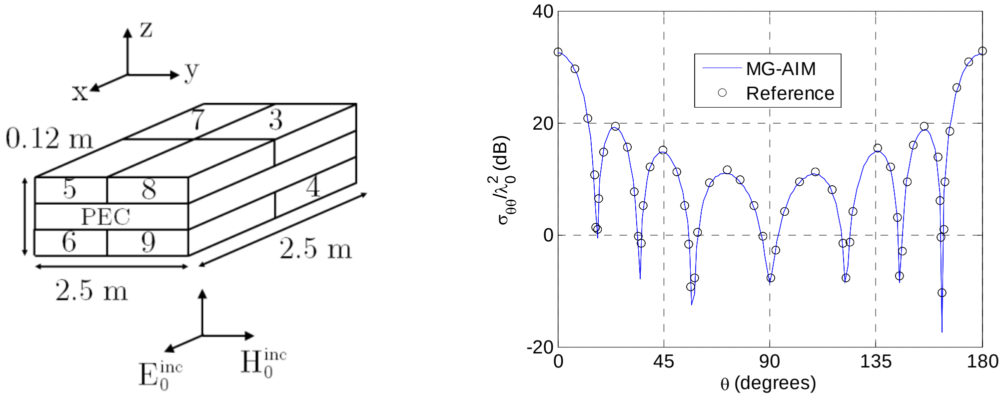

(a) (b)

Figure 2.4.1: RCS of a composite structure: (a) Configuration. (b) Comparison between the EH-PMCHWT solver and the reference.

2.4.1. Validation

To validate the extension of multiple-grid AIM for composite structures, scattering from a structure composed of dielectric and PEC regions and dielectric-PEC and dielectric-dielectric junctions is analyzed at 400 MHz. As Fig. 2.4.1(a) shows, the structure has three layers; 4 dielectric regions at the top and bottom and a PEC region at the center; the relative permittivities range from 3 to 9 [37]. The composite structure is excited by an $\hat{x}$-polarized plane wave propagating toward the $\hat{z}$ direction. The structure is meshed such that the average edge length is ~1/10th of the smallest wavelength in all regions which results in $N = 128\ 788$ (1 620 junction edges) at 400

MHz. Fig. 2.4.1 shows the good agreement between EH-PMCHWT multiple-grid AIM and the reference results obtained by a finite-element boundary-integral equation solver at 400 MHz [37], validating the extension.

Chapter III Multiple-Grid AIM for CC-PMCHWT Equations

This chapter presents the multiple-grid AIM approach for the CC-PMCHWT formulation, which improves the convergence of the iterative MOM solution. The presentation follows the same order as in Chapter 2: First, the method is formulated for piecewise homogeneous structures composed of conventional magnetodielectric materials in free space, then for such structures in the presence of a PEC/PMC plane, then for those containing metamaterial regions, and finally for arbitrary composite structures composed of PEC/PMC regions and material-PEC/PMC junctions.

3.1. PIECEWISE HOMOGENEOUS STRUCTURES

In this section, the CC-PMCHWT equations for analyzing scattering from piecewise homogeneous structures are formulated. Then, their MOM solution and the multiple-grid AIM acceleration are detailed. Numerical results investigating the effectiveness of the formulation conclude this section. The notation in this chapter follows and extends that in Chapter 2.

3.1.1. CC-PMCHWT Formulation

Consider the K-region scattering problem in Fig. 2.1.1(a). The CC-PMCHWT equations are derived in four steps similar to the EH-PMCHWT equations. The first three steps, i.e., the formulation of equivalent problems, the definition of preferred currents, and the incident/scattered field decomposition, are identical to those when deriving the EH-PMCHWT equations as detailed in Section 2.1.2. In the fourth step, however, electric and magnetic current combined field integral equations (JCFIEs and MCFIEs) [13] are formulated and combined according to the PMCHWT recipe instead of the T-EFIEs and T-MFIEs. The JCFIE and MCFIE for each surface S_{kl} is given as

$$
\begin{aligned}
\text{JCFIE}_{kl} &= \frac{1}{\eta_k}\text{T-EFIE}_{kl} + \text{N-MFIE}_{kl} \\
\text{MCFIE}_{kl} &= \text{N-EFIE}_{kl} + \eta_k \text{T-MFIE}_{kl}
\end{aligned}
\qquad (3.1.1)
$$

where

$$
\begin{aligned}
-\hat{\mathbf{n}}_{kl} \times \hat{\mathbf{n}}_{kl} \times \mathbf{E}_k - \hat{\mathbf{n}}_{kl} \times \mathbf{M}_{kl} &= \mathbf{0} \quad (\text{T-EFIE}_{kl}) \\
-\hat{\mathbf{n}}_{kl} \times \hat{\mathbf{n}}_{kl} \times \mathbf{H}_k + \hat{\mathbf{n}}_{kl} \times \mathbf{J}_{kl} &= \mathbf{0} \quad (\text{T-MFIE}_{kl}) \\
-\hat{\mathbf{n}}_{kl} \times \mathbf{E}_k - \mathbf{M}_{kl} &= \mathbf{0} \quad (\text{N-EFIE}_{kl}) \\
\hat{\mathbf{n}}_{kl} \times \mathbf{H}_k - \mathbf{J}_{kl} &= \mathbf{0} \quad (\text{N-MFIE}_{kl})
\end{aligned}
\qquad (3.1.2)
$$

As a result, the linear combination of the JCFIEs and MCFIEs according to the PMCHWT recipe yields:

$$
\begin{aligned}
&\sum_k \sum_l \beta_{kl} \text{JCFIE}_{kl} \quad (\text{JC})\text{PMCHWT} \\
&\sum_k \sum_l \beta_{kl} \text{MCFIE}_{kl} \quad (\text{MC})\text{PMCHWT}
\end{aligned}
\qquad (3.1.3)
$$

where $\beta_{kl} = \hat{\mathbf{p}}_{kl} \bullet \hat{\mathbf{n}}_{kl}$. This combination is commonly referred to as the JMCFIE formulation [13, 16-18]; however, it is called the CC-PMCHWT formulation in this dissertation to emphasize that the CFIE equations are combined similar to the EH-PMCHWT recipe and to highlight that the formulation is different from the better known CFIE formulations for multi-region problems [19, 38] that enforce the JCFIEs for each equivalent problem separately (rather than combining them). While the CC-PMCHWT formulation can be traced to [19], it has been popularized by [13].

3.1.2. MOM

Following the procedure in Section 2.1.3, a set of integral equations for the preferred currents is obtained and converted to a system of linear equations by the usual MOM steps: The surfaces are meshed, the currents are approximated using RWG and half-RWG functions, and the SIEs are weighted by testing functions. Similar to (2.1.12), this results in the following $2N$ equations for $2N$ unknowns

$$ {}^{\mathrm{CC}}\mathbf{Z}\begin{bmatrix}\mathbf{I}\\ \mathbf{V}\end{bmatrix}=\begin{bmatrix}{}^{\mathrm{CC}}\mathbf{V}^{\mathrm{inc}}\\ {}^{\mathrm{CC}}\mathbf{I}^{\mathrm{inc}}\end{bmatrix} \tag{3.1.4} $$

As in Section 2.1.3, the MOM matrix assembly can be formulated using the local notation as

$$ \begin{gathered} {}^{\mathrm{CC}}\mathbf{Z}=\sum_k\sum_l\beta_{kl}\begin{bmatrix}\mathbf{C}_{kl}^T & \mathbf{0}\\ \mathbf{0} & \mathbf{C}_{kl}^T\end{bmatrix}{}^{\mathrm{CC}}\mathbf{Z}_{kl}\\ \begin{bmatrix}{}^{\mathrm{CC}}\mathbf{V}^{\mathrm{inc}}\\ {}^{\mathrm{CC}}\mathbf{I}^{\mathrm{inc}}\end{bmatrix}=\sum_k\sum_l\beta_{kl}\begin{bmatrix}\mathbf{C}_{kl}^T & \mathbf{0}\\ \mathbf{0} & \mathbf{C}_{kl}^T\end{bmatrix}\begin{bmatrix}{}^{\mathrm{CC}}\mathbf{V}_{kl}^{\mathrm{inc}}\\ {}^{\mathrm{CC}}\mathbf{I}_{kl}^{\mathrm{inc}}\end{bmatrix} \end{gathered} \tag{3.1.5} $$

Thus, the counterpart of (2.1.14) is

$$ {}^{\mathrm{CC}}\mathbf{Z}_{kl}\begin{bmatrix}\mathbf{I}\\ \mathbf{V}\end{bmatrix}=\begin{bmatrix}{}^{\mathrm{CC}}\mathbf{V}_{kl}^{\mathrm{inc}}\\ {}^{\mathrm{CC}}\mathbf{I}_{kl}^{\mathrm{inc}}\end{bmatrix} \tag{3.1.6} $$

The matrices and vectors in (3.1.5) and (3.1.6) have the same number of non-zero entries as the ones in (2.1.13) and (2.1.14). The vectors ${}^{\mathrm{CC}}\mathbf{V}_{kl}^{\mathrm{inc}}$ and ${}^{\mathrm{CC}}\mathbf{I}_{kl}^{\mathrm{inc}}$ store the incident fields tested on surface S_{kl}. The matrix ${}^{\mathrm{CC}}\mathbf{Z}_{kl}$ relates the scattered fields tested on surface S_{kl} to the currents on the entire structure. It can be expanded as

$$ {}^{\mathrm{CC}}\mathbf{Z}_{kl}=\sum_{l'=0,l'\neq k}^{K-1}\underbrace{\begin{bmatrix}(\mathbf{L}_{kll'}-{}_{\times}\mathbf{K}_{kll'}+2\mathbf{T}_{kll'}) & ({}_{\times}\mathbf{L}_{kll'}+\mathbf{K}_{kll'}+2\,{}_{\times}\mathbf{T}_{kll'})/\eta_k\\ -\eta_k({}_{\times}\mathbf{L}_{kll'}+\mathbf{K}_{kll'}+2\,{}_{\times}\mathbf{T}_{kll'}) & (\mathbf{L}_{kll'}-{}_{\times}\mathbf{K}_{kll'}+2\mathbf{T}_{kll'})\end{bmatrix}}_{{}^{\mathrm{CC}}\mathbf{Z}_{kll'}}\alpha_{kl'}\begin{bmatrix}\mathbf{C}_{kl'} & \mathbf{0}\\ \mathbf{0} & \mathbf{C}_{kl'}\end{bmatrix} \tag{3.1.7} $$

Similar to ${}^{\mathrm{EH}}\mathbf{Z}_{kll'}$ in (2.1.15), ${}^{\mathrm{CC}}\mathbf{Z}_{kll'}$, which is a $2N_{kl}\times 2N_{kl'}$ dense matrix, relates the scattered fields tested on surface S_{kl} to the currents only on $S_{kl'}$. The entries of ${}^{\mathrm{CC}}\mathbf{V}_{kl}^{\mathrm{inc}}$, ${}^{\mathrm{CC}}\mathbf{I}_{kl}^{\mathrm{inc}}$, and ${}^{\mathrm{CC}}\mathbf{Z}_{kll'}$ are given as

$$ \begin{gathered} {}^{\mathrm{CC}}\mathbf{V}_{kl}^{\mathrm{inc}}[n]=\iint_{S_{kl}}\mathbf{S}_{kl,n}(\mathbf{r})\bullet\left[\mathbf{E}_k^{\mathrm{inc}}(\mathbf{r})/\eta_k+\hat{\mathbf{n}}_{kl}\times\mathbf{H}_k^{\mathrm{inc}}(\mathbf{r})\right]ds\\ {}^{\mathrm{CC}}\mathbf{I}_{kl}^{\mathrm{inc}}[n]=\iint_{S_{kl}}\mathbf{S}_{kl,n}(\mathbf{r})\bullet\left[\eta_k\mathbf{H}_k^{\mathrm{inc}}(\mathbf{r})-\hat{\mathbf{n}}_{kl}\times\mathbf{E}_k^{\mathrm{inc}}(\mathbf{r})\right]ds \end{gathered} \tag{3.1.8} $$

$$
\begin{aligned}
\mathbf{K}_{kll'}[n,n'] &= \iint_{S_{kl}} \mathbf{S}_{kl,n}(\mathbf{r}) \bullet \mathcal{K}_{k}(\mathbf{S}_{kl',n'},\mathbf{r})ds \\
&= \iint_{S_{kl}} \mathbf{S}_{kl,n}(\mathbf{r}) \bullet \nabla \times \iint_{S_{kl'}} \mathbf{S}_{kl',n'}(\mathbf{r}')g_{k}(d)ds'ds \\
{}_{\times}\mathbf{K}_{kll'}[n,n'] &= \iint_{S_{kl}} \mathbf{S}_{kl,n}(\mathbf{r}) \times \hat{\mathbf{n}}_{kl} \bullet \mathcal{K}_{k}(\mathbf{S}_{kl',n'},\mathbf{r})ds \\
&= \iint_{S_{kl}} \mathbf{S}_{kl,n}(\mathbf{r}) \times \hat{\mathbf{n}}_{kl} \bullet \nabla \times \iint_{S_{kl'}} \mathbf{S}_{kl',n'}(\mathbf{r}')g_{k}(d)ds'ds \\
\mathbf{L}_{kll'}[n,n'] &= \iint_{S_{kl}} \mathbf{S}_{kl,n}(\mathbf{r}) \bullet \mathcal{L}_{k}(\mathbf{S}_{kl',n'},\mathbf{r})ds \\
&= \gamma_{k} \iint_{S_{kl}} \iint_{S_{kl'}} \mathbf{S}_{kl,n}(\mathbf{r}) \bullet \mathbf{S}_{kl',n'}(\mathbf{r}')g_{k}(d)ds'ds \\
&\quad + \frac{1}{\gamma_{k}} \iint_{S_{kl}} \iint_{S_{kl'}} \nabla \bullet \mathbf{S}_{kl,n}(\mathbf{r}) \nabla' \bullet \mathbf{S}_{kl',n'}(\mathbf{r}')g_{k}(d)ds'ds \\
{}_{\times}\mathbf{L}_{kll'}[n,n'] &= \iint_{S_{kl}} \mathbf{S}_{kl,n}(\mathbf{r}) \times \hat{\mathbf{n}}_{kl} \bullet \mathcal{L}_{k}(\mathbf{S}_{kl',n'},\mathbf{r})ds \\
&= \gamma_{k} \iint_{S_{kl}} \iint_{S_{kl'}} \mathbf{S}_{kl,n}(\mathbf{r}) \times \hat{\mathbf{n}}_{kl} \bullet \mathbf{S}_{kl',n'}(\mathbf{r}')g_{k}(d)ds'ds \\
&\quad - \frac{1}{\gamma_{k}} \oint_{\partial S_{kl,n}} \hat{\mathbf{t}}_{kl,n} \bullet \mathbf{S}_{kl,n}(\mathbf{r}) \iint_{S_{kl'}} \nabla' \bullet \mathbf{S}_{kl',n'}(\mathbf{r}')g_{k}(d)ds'dl \\
\mathbf{T}_{kll'}[n,n'] &= \frac{1}{2} \iint_{S_{kl}} \mathbf{S}_{kl,n}(\mathbf{r}) \bullet \mathbf{S}_{kl',n'}(\mathbf{r}')ds \\
{}_{\times}\mathbf{T}_{kll'}[n,n'] &= \frac{1}{2} \iint_{S_{kl}} \mathbf{S}_{kl,n}(\mathbf{r}) \times \hat{\mathbf{n}}_{kl} \bullet \mathbf{S}_{kl',n'}(\mathbf{r}')ds
\end{aligned}
\tag{3.1.9}
$$

for $1 \leq n \leq N_{kl}$ and $1 \leq n' \leq N_{kl'}$. Here, $\partial S_{kl,n}$ is the contour bounding $\mathbf{S}_{kl,n}$ traversed such that the right-hand-rule yields the normal direction $\hat{\mathbf{n}}_{kl}$ (when the edge $e_{kl,n}$ is a regular edge, the integral should be separated to two and $e_{kl,n}$ must be traversed twice in opposite directions) and $\hat{\mathbf{t}}_{kl,n}$ is the tangential unit vector along the contour $\partial S_{kl,n}$.

The computational complexity of the above procedure should be contrasted to that of the MOM solution in Section 2.1.3.4: (i) Double the number of operations needed for assembling the ${}^{\mathrm{cc}}\mathbf{Z}$ matrix in (3.1.4) compared to that for the ${}^{\mathrm{EH}}\mathbf{Z}$ matrix in (2.1.12) because of the additional cost of filling the ${}_{\times}\mathbf{K}_{kll'}$ and ${}_{\times}\mathbf{L}_{kll'}$ matrices (the $\mathbf{T}_{kll'}$ and ${}_{\times}\mathbf{T}_{kll'}$ are near-diagonal matrices with non-zero entries only for overlapping basis/testing function pairs and require only $O(N)$ operations to fill); (ii) The same number of operations are needed per iteration for solving (3.1.4) as (2.1.12); and (iii) the same amount of memory is needed for solving (3.1.4) and (2.1.12). If an iterative solver that needs ${}^{\mathrm{cc}}N^{\mathrm{I}}$ iterations to converge is used then the setup, solution, and memory costs scale as $O(2N^{\mathrm{nz}})$, $O({}^{\mathrm{cc}}N^{\mathrm{I}}N^{\mathrm{nz}})$, and $O(N^{\mathrm{nz}})$, respectively.

3.1.3. Multiple-Grid AIM

Similar to the multiple-grid AIM in Section 2.1.4, computational savings are achieved by employing K different auxiliary grids $C_0,\ldots,C_{K-1}$ (identical to those defined in Section 2.1.4.1) for a K-region problem (Fig. 2.1.4). Using grid C_k, the proposed scheme approximates the MOM matrices pertinent to the equivalent problem k as ${}^{\mathrm{CC}}\mathbf{Z}_{kll'} \approx {}^{\mathrm{CC}}\mathbf{Z}_{kll'}^{\mathrm{near}} + {}^{\mathrm{CC}}\mathbf{Z}_{kll'}^{\mathrm{FFT}}$, where

$$\begin{aligned}
{}^{\mathrm{CC}}\mathbf{Z}_{kll'}^{\mathrm{FFT}} &= \left(\begin{bmatrix} \mathbf{\Lambda}_{kl}^{T} & \mathbf{0} \\ \mathbf{0} & \mathbf{\Lambda}_{kl}^{T} \end{bmatrix} \underbrace{\begin{bmatrix} \mathbf{L}_{k}^{\mathrm{FFT}} & \mathbf{K}_{k}^{\mathrm{FFT}} \big/ \eta_k \\ -\eta_k \mathbf{K}_{k}^{\mathrm{FFT}} & \mathbf{L}_{k}^{\mathrm{FFT}} \end{bmatrix}}_{\mathbf{Z}_{k}^{\mathrm{FFT}}} + \begin{bmatrix} \Gamma_{kl}^{T} & \mathbf{0} \\ \mathbf{0} & \Gamma_{kl}^{T} \end{bmatrix} \underbrace{\begin{bmatrix} -\mathbf{K}_{k}^{\mathrm{FFT}} & \mathbf{L}_{k}^{\mathrm{FFT}} \big/ \eta_k \\ -\eta_k \mathbf{L}_{k}^{\mathrm{FFT}} & -\mathbf{K}_{k}^{\mathrm{FFT}} \end{bmatrix}}_{{}_{\times}\mathbf{Z}_{k}^{\mathrm{FFT}}} \right) \begin{bmatrix} \mathbf{\Lambda}_{kl'} & \mathbf{0} \\ \mathbf{0} & \mathbf{\Lambda}_{kl'} \end{bmatrix} \\
{}^{\mathrm{CC}}\mathbf{Z}_{kll'}^{\mathrm{near}} &= \begin{bmatrix} \mathbf{L}_{kll'}^{\mathrm{near}} - {}_{\times}\mathbf{K}_{kll'}^{\mathrm{near}} + 2\mathbf{T}_{kll'} & \left({}_{\times}\mathbf{L}_{kll'}^{\mathrm{near}} + \mathbf{K}_{kll'}^{\mathrm{near}} + 2\,{}_{\times}\mathbf{T}_{kll'} \right) \big/ \eta_k \\ -\eta_k \left({}_{\times}\mathbf{L}_{kll'}^{\mathrm{near}} + \mathbf{K}_{kll'}^{\mathrm{near}} + 2\,{}_{\times}\mathbf{T}_{kll'} \right) & \mathbf{L}_{kll'}^{\mathrm{near}} - {}_{\times}\mathbf{K}_{kll'}^{\mathrm{near}} + 2\mathbf{T}_{kll'} \end{bmatrix}
\end{aligned} \tag{3.1.10}$$

Here, the projection matrix $\mathbf{\Lambda}_{kl'}$, the interpolation matrix $\mathbf{\Lambda}_{kl}^{T}$, and the propagation matrices $\mathbf{L}_{k}^{\mathrm{FFT}}$ and $\mathbf{K}_{k}^{\mathrm{FFT}}$ are identical to the ones given in (2.1.18) and (2.1.19). Just as in Section 2.1.4, 8 block-Toeplitz matrix-vector multiplications are calculated via FFTs to multiply $\mathbf{Z}_{k}^{\mathrm{FFT}}$ with a trial vector (once again, these correspond to the multiplications of $\mathbf{L}_{k}^{\mathrm{FFT}}$ with electric and magnetic current coefficients, respectively). The multiplication of

${}_{\times}\mathbf{Z}_k^{\text{FFT}}$ with a trial vector is found from that of $\mathbf{Z}_k^{\text{FFT}}$ with the same trial vector at no additional cost (the sub-matrices of the two matrices are identical and the scaling coefficients are absorbed into the interpolation stage). The extra interpolation matrix Γ_{kl} interpolates fields at observation points on C_k onto the rotated version of the testing functions on S_{kl}; it is given as

$$\Gamma_{kl} = \begin{bmatrix}\Gamma_{kl}^{\text{x}} & \Gamma_{kl}^{\text{y}} & \Gamma_{kl}^{\text{z}} & \Gamma_{kl}^{\text{L}}\end{bmatrix}^T \tag{3.1.11}$$

Here, each column n of the projection matrices $\Gamma_{kl}^{\text{x,y,z,L}}$ are filled by matching the multipole moments of the $M_{k,n}$ point sources on C_k to those of the functions $\hat{\mathbf{x}}\cdot\mathbf{S}_{kl,n}\times\hat{\mathbf{n}}_{kl},\ \hat{\mathbf{y}}\cdot\mathbf{S}_{kl,n}\times\hat{\mathbf{n}}_{kl},\ \hat{\mathbf{z}}\cdot\mathbf{S}_{kl,n}\times\hat{\mathbf{n}}_{kl},\ -\hat{\mathbf{t}}_{kl,n}\cdot\mathbf{S}_{kl,n}$, respectively.

For $1\le n\le N_{kl}$ and $1\le n'\le N_{kl'}$, the entries of the near-zone correction matrices ${}^{\text{CC}}\mathbf{Z}_{kl'}^{\text{near}}$ in (3.1.10) are

$$\mathbf{X}_{kl'}^{\text{near}}[n,n'] = \mathbf{X}_{kl'}[n,n'] - \mathbf{X}_{kl'}^{\text{FFT}}[n,n'] \tag{3.1.12}$$

($\mathbf{X}\in\{\mathbf{L},\mathbf{K},{}_{\times}\mathbf{L},{}_{\times}\mathbf{K}\}$) when the testing function $\mathbf{S}_{kl,n}$ ($\mathbf{S}_{kl,n}\times\hat{\mathbf{n}}_{kl}$) is in the near-zone of the basis function $\mathbf{S}_{kl',n'}$ or zero otherwise.

Assembling the ${}^{\text{CC}}\mathbf{Z}_{kl'}$ matrices as in (2.1.12)-(2.1.15), the method approximates the MOM matrix equation (3.1.4) as

$$\left({}^{\text{CC}}\mathbf{Z}^{\text{FFT}} + {}^{\text{CC}}\mathbf{Z}^{\text{near}}\right)\begin{bmatrix}\mathbf{I}\\ \mathbf{V}\end{bmatrix} \approx \begin{bmatrix}{}^{\text{CC}}\mathbf{V}^{\text{inc}}\\ {}^{\text{CC}}\mathbf{I}^{\text{inc}}\end{bmatrix} \tag{3.1.13}$$

where

$$\begin{aligned}{}^{\text{CC}}\mathbf{Z}^{\text{FFT}} = \sum_k\sum_l \beta_{kl}&\left(\begin{bmatrix}\mathbf{C}_{kl}^T\mathbf{\Lambda}_{kl}^T & \mathbf{0}\\ \mathbf{0} & \mathbf{C}_{kl}^T\mathbf{\Lambda}_{kl}^T\end{bmatrix}\mathbf{Z}_k^{\text{FFT}} + \begin{bmatrix}\mathbf{C}_{kl}^T\Gamma_{kl}^T & \mathbf{0}\\ \mathbf{0} & \mathbf{C}_{kl}^T\Gamma_{kl}^T\end{bmatrix}{}_{\times}\mathbf{Z}_k^{\text{FFT}}\right)\\ &\times\sum_{l'=0,l'\neq k}^{K-1}\alpha_{kl'}\begin{bmatrix}\mathbf{\Lambda}_{kl'}\mathbf{C}_{kl'} & \mathbf{0}\\ \mathbf{0} & \mathbf{\Lambda}_{kl'}\mathbf{C}_{kl'}\end{bmatrix}\end{aligned} \tag{3.1.14}$$

$${}^{\text{CC}}\mathbf{Z}^{\text{near}} = \sum_k\sum_l \beta_{kl}\begin{bmatrix}\mathbf{C}_{kl}^T & \mathbf{0}\\ \mathbf{0} & \mathbf{C}_{kl}^T\end{bmatrix}\sum_{l'=0,l'\neq k}^{K-1}{}^{\text{CC}}\mathbf{Z}_{kl'}^{\text{near}}\alpha_{kl'}\begin{bmatrix}\mathbf{C}_{kl'} & \mathbf{0}\\ \mathbf{0} & \mathbf{C}_{kl'}\end{bmatrix} \tag{3.1.15}$$

The multiple-grid AIM stores the correction matrix ${}^{\text{cc}}\mathbf{Z}^{\text{near}}$, the sparse matrices $\mathbf{\Lambda}_{kl}$, $\mathbf{C}_{kl}$ and Γ_{kl}, and unique parts of the block-Toeplitz matrices $\mathbf{Z}_{k}^{\text{FFT}}$ and ${}_{\times}\mathbf{Z}_{k}^{\text{FFT}}$ in (3.1.10). Compared to the multiple-grid AIM in Chapter 2, only the pre-correction and interpolation stages are modified while the projection and propagation stages are unchanged (no additional FFTs are needed); the pre-correction stage requires double the matrix fill time (but the same storage space and the same number of operations per iteration); and the interpolation stage requires double the number of operations and memory. Thus, the setup, solution, and memory costs of the multiple-grid AIM scale as $O(2N^{\text{nz,near}}+\sum_{k}N_{k}^{\text{C}})$, $O({}^{\text{cc}}N^{\text{I}}[N^{\text{nz,near}}+\sum_{k}N_{k}^{\text{C}}\log N_{k}^{\text{C}}])$, and $O(N^{\text{nz,near}}+\sum_{k}N_{k}^{\text{C}})$, respectively.

3.1.4. Numerical Results

This section presents numerical results that validate the performance of the classical and multiple-grid AIM accelerated MOM solution of the CC-PMCHWT equations.

3.1.4.1. Computational Complexity Validation

Here, the practical efficiency and accuracy of the multiple-grid AIM scheme for piecewise homogeneous structures are systematically evaluated as the number of edges N increases. The size of multi-region problems can be scaled in the same ways as Section 2.1.5: On the one extreme, new regions are added recursively for layered spheres as the number of layers are increased; on the other extreme, they are added in parallel for a dielectric-rod array as the number of rods are increased. All geometry, material, and AIM parameters are chosen the same in the following simulations as those in Section 2.1.5.1; these parameters can be found in Tables 2.1.1 and 2.1.2.

3.1.4.2. Layered Sphere

Consider the $K-1$ layered spheres with $r_0 = \lambda_0$ and $r_0 = 4\lambda_0$ in Section 2.1.5.1 (shown in Fig. 2.1.5). For the $r_0 = \lambda_0$ layered spheres, Figs. 3.1.1(a)-(d) compare the setup, solution, and memory costs for the CC-PMCHWT and the EH-PMCHWT formulations. The computational costs in Fig. 3.1.1 agree well with theoretical analysis, e.g., CC-PMCHWT formulation doubles all setup costs; the time required per iteration by the classic MOM solution is identical for both formulations, whereas multiple-grid AIM solution requires some more operations (~10%) for the CC-PMCHWT formulation due to the extra interpolation step; the memory cost of the classical MOM solution is identical for both two formulations, whereas multiple-grid AIM solution requires some more memory (~12%) for the CC-PMCHWT formulation due to the extra interpolation coefficients. For the $r_0 = 4\lambda_0$ layered spheres, Figs. 3.1.2(a)-(d) show the setup, solution, and memory costs. Again, the computational costs agree with theoretical analysis: CC-PMCHWT formulation doubles the setup costs while slightly increasing the time required per iteration and the memory. Figs. 3.1.1(d) and 3.1.2(d) show the number of iterations required for convergence by each method when using diagonal preconditioning. The figure shows that the iterative solver convergence deteriorates with the increasing number of layers for both formulations; however, the convergence for CC-PMCHWT formulation generally requires much fewer iterations.

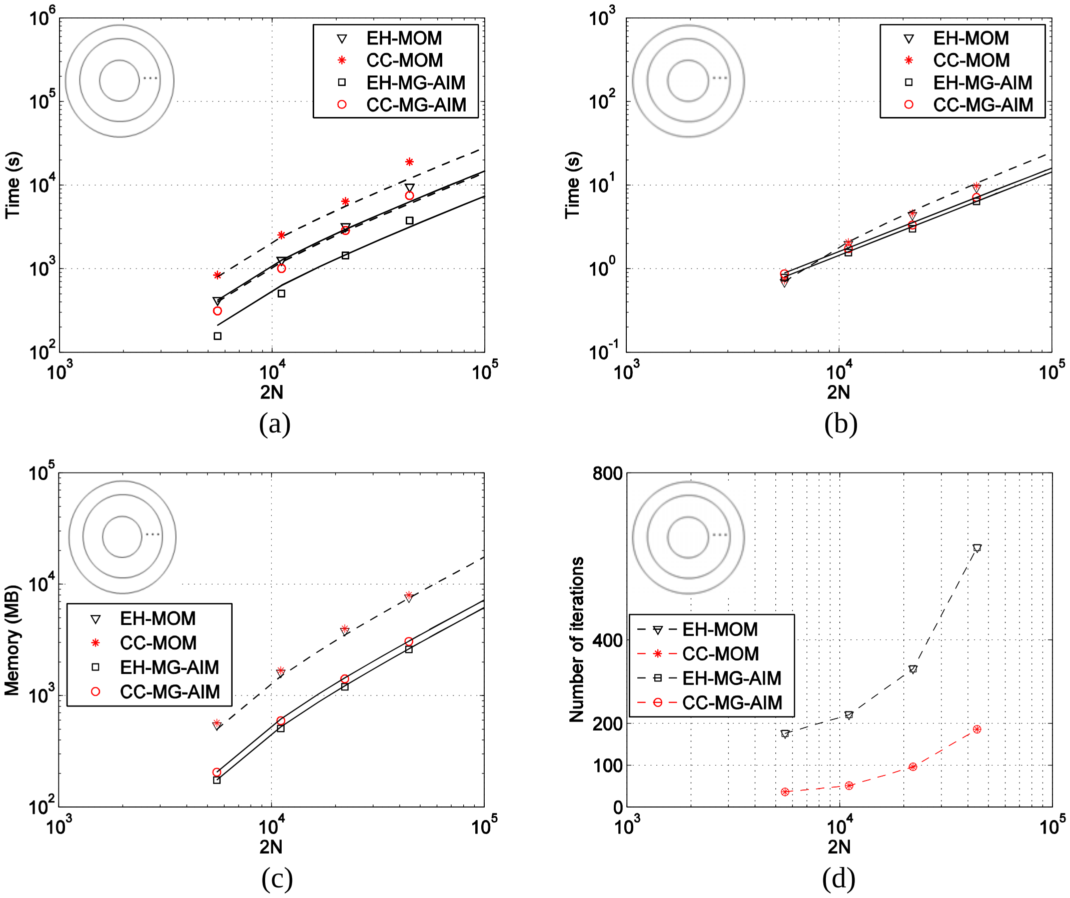

(a) (b) (c) (d)

Figure 3.1.1: CC-PMCHWT solvers vs. EH-PMCHWT solvers for the $r_0 = \lambda_0$ layered dielectric sphere as the number of layers is increased from 1 to 8. (a) The setup cost. (b) The solution cost per iteration. (c) The memory cost. (d) The number of iterations. In (a)-(c), all dashed and straight lines are parallel to $2K-3$ except the straight lines in (c) that are parallel to $K-1$. In (a), the higher solid and dash lines are drawn by doubling the slope of the corresponding lines.

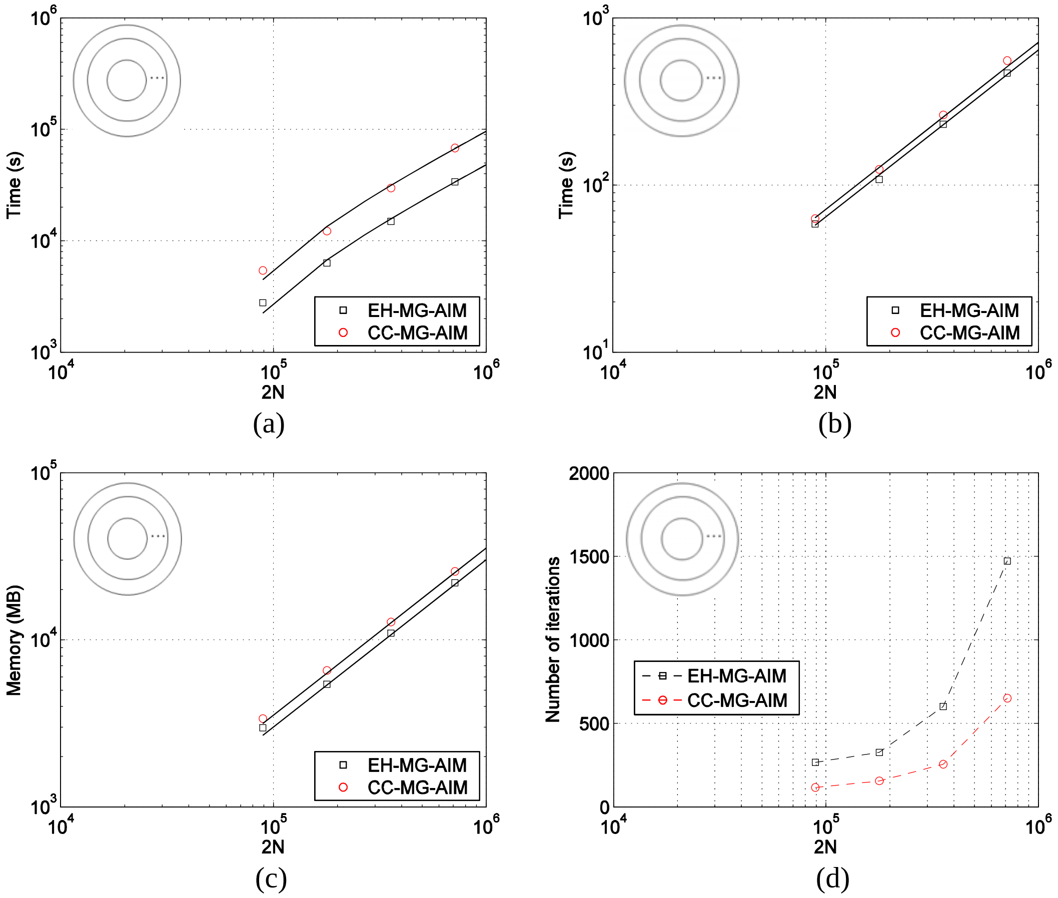

(a) (b)

(c) (d)

Figure 3.1.2: CCPMCHWT solvers vs. EH-PMCHWT solvers for the $r_0 = 4\lambda_0$ layered dielectric sphere as the number of layers is increased from 1 to 8 layers. (a) The setup cost. (b) The solution cost per iteration. (c) The memory cost. (d) The number of iterations. In (a)-(b), all straight lines are parallel to $2K-3$; in (c), all of them are parallel to $K-1$. In (a), the higher dash lines are drawn by doubling the slope of the corresponding lines.

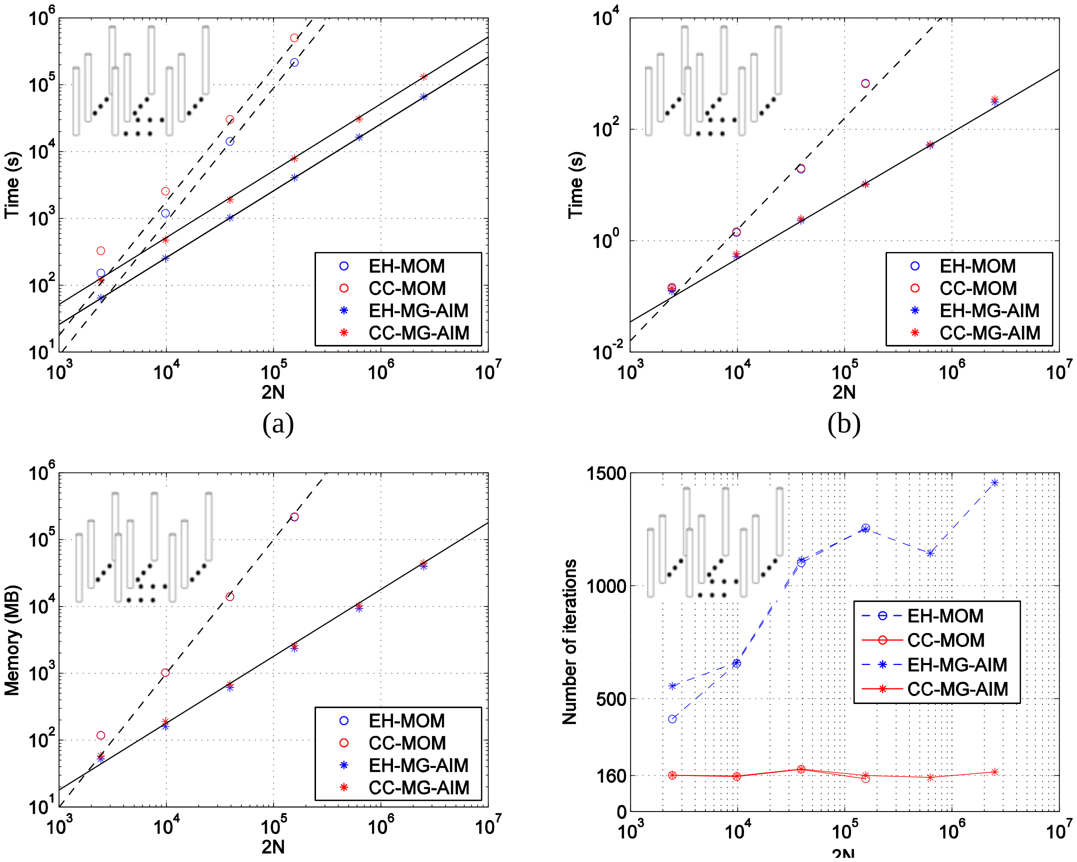

(a) (b)

(c) (d)

Figure 3.1.3: CC-PMCHWT solvers vs. EH-PMCHWT solvers for the dielectric rod array as the number of rods is increased from 1 to 1024. (a) The setup cost. (b) The solution cost per iteration. (c) The memory cost. (d) The number of iterations. In (a)-(c), dashed lines are parallel to K^2 and straight lines are parallel to K. In (a), the higher solid and dash lines are drawn by doubling the slope of the corresponding lines.

3.1.4.3. Dielectric-Rod Array

Consider the uniform two-dimensional array of $K-1$ dielectric rods in Section 2.1.5.2 (shown in Fig. 2.1.6. Figs. 3.1.3(a)-(c) compare the setup, solution, and memory costs of the classical and fast solvers for the CC-PMCHWT and the EH-PMCHWT formulations. The computational costs in Figs. 3.1.3 agree with these theoretical analyses, e.g., the CC-PMCHWT formulation doubles all setup costs; the time required per iteration by each solver is practically the same for both formulations; the memory cost of the classical MOM solution is identical for both formulations, whereas multiple-grid AIM solution requires slightly more memory for CC-PMCHWT due to the extra interpolation coefficients. Fig. 3.1.3(d) shows the number of iterations required for convergence by each method when using diagonal preconditioning. The figure shows that the iterative solver convergence deteriorates with the number of rods for the EH-PMCHWT formulation, while it is insensitive to the problem size for the CC-PMCHWT formulation.

3.1.5. Summary

This section formulated the CC-PMCHWT equations for piecewise homogeneous structures and highlighted the necessary changes to the classical as well as multiple-grid AIM accelerated MOM solution. The iterative solution of CC-PMCHWT equations generally converge better than EH-PMCHWT ones; however, the improvement is problem dependent (further examples are shown in Sections 3.2-3.4 and Chapter 4). Also, the accuracy of CC-PMCHWT-based solvers might be degraded by the high-order singularity present in the integrations of rotated integral equations, which can be improved by increasing the mesh density or by using curl-conforming testing functions. The CC-PMCHWT formulation and multiple-grid AIM acceleration are general enough that they can be easily extended to structures containing PEC and/or metamaterial regions with negative constitutive parameters as detailed in the next sections.

3.2. MODELING A PEC/PMC PLANE

To model a PEC/PMC plane efficiently, the Green function modification (GFM) approach of Section 2.2 should be extended to CC-PMCHWT. These extensions are slightly more complicated than those for the EH-PMCHWT formulation because of the presence of additional rotated EFIE and MFIE kernels.

Consider the same homogeneous structure with surface S residing above a PEC plane at $z = 0$ excited by an external time-harmonic electromagnetic field $\{\mathbf{E}_0^{\mathrm{inc}}, \mathbf{H}_0^{\mathrm{inc}}\}$ (Fig. 2.2.1). The brute-force imaging approach of the CC-PMCHWT is the same the EH-PMCHWT formulation: (i) Apply method of images: Remove the plane; introduce the image structure with surface $\tilde{S}$; and excite the new structure with the sum of $\{\mathbf{E}_0^{\mathrm{inc}}, \mathbf{H}_0^{\mathrm{inc}}\}$ and its image $\{\tilde{\mathbf{E}}_0^{\mathrm{inc}}, \tilde{\mathbf{H}}_0^{\mathrm{inc}}\}$. (ii) Formulate integral equations: Construct equivalent problems (Fig. 2.2.1); formulate JCFIEs and MCFIEs for each problem; and combine them using the PMCHWT recipe. (iii) Apply the MOM procedure with RWG basis functions and Galerkin testing: Mesh S with triangle patches with N edges and $\tilde{S}$ with the images of these patches; and expand the actual (image) electric and magnetic current densities $\{\mathbf{J}, \mathbf{M}\}$ ($\{\tilde{\mathbf{J}}, \tilde{\mathbf{M}}\}$) on S ($\tilde{S}$) by using actual (image) RWG functions. Then, Galerkin testing yields the brute-force imaging (BFI) equations

$$\sum_{k=0}^{2}\begin{bmatrix} (\mathbf{L}_k - {}_{\times}\mathbf{K}_k + 2\mathbf{T}_k) & ({}_{\times}\mathbf{L}_k + \mathbf{K}_k + 2\,{}_{\times}\mathbf{T}_k)\big/\eta_k \\ -\eta_k({}_{\times}\mathbf{L}_k + \mathbf{K}_k + 2\,{}_{\times}\mathbf{T}_k) & (\mathbf{L}_k - {}_{\times}\mathbf{K}_k + 2\mathbf{T}_k) \end{bmatrix}\begin{bmatrix} \mathbf{I} \\ \tilde{\mathbf{I}} \\ \mathbf{V} \\ \tilde{\mathbf{V}} \end{bmatrix} = \begin{bmatrix} {}^{\mathrm{CC}}\mathbf{V}_0^{\text{a-inc}} \\ {}^{\mathrm{CC}}\mathbf{V}_0^{\text{i-inc}} \\ {}^{\mathrm{CC}}\mathbf{I}_0^{\text{a-inc}} \\ {}^{\mathrm{CC}}\mathbf{I}_0^{\text{i-inc}} \end{bmatrix} \quad (\mathrm{BFI}) \qquad (3.2.1)$$

Here and throughout this section, the subscript of a matrix or vector shows the equivalent problem (0 for external-, 1 for actual internal-, and 2 for image internal-equivalent) and the superscript above a vector shows the testing function (“a-inc” for actual and “i-inc” for image RWG) used to fill it. The entries of the right-hand-side vectors are (for $1 \le n \le N$)

$$\begin{aligned}
{}^{\mathrm{CC}}\mathbf{V}_0^{\text{a-inc}}[n] &= \iint \mathbf{S}_n^{\mathrm{a}} \bullet \left[\left(\mathbf{E}_0^{\mathrm{inc}} + \tilde{\mathbf{E}}_0^{\mathrm{inc}}\right) \big/ \eta_0 + \hat{\mathbf{n}}_0^{\mathrm{a}} \times \left(\mathbf{H}_0^{\mathrm{inc}} + \tilde{\mathbf{H}}_0^{\mathrm{inc}}\right) \right] ds \\
{}^{\mathrm{CC}}\mathbf{V}_0^{\text{i-inc}}[n] &= \iint \mathbf{S}_n^{\mathrm{i}} \bullet \left[\left(\mathbf{E}_0^{\mathrm{inc}} + \tilde{\mathbf{E}}_0^{\mathrm{inc}}\right) \big/ \eta_0 + \hat{\mathbf{n}}_0^{\mathrm{i}} \times \left(\mathbf{H}_0^{\mathrm{inc}} + \tilde{\mathbf{H}}_0^{\mathrm{inc}}\right) \right] ds \\
{}^{\mathrm{CC}}\mathbf{I}_0^{\text{a-inc}}[n] &= \iint \mathbf{S}_n^{\mathrm{a}} \bullet \left[\eta_0 \left(\mathbf{H}_0^{\mathrm{inc}} + \tilde{\mathbf{H}}_0^{\mathrm{inc}}\right) - \hat{\mathbf{n}}_0^{\mathrm{a}} \times \left(\mathbf{E}_0^{\mathrm{inc}} + \tilde{\mathbf{E}}_0^{\mathrm{inc}}\right) \right] ds \\
{}^{\mathrm{CC}}\mathbf{I}_0^{\text{i-inc}}[n] &= \iint \mathbf{S}_n^{\mathrm{i}} \bullet \left[\eta_0 \left(\mathbf{H}_0^{\mathrm{inc}} + \tilde{\mathbf{H}}_0^{\mathrm{inc}}\right) - \hat{\mathbf{n}}_0^{\mathrm{i}} \times \left(\mathbf{E}_0^{\mathrm{inc}} + \tilde{\mathbf{E}}_0^{\mathrm{inc}}\right) \right] ds
\end{aligned} \tag{3.2.2}$$

where $\hat{\mathbf{n}}_0^{\mathrm{a}}$ ($\hat{\mathbf{n}}_0^{\mathrm{i}}$) represents the normal on the actual (image) structure for the external problem, similar definitions are used for the rest equivalent problems. $\mathbf{X}_k \in \{\mathbf{L}_k, \mathbf{K}_k\}$ and ${}_{\times}\mathbf{X}_k \in \{{}_{\times}\mathbf{L}_k, {}_{\times}\mathbf{K}_k\}$, then the entries of these $2N \times 2N$ matrices can be found by expressing them as

$$\mathbf{X}_k = \begin{bmatrix} \mathbf{X}_k^{\mathrm{aa}} & \mathbf{X}_k^{\mathrm{ai}} \\ \mathbf{X}_k^{\mathrm{ia}} & \mathbf{X}_k^{\mathrm{ii}} \end{bmatrix}, \; {}_{\times}\mathbf{X}_k = \begin{bmatrix} {}_{\times}\mathbf{X}_k^{\mathrm{aa}} & {}_{\times}\mathbf{X}_k^{\mathrm{ai}} \\ {}_{\times}\mathbf{X}_k^{\mathrm{ia}} & {}_{\times}\mathbf{X}_k^{\mathrm{ii}} \end{bmatrix} \tag{3.2.3}$$

It is important to note that some of these $N \times N$ sub-matrices can be zero (e.g., $\mathbf{X}_1^{\mathrm{ai,ia,ii}} = \mathbf{X}_2^{\mathrm{aa,ai,ia}} = \mathbf{0}$ and ${}_{\times}\mathbf{X}_1^{\mathrm{ai,ia,ii}} = {}_{\times}\mathbf{X}_2^{\mathrm{aa,ai,ia}} = \mathbf{0}$ when the structure does not intersect the PEC plane); otherwise, their entries are

$$\begin{aligned}
\mathbf{L}_k^{\mathrm{ts}}[n,n'] &= \gamma_k \iint \mathbf{S}_n^{\mathrm{t}}(\mathbf{r}) \bullet \iint \mathbf{S}_{n'}^{\mathrm{s}}(\mathbf{r}') g_k(\mathbf{r},\mathbf{r}') ds' ds \\
&\quad + \frac{1}{\gamma_k} \iint \nabla \bullet \mathbf{S}_n^{\mathrm{t}}(\mathbf{r}) \iint \nabla' \bullet \mathbf{S}_{n'}^{\mathrm{s}}(\mathbf{r}') g_k(\mathbf{r},\mathbf{r}') ds' ds \\
{}_{\times}\mathbf{L}_k^{\mathrm{ts}}[n,n'] &= \gamma_k \iint \mathbf{S}_n^{\mathrm{t}}(\mathbf{r}) \times \hat{\mathbf{n}}_k^{\mathrm{t}} \bullet \iint \mathbf{S}_{n'}^{\mathrm{s}}(\mathbf{r}') g_k(d) ds' ds \\
&\quad - \frac{1}{\gamma_k} \oint \hat{\mathbf{t}}_n^{\mathrm{t}} \bullet \mathbf{S}_n^{\mathrm{t}}(\mathbf{r}) \iint \nabla' \bullet \mathbf{S}_{n'}^{\mathrm{s}}(\mathbf{r}') g_k(d) ds' dl \\
\mathbf{K}_k^{\mathrm{ts}}[n,n'] &= \iint \mathbf{S}_n^{\mathrm{t}}(\mathbf{r}) \bullet \nabla \times \iint \mathbf{S}_{n'}^{\mathrm{s}}(\mathbf{r}') g_k(\mathbf{r},\mathbf{r}') ds' ds \\
{}_{\times}\mathbf{K}_k^{\mathrm{ts}}[n,n'] &= \iint \mathbf{S}_n^{\mathrm{t}}(\mathbf{r}) \times \hat{\mathbf{n}}_k^{\mathrm{t}} \bullet \nabla \times \iint \mathbf{S}_{n'}^{\mathrm{s}}(\mathbf{r}') g_k(\mathbf{r},\mathbf{r}') ds' ds \\
\mathbf{T}_k^{\mathrm{ts}}[n,n'] &= \frac{1}{2} \iint \mathbf{S}_n^{\mathrm{t}}(\mathbf{r}) \bullet \mathbf{S}_{n'}^{\mathrm{s}}(\mathbf{r}') ds \\
{}_{\times}\mathbf{T}_k^{\mathrm{ts}}[n,n'] &= \frac{1}{2} \iint \mathbf{S}_n^{\mathrm{t}}(\mathbf{r}) \times \hat{\mathbf{n}}_k^{\mathrm{t}} \bullet \mathbf{S}_{n'}^{\mathrm{s}}(\mathbf{r}') ds
\end{aligned} \tag{3.2.4}$$

for $1 \le n, n' \le N$ and $\mathrm{t,s} \in \{\mathrm{a,i}\}$. Note that the self-term calculations $\mathbf{T}_k^{\mathrm{ai}}[n,n'] = \mathbf{T}_k^{\mathrm{ia}}[n,n'] = {}_{\times}\mathbf{T}_k^{\mathrm{ai}}[n,n'] = {}_{\times}\mathbf{T}_k^{\mathrm{ia}}[n,n'] = 0$. In the above equations, $g_k(\mathbf{r},\mathbf{r}')$ is the homogeneous-medium Green function and ε_k, μ_k, γ_k, and η_k are the permittivity, permeability, propagation constant, and intrinsic impedance for free space ($k = 0$) or dielectric structure ($k = 1, 2$), respectively. The MOM matrix equation (3.2.1) can be simplified by enforcing that the image and actual electric (magnetic) currents have opposite (identical) tangential components and identical (opposite) vertical components, i.e.,

$$\begin{aligned} \hat{\mathbf{t}} \bullet \{\mathbf{J}(\mathbf{r}), \mathbf{M}(\mathbf{r})\} &= \hat{\mathbf{t}} \bullet \{-\tilde{\mathbf{J}}(\tilde{\mathbf{r}}), \tilde{\mathbf{M}}(\tilde{\mathbf{r}})\} \\ \hat{\mathbf{z}} \bullet \{\mathbf{J}(\mathbf{r}), \mathbf{M}(\mathbf{r})\} &= \hat{\mathbf{z}} \bullet \{\tilde{\mathbf{J}}(\tilde{\mathbf{r}}), -\tilde{\mathbf{M}}(\tilde{\mathbf{r}})\} \end{aligned} \tag{3.2.5}$$

From Section 2.2, it is clear that

$$\{\tilde{\mathbf{I}}, \tilde{\mathbf{V}}\} = \{-\mathbf{I}, \mathbf{V}\} \tag{3.2.6}$$

Substituting (3.2.6) in (3.2.1), two sets of equations are obtained for $\mathbf{I}$ and $\mathbf{V}$: One using actual and the other using image testing functions. Either set or their linear combination can be solved uniquely for $\mathbf{I}$, $\tilde{\mathbf{I}}$, $\mathbf{V}$ and $\tilde{\mathbf{V}}$; here, the first set is chosen:

$$\begin{gathered} \sum_{k=0}^{1} \begin{bmatrix} \mathbf{LxK} & \mathbf{KxL}/\eta_k \\ -\eta_k \mathbf{KxL} & \mathbf{LxK} \end{bmatrix} \begin{bmatrix} \mathbf{I} \\ \mathbf{V} \end{bmatrix} = \begin{bmatrix} {}^{\mathrm{CC}}\mathbf{V}_0^{\text{a-inc}} \\ {}^{\mathrm{CC}}\mathbf{I}_0^{\text{a-inc}} \end{bmatrix} \ (\mathrm{GFM}) \\ \mathbf{LxK} = (\mathbf{L}_k^{\mathrm{aa}} - \mathbf{L}_k^{\mathrm{ai}}) - ({}_{\times}\mathbf{K}_k^{\mathrm{aa}} - {}_{\times}\mathbf{K}_k^{\mathrm{ai}}) \\ \mathbf{KxL} = ({}_{\times}\mathbf{L}_k^{\mathrm{aa}} + {}_{\times}\mathbf{L}_k^{\mathrm{ai}}) + (\mathbf{K}_k^{\mathrm{aa}} + \mathbf{K}_k^{\mathrm{ai}}) \end{gathered} \tag{3.2.7}$$

3.2.1. MOM Computational Complexity and Extensions

There are 24 unique matrices ($\mathbf{X}_0^{\mathrm{aa,ai,ia,ii}}$, $\mathbf{X}_1^{\mathrm{aa}}$, $\mathbf{X}_2^{\mathrm{ii}}$, ${}_{\times}\mathbf{X}_0^{\mathrm{aa,ai,ia,ii}}$, ${}_{\times}\mathbf{X}_1^{\mathrm{aa}}$, and ${}_{\times}\mathbf{X}_2^{\mathrm{ii}}$) in (3.2.1) and 12 unique matrices ($\mathbf{X}_0^{\mathrm{aa,ai}}$, $\mathbf{X}_1^{\mathrm{aa}}$, ${}_{\times}\mathbf{X}_0^{\mathrm{aa,ai}}$, and ${}_{\times}\mathbf{X}_1^{\mathrm{aa}}$) in (3.2.7) that are dense ($\mathbf{T}_k^{\mathrm{aa}}$, $\mathbf{T}_k^{\mathrm{ai}}$, ${}_{\times}\mathbf{T}_k^{\mathrm{aa}}$, and ${}_{\times}\mathbf{T}_k^{\mathrm{ai}}$ are sparse). BFI and GFM approaches solve for $2N$ and N unknowns and require $O(24N^2)$ and $O(12N^2)$ bytes/operations to fill the unique matrices and $O(48N^2)$ and $O(24N^2)$ operations per iteration to calculate non-zero matrix-vector multiplications, respectively. Thus, GFM finds half the number of unknowns and requires half the memory space, matrix-fill operations, and matrix-solve operations compared to BFI.

When the PEC plane intersects the homogeneous structure, there are 2 equivalent problems, 32 unique matrices ($\mathbf{X}_{0,1}^{\mathrm{aa,ai,ia,ii}}$) in (3.2.1), and 16 unique matrices ($\mathbf{X}_{0,1}^{\mathrm{aa,ai}}$) in (3.2.7) are dense ($\mathbf{T}_k^{\mathrm{aa}}$, $\mathbf{T}_k^{\mathrm{ai}}$, ${}_\times\mathbf{T}_k^{\mathrm{aa}}$, and ${}_\times\mathbf{T}_k^{\mathrm{ai}}$ are sparse). Moreover, junction edges are treated the same way as the EH-PMCHWT formulation; because $N^{\mathrm{j}} \ll N^{\mathrm{r}}$ in general, they require $O(32N^2)$ and $O(16N^2)$ bytes/ operations to fill the unique matrices and $O(64N^2)$ and $O(32N^2)$ operations per iteration, respectively. Thus, GFM still solves for (almost) half the number of unknowns and requires (almost) half the resources compared to BFI.

When the structure is on/above a PMC plane, $\{\tilde{\mathbf{E}}_0^{\mathrm{inc}}, \tilde{\mathbf{H}}_0^{\mathrm{inc}}\}$ in (3.2.2) and the signs of the $\mathbf{X}^{\mathrm{ai}}$ terms in (3.2.7) must be modified according to duality (i.e., $\{\tilde{\mathbf{I}}, \tilde{\mathbf{V}}\} = \{\mathbf{I}, -\mathbf{V}\}$ for a PMC plane).

3.2.2. Green Function Modification for Multiple-Grid AIM

As the EH-PMCHWT formulation, when brute-force imaging is used, the multiple-grid AIM defines the same three auxiliary grids $C_{0,1,2}$ with $N_{0,1,2}^{\mathrm{C}}$ grid points that enclose $S_0 = S \cup \tilde{S}$, $S_1 = S$, and $S_2 = \tilde{S}$ to speed up the calculations stemming from the external-, actual internal-, and image internal-equivalent problem, respectively (Fig. 3.2.1). Using the same auxiliary grids, the multiple-grid AIM approximates the CC-PMCHWT MOM matrices in (3.2.1) as (for $0 \le k \le 2$)

$$\begin{aligned} \mathbf{X}_k &\approx \mathbf{X}_k^{\mathrm{near}} + \mathbf{\Lambda}_k^{\dagger}\mathbf{X}_k^{\mathrm{FFT}}\mathbf{\Lambda}_k \\ {}_\times\mathbf{X}_k &\approx {}_\times\mathbf{X}_k^{\mathrm{near}} + \Gamma_k^{\dagger}\mathbf{X}_k^{\mathrm{FFT}}\mathbf{\Lambda}_k \end{aligned} \tag{3.2.8}$$

where $\mathbf{\Lambda}_k$ are projection matrices that map the currents on S_k to point sources on C_k, $\mathbf{X}_k^{\mathrm{FFT}} \in \{\mathbf{L}_k^{\mathrm{FFT}}, \mathbf{K}_k^{\mathrm{FFT}}\}$ are propagation matrices that relate fields at observation points on C_k to point sources on C_k, $\mathbf{X}_k^{\mathrm{near}} \in \{\mathbf{L}_k^{\mathrm{near}}, \mathbf{K}_k^{\mathrm{near}}, \mathbf{T}_k^{\mathrm{near}}\}$ and ${}_\times\mathbf{X}_k^{\mathrm{near}} \in \{{}_\times\mathbf{L}_k^{\mathrm{near}}, {}_\times\mathbf{K}_k^{\mathrm{near}}, {}_\times\mathbf{T}_k^{\mathrm{near}}\}$ are correction matrices that adjust near-zone entries, and $\dagger$ denotes transpose. The projection matrices are expressed as

$$\boldsymbol{\Lambda}_k = \begin{bmatrix}\boldsymbol{\Lambda}_k^{\rm a} & \boldsymbol{\Lambda}_k^{\rm i}\end{bmatrix} = \begin{bmatrix}\boldsymbol{\Lambda}_k^{\rm a,x} & \boldsymbol{\Lambda}_k^{\rm i,x} \\ \boldsymbol{\Lambda}_k^{\rm a,y} & \boldsymbol{\Lambda}_k^{\rm i,y} \\ \boldsymbol{\Lambda}_k^{\rm a,z} & \boldsymbol{\Lambda}_k^{\rm i,z} \\ \boldsymbol{\Lambda}_k^{\rm a,\nabla} & \boldsymbol{\Lambda}_k^{\rm i,\nabla}\end{bmatrix} \quad \Gamma_k = \begin{bmatrix}\Gamma_k^{\rm a} & \Gamma_k^{\rm i}\end{bmatrix} = \begin{bmatrix}\Gamma_k^{\rm a,x} & \Gamma_k^{\rm i,x} \\ \Gamma_k^{\rm a,y} & \Gamma_k^{\rm i,y} \\ \Gamma_k^{\rm a,z} & \Gamma_k^{\rm i,z} \\ \Gamma_k^{\rm a,\nabla} & \Gamma_k^{\rm i,\nabla}\end{bmatrix} \tag{3.2.9}$$

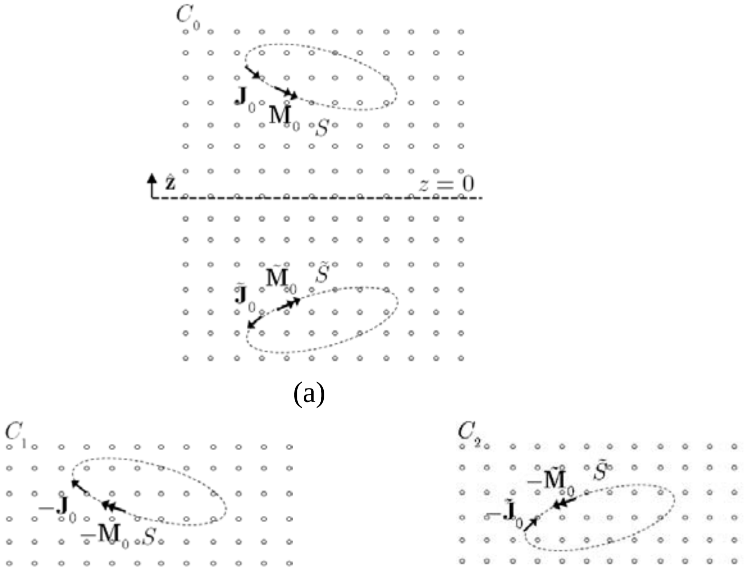

(a)

(b) (c)

Figure 3.2.1: The three multiple-grid AIM auxiliary grids used for brute-force imaging: (a) C_0, (b) C_1, and (c) C_2.

where the $4N_k^{\rm C} \times N$ projection matrices $\boldsymbol{\Lambda}_k^{\rm a}$, $\boldsymbol{\Lambda}_k^{\rm i}$, $\Gamma_k^{\rm a}$, and $\Gamma_k^{\rm i}$ are sparse with $O(N)$ non-zero entries ($\boldsymbol{\Lambda}_1^{\rm i} = \boldsymbol{\Lambda}_2^{\rm a} = \mathbf{0}$ and $\Gamma_1^{\rm i} = \Gamma_2^{\rm a} = \mathbf{0}$ when the PEC plane does not intersect the structure). The $4N_k^{\rm C} \times 4N_k^{\rm C}$ propagation matrices are constructed the same as (2.2.37). In (3.2.8), the $2N \times 2N$ correction matrices $\mathbf{X}_k^{\rm near}$ and ${}_{\times}\mathbf{X}_k^{\rm near}$ are sparse with $N_k^{\rm nz,near}$ entries and can be formulated as

$$\mathbf{X}_k^{\rm near} = \begin{bmatrix}\mathbf{X}_k^{\rm near,aa} & \mathbf{X}_k^{\rm near,ai} \\ \mathbf{X}_k^{\rm near,ia} & \mathbf{X}_k^{\rm near,ii}\end{bmatrix}, \; {}_{\times}\mathbf{X}_k^{\rm near} = \begin{bmatrix}{}_{\times}\mathbf{X}_k^{\rm near,aa} & {}_{\times}\mathbf{X}_k^{\rm near,ai} \\ {}_{\times}\mathbf{X}_k^{\rm near,ia} & {}_{\times}\mathbf{X}_k^{\rm near,ii}\end{bmatrix} \tag{3.2.10}$$

Some of these sub-matrices are zero similar to (3.2.3); the entries of the non-zero sub-matrices are

$$
\begin{aligned}
\mathbf{X}_k^{\mathrm{near,ts}}[n,n'] &= \begin{cases} (\mathbf{X}_k^{\mathrm{ts}} - \mathbf{\Lambda}_k^{\mathrm{t}\dagger}\mathbf{X}_k^{\mathrm{FFT}}\mathbf{\Lambda}_k^{\mathrm{s}})[n,n'] & \text{if } \mathbf{S}_n^{\mathrm{t}} \text{ near } \mathbf{S}_{n'}^{\mathrm{s}} \\ 0 & \text{otherwise} \end{cases} \\
{}_{\times}\mathbf{X}_k^{\mathrm{near,ts}}[n,n'] &= \begin{cases} ({}_{\times}\mathbf{X}_k^{\mathrm{ts}} - \Gamma_k^{\mathrm{t}\dagger}\mathbf{X}_k^{\mathrm{FFT}}\mathbf{\Lambda}_k^{\mathrm{s}})[n,n'] & \text{if } \mathbf{S}_n^{\mathrm{t}} \text{ near } \mathbf{S}_{n'}^{\mathrm{s}} \\ 0 & \text{otherwise} \end{cases}
\end{aligned}
\tag{3.2.11}
$$

for $1 \le n, n' \le N$ and $\mathrm{t},\mathrm{s} \in \{\mathrm{a},\mathrm{i}\}$.

When Green-function modification is used, the multiple-grid AIM must approximate the $\mathbf{X}_k^{\mathrm{aa}}$, ${}_{\times}\mathbf{X}_k^{\mathrm{aa}}$, $\mathbf{X}_k^{\mathrm{ai}}$, and ${}_{\times}\mathbf{X}_k^{\mathrm{ai}}$ matrices (when they exist) in (3.2.7). A simple approach is to use the same auxiliary grids as in the brute-force imaging approach but map only the actual currents for $\mathbf{X}_k^{\mathrm{aa}}$ (${}_{\times}\mathbf{X}_k^{\mathrm{aa}}$) and image currents for $\mathbf{X}_k^{\mathrm{ai}}$ (${}_{\times}\mathbf{X}_k^{\mathrm{ai}}$) (for $0 \le k \le 1$):

$$
\begin{aligned}
\mathbf{X}_k^{\mathrm{aa}} &\approx \mathbf{X}_k^{\mathrm{near,aa}} + \mathbf{\Lambda}_k^{\mathrm{a}\dagger}\mathbf{X}_k^{\mathrm{FFT}}\mathbf{\Lambda}_k^{\mathrm{a}} \\
\mathbf{X}_k^{\mathrm{ai}} &\approx \mathbf{X}_k^{\mathrm{near,ai}} + \mathbf{\Lambda}_k^{\mathrm{a}\dagger}\mathbf{X}_k^{\mathrm{FFT}}\mathbf{\Lambda}_k^{\mathrm{i}} \\
{}_{\times}\mathbf{X}_k^{\mathrm{aa}} &\approx {}_{\times}\mathbf{X}_k^{\mathrm{near,aa}} + \Gamma_k^{\mathrm{a}\dagger}\mathbf{X}_k^{\mathrm{FFT}}\mathbf{\Lambda}_k^{\mathrm{a}} \\
{}_{\times}\mathbf{X}_k^{\mathrm{ai}} &\approx {}_{\times}\mathbf{X}_k^{\mathrm{near,ai}} + \Gamma_k^{\mathrm{a}\dagger}\mathbf{X}_k^{\mathrm{FFT}}\mathbf{\Lambda}_k^{\mathrm{i}}
\end{aligned}
\tag{3.2.12}
$$

Compared to brute-force imaging, this approach halves the cost of near-zone corrections but it does not change the FFT costs for regions where the auxiliary grid encloses both an actual and an image structure, e.g., the free-space region in Fig. 2.2.1. It is more efficient to modify the Green functions and approximate the MOM matrices as:

$$
\begin{aligned}
\mathbf{X}_k^{\mathrm{aa}} \mp \mathbf{X}_k^{\mathrm{ai}} &\approx \mathbf{X}_k^{\mathrm{near,aa}} \mp \mathbf{X}_k^{\mathrm{near,ai}} + \mathbf{\Lambda}_k^{\mathrm{a}\dagger}(\mathbf{X}_{k,\mathrm{T}}^{\mathrm{FFT}} \mp \mathbf{X}_{k,\mathrm{H}}^{\mathrm{FFT}})\mathbf{\Lambda}_k^{\mathrm{a}} \\
{}_{\times}\mathbf{X}_k^{\mathrm{aa}} \mp {}_{\times}\mathbf{X}_k^{\mathrm{ai}} &\approx {}_{\times}\mathbf{X}_k^{\mathrm{near,aa}} \mp {}_{\times}\mathbf{X}_k^{\mathrm{near,ai}} + \Gamma_k^{\mathrm{a}\dagger}(\mathbf{X}_{k,\mathrm{T}}^{\mathrm{FFT}} \mp \mathbf{X}_{k,\mathrm{H}}^{\mathrm{FFT}})\mathbf{\Lambda}_k^{\mathrm{a}}
\end{aligned}
\tag{3.2.13}
$$

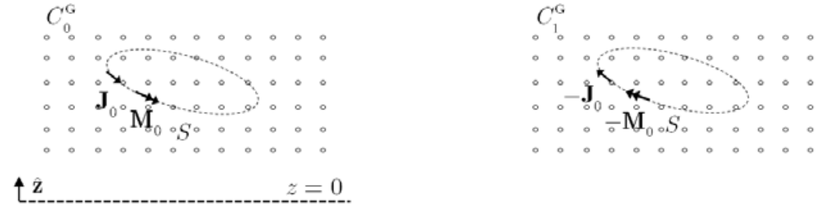

(a) (b)

Figure 3.2.2: The two multiple-grid AIM auxiliary grids used for Green-function modification: (a) C_0^{G} and (b) C_1^{G}.

The propagation and reflection matrices ($\mathbf{X}^{\mathrm{FFT}}_{k,\mathrm{T}}$ and $\mathbf{X}^{\mathrm{FFT}}_{k,\mathrm{H}}$) are constructed using identical auxiliary grids, which enclose only actual structures (Fig. 3.2.2), which are the same as them for the EH-PMCHWT formulation. Let C^{G}_k denote this smaller auxiliary grid with $N^{\mathrm{G}}_k = \delta_k N^{\mathrm{C}}_k$ grid points for region k; if region k is terminated on the plane, then $\delta_k \leq 0.5$; if it resides above the plane, then $\delta_k = 1$; if it resides below the plane, then $\delta_k = 0$ (i.e., C^{G}_k is not defined); e.g., $\delta_0 < 0.5$, $\delta_1 = 1$ and $\delta_2 = 0$ for the problem in Fig. 2.2.1. The propagation and reflection matrices are constructed using the $N^{\mathrm{G}}_k \times N^{\mathrm{G}}_k$ Green function matrices

$$\mathbf{G}^{\mathrm{x,y,z,A},\phi}_{k,\mathrm{P}}[u,u'] = \{\partial_x, \partial_y, \partial_z, \gamma_k, 1/\gamma_k\} g_{k,\mathrm{P}}(\mathbf{r}_u, \mathbf{r}_{u'}) \tag{3.2.14}$$

for $\mathrm{P} \in \{\mathrm{T}, \mathrm{H}\}$ and nodes u and u' on C^{G}_k ($\mathbf{G}^{\mathrm{x,y,z,A},\phi}_{k,\mathrm{P}}[u,u] = 0$).

The conversion scheme developed in Section 2.2 can be directly applied to the Hankel matrix-vector multiplication by using the anti-diagonal permutation matrix $\mathbf{P}$ [30]. Here are the detailed procedures: (i) Calculate the FFT of a zero-padded vector for $\mathbf{\Lambda}^{\mathrm{a},\nabla}_k \mathbf{I}$ and store it in $\overline{\mathbf{I}}^{\mathrm{a},\nabla}_k$. (ii) Multiply $\overline{\mathbf{I}}^{\mathrm{a},\nabla}_k$ element-by-element with the pre-computed FFT for $\mathbf{G}^{\phi}_{k,\mathrm{T}}$. (iii) Find the FFT for the re-ordered vector $\mathbf{P}^{-1}\mathbf{\Lambda}^{\mathrm{a},\nabla}_k \mathbf{I}$ by multiplying each element of $\overline{\mathbf{I}}^{\mathrm{a},\nabla}_k$ with the pre-computed FFT for $\mathbf{G}^{\phi}_{k,\mathrm{H}}\mathbf{P}$ that is multiplied by a phase shift term (to account for the re-ordering). (iv) Combine the vectors found in (ii) and (iii) and calculate the inverse FFT of the resulting vector. These require $O(8N^{\mathrm{G}}_k \log 8N^{\mathrm{G}}_k)$, $O(8N^{\mathrm{G}}_k)$, $O(8N^{\mathrm{G}}_k)$ and $O(8N^{\mathrm{G}}_k \log 8N^{\mathrm{G}}_k)$ operations, respectively; thus, only $O(8N^{\mathrm{G}}_k)$ extra operations produce $\mathbf{\Lambda}^{\mathrm{a}\nabla\dagger}_k(\mathbf{G}^{\phi}_{k,\mathrm{T}} \mp \mathbf{G}^{\phi}_{k,\mathrm{H}})\mathbf{\Lambda}^{\mathrm{a}\nabla}_k \mathbf{I}$, and $O(8N^{\mathrm{G}}_k)$ more operations produce $\Gamma^{\mathrm{a}\nabla\dagger}_k(\mathbf{G}^{\phi}_{k,\mathrm{T}} \mp \mathbf{G}^{\phi}_{k,\mathrm{H}})\mathbf{\Lambda}^{\mathrm{a}\nabla}_k \mathbf{I}$.

3.2.3. Multiple-Grid AIM Computational Complexity

When BFI is used, the multiple-grid AIM requires, for each region k, $O(2N^{\mathrm{nz,near}}_k + 8N^{\mathrm{C}}_k)$ bytes/operations to fill the non-zero and unique entries of $\mathbf{X}^{\mathrm{near}}_k$

and $\mathbf{X}_k^{\mathrm{FFT}}$ and $O(2N_k^{\mathrm{nz,near}} + 8[16N_k^{\mathrm{C}} \log 8N_k^{\mathrm{C}} + 8N_k^{\mathrm{C}}] + 12N_k^{\mathrm{C}})$ operations per iteration to multiply them. When GFM is used, only $\mathbf{X}_k^{\mathrm{near,aa}}$ and $\mathbf{X}_{k,\mathrm{T}}^{\mathrm{FFT}}$ exist if $\delta_k \in \{0,1\}$ and the multiple-grid AIM requires $O(2\delta_k N_k^{\mathrm{nz,near}} + 8N_k^{\mathrm{G}})$ bytes/operations to fill the unique entries of these matrices and $O(2\delta_k N_k^{\mathrm{nz,near}} + 8[16N_k^{\mathrm{G}} \log 8N_k^{\mathrm{G}} + 8N_k^{\mathrm{G}}] + 12N_k^{\mathrm{G}})$ operations per iteration to multiply them. Therefore, GFM exactly halves the computational costs for regions not terminated on the plane. For regions that are terminated on the plane ($\delta_k \leq 0.5$), GFM reduces the cost by a factor of $1/\delta_k$; this can be a very large factor if the structure is high above the plane (when $\delta_k \ll 0.5$). When $\delta_k \leq 0.5$, however, $\mathbf{X}_k^{\mathrm{near,ai}}$ and $\mathbf{X}_{k,\mathrm{H}}^{\mathrm{FFT}}$ also exist and an additional $O(8N_k^{\mathrm{G}})$ bytes/operations are needed to fill them and $O(64N_k^{\mathrm{G}})$ operations are needed to multiply them per iteration. While these additional costs reduce the $1/\delta_k$ gain, this is offset by several factors: (i) The correction cost is generally not negligible, i.e., rarely is $N_k^{\mathrm{nz,near}} \ll N_k^{\mathrm{G}}$. (ii) In the solution time, FFT cost dominates the multiplication cost by a logarithmic factor and the reduction in the FFT cost is greater than $1/\delta_k$ (by a logarithmic factor).

3.2.4. Validation

This section presents numerical examples to validate the Green function modification (GFM) approach for the CC-PMCHWT equations. Consider the same scattering problem as Section 2.2.4 (all the input parameters are the same as in that Section): A 200 MHz plane wave polarized along $(\theta, \phi) = (45^o, 0^o)$ is propagating to $(\theta, \phi) = (135^o, 0^o)$ direction and illuminates a $4\ \mathrm{m}$ diameter dielectric sphere of permittivity $\varepsilon_1 = 2\varepsilon_0$ that is located H meters above a PEC plane. The MOM and multiple-grid AIM using brute-force imaging and Green-function modification are contrasted when the sphere is located close to ($H = 0.25$ m) and far from ($H = 5$ m) the plane. The sphere surface is meshed using $N = 10\ 947$ edges and $N_0^{\mathrm{G}} = N_1^{\mathrm{G}} = N_0^{\mathrm{C}} = 40^3$ in either scenario but N_1^{C} increases from 40^3 to $40^2 \times 160$ in the latter case. Fig. 3.2.3 validates that the multiple-grid AIM acceleration produces visually identical RCS results with MOM; it also shows that Green-function modification approach produces practically identical results with brute-force imaging. Table 3.2.1 summarizes their computational requirements. The table shows, just as in Section 2.2.5.1, that MG-AIM-GFM is the most efficient method, is insensitive to H, and can reduce all costs by at least a factor of 2.

A comparison with the EH-PMCHWT solvers in Section 2.2 is in order (compare Tables 2.2.1 and 3.2.1). The MOM solution for CC-PMCHWT equations has double the matrix fill time and the same matrix solve time and memory for both imaging approaches. The multiple-grid AIM solver has double the matrix fill time, ~30% slower matrix solve time per iteration, and the same memory as the EH-PMCHWT one for both imaging approaches. The CC-PMCWHT solutions require one fifth number of iterations compared to the EH-PMCHWT ones.

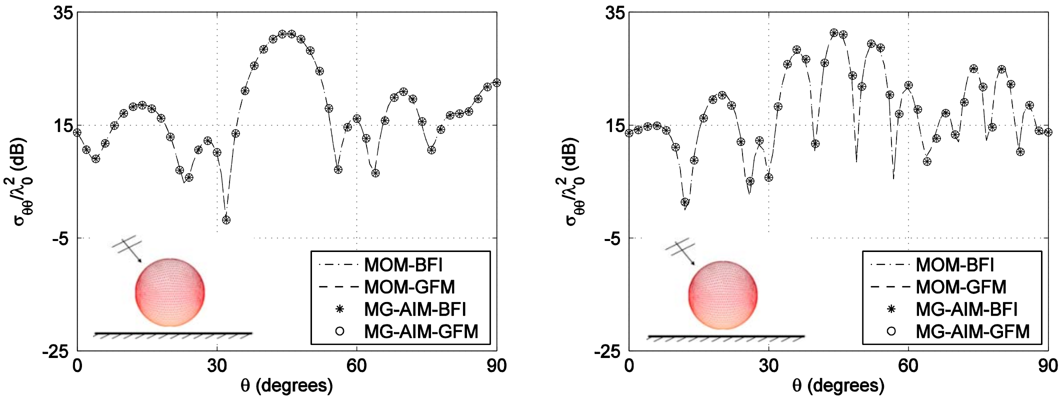

(a) (b)

Figure 3.2.3: VV-polarized RCS in the $x - z$ plane for a dielectric sphere H m above the PEC plane: (a) $H = 0.25$. (b) $H = 5$. The results are obtained using the CC-PMCHWT equations.

Table 3.2.1: Performance of CC-PMCHWT solvers for a dielectric sphere above a PEC plane

Method		Fill Time (s)	Solve Time per Iteration (s)	Number of Iterations	Memory (GB)
MOM-BFI		52 750	34.94	56	24.2
MOM-GFM		25 876	17.39	51	12.0
MG-AIM-BFI	$H = 0.25$	3402	12.06	56	1.4
	$H = 5$	3390	16.75	56	1.5
MG-AIM-GFM	$H = 0.25$	1720	6.51	61	0.72
	$H = 5$	1697	6.51	51	0.72

3.2.5. Summary

This section presented and contrasted two imaging approaches for the CC-PMCHWT based scattering analysis in the presence of a PEC/PMC plane. Numerical examples validated that modifying Green functions can achieve the same reduction as the EH-PMCHWT based solvers: It reduces the simulation time and memory requirement by a factor of (almost) 2 or larger compared to the brute force approach if the structure of interest is terminated on or resides above the plane, respectively.

3.3. MODELING METAMATERIAL REGIONS

For homogeneous regions of metamaterials, just like the EH-PMCHWT formulation, the CC-PMCHWT formulation is also directly applicable provided that the wave impedance and propagation constant are chosen carefully. Conservation of energy and passivity are enforced explicitly as described in Section 3.2. For validation, the same 1-m radius sphere composed of two hemispheres as in Section 2.3 is considered. Fig. 3.3.1 compares the RCS for the 3-region structure to the analytical Mie series results. Excellent agreement is observed in all cases, validating the CC-PMCHWT extension for metamaterial regions.

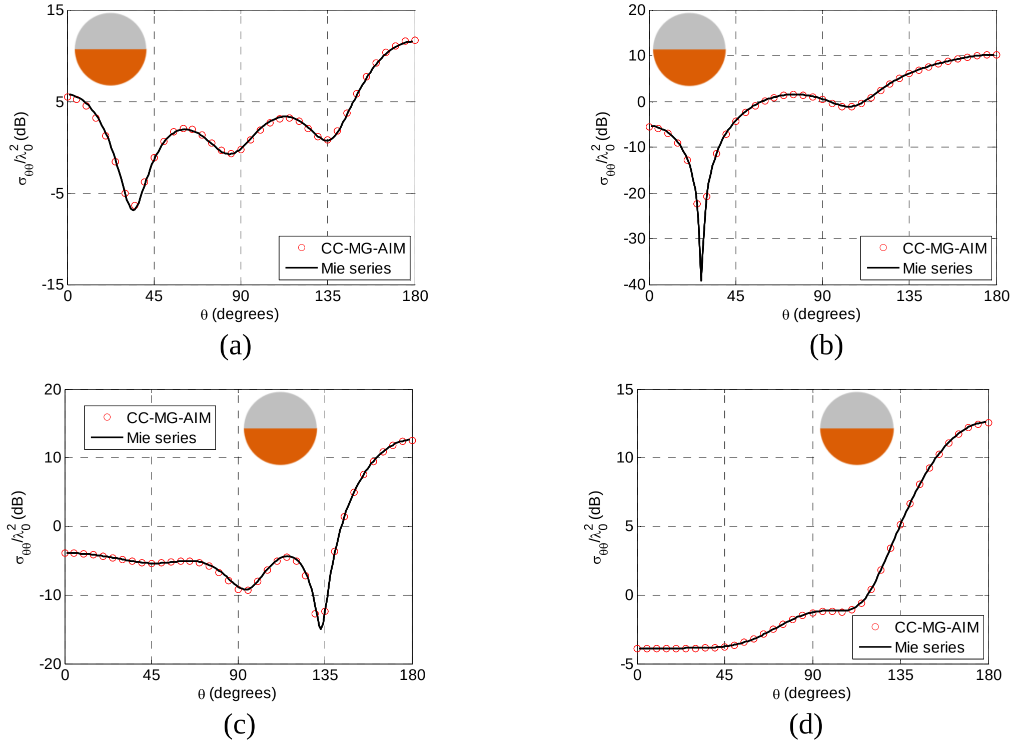

(a) (b) (c) (d)

Figure 3.3.1: Validation for metamaterial regions for the CC-PMCHWT equations. VV-polarized RCS in the $x-z$ plane at 150 MHz for a 1-m radius, three-region sphere composed of two identical hemispheres with (a) DPS-DPS. (b) DNG-DNG. (c) ENG-ENG. (d) MNG-MNG configuration.

Next, the same scattering problems used to validate metamaterials in Section 2.3 are solved using the CC-PMCHWT formulation. The formulation behaves similar to the EH-PMCHWT formulation, i.e., it does not suffer from a surface-plasmon resonance problem and will be ill posed for materials with constitutive parameters of $\{-\varepsilon_0, -\mu_0\}$ because the diagonal entries from DPS and DNG regions will almost cancel during the combination step (Both CC- and EH-PMCHWT follow the same combination recipe). Note that the CC-PMCHWT solutions required 51 iterations for both the $\{-3\varepsilon_0, -\mu_0\}$ and $\{-1.5\varepsilon_0, -1.5\mu_0\}$ spheres (Fig. 3.3.2(a) and 3.3.2(b)) while the EH-PMCHWT ones in Section 2.3 required 84 iterations for the former and 46 iterations for the latter. As mentioned in Section 3.1.5, the improvements in iterative solver convergence due to CC-PMCHWT formulation are problem dependent.

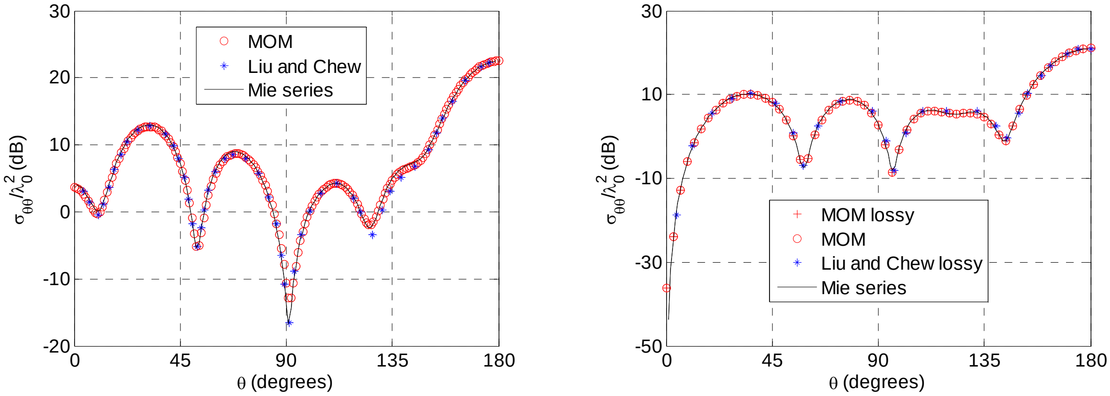

(a) (b)

Figure 3.3.2: Well-posedness of EH-PMCHWT solver for the DPS-DNG interface. VV-polarized RCS in the $x-z$ plane at 300 MHz for a 1-m radius DNG sphere: (a) $\{-3\varepsilon_0, -\mu_0\}$. (b) $\{-1.5\varepsilon_0, -1.5\mu_0\}$.

3.4. MODELING PEC/PMC REGIONS AND MATERIAL-PEC/PMC JUNCTIONS

CC-PMCHWT-based solvers can very easily treat structures that include PEC/PMC regions and material-PEC/PMC junctions. When closed PEC/PMC regions are present, the following modifications are implemented: No (internal) equivalent problems are formulated for them; only $\mathbf{J}_k$ or $\mathbf{M}_k$ is defined on S_k. For a PEC (PMC) region, only J-CFIEs (M-CFIEs), which are the linear combination of T-EFIE_{kl} (T-MFIE_{kl}) with N-MFIE_{kl} (N-EFIE_{kl}), are enforced on S_k:

$$\begin{aligned}\text{J-CFIE}_{kl} &= 1/\eta_k\, \text{T-EFIE}_{kl} + \text{N-MFIE}_{kl} \quad \text{for PEC region}\\ \text{M-CFIE}_{kl} &= \text{N-EFIE}_{kl} + \eta_k \text{T-MFIE}_{kl} \quad \text{for PMC region}\end{aligned} \tag{2.4.14}$$

The J-CFIEs (M-CFIEs) formulated for PEC (PMC) regions are concatenated with the CC-PMCHWT equations for the magnetodielectric regions [21, 36].

$$\sum_k \sum_l \beta_{kl} \begin{cases} \text{J-CFIE}_{kl} & \text{if } R_l \text{ is a PEC region} \\ \text{M-CFIE}_{kl} & \text{if } R_l \text{ is a PMC region} \\ \text{J-CFIE}_{kl} & \text{else} \\ \text{M-CFIE}_{kl} & \end{cases} \tag{2.4.14}$$

where $\beta_{kl} = \hat{\mathbf{p}}_{kl} \bullet \hat{\mathbf{n}}_{kl}$.

The above combination of CFIEs for PEC/PMC regions and CC-PMCHWT equations for magnetodielectric ones is free of internal resonance problems [21]. Moreover, the concatenation requires no additional modifications because the presence of N-EFIE and N-MFIE has already been accounted for in the CC-PMCHWT formulation. Therefore, the CC-PMCHWT formulation is much more convenient for the treatment of composite structures that include PEC/PMC-material junctions.

To validate the extension, the composite structure in Fig. 2.4.1(a), which is composed of dielectric regions, PEC regions, dielectric-PEC, and dielectric-dielectric junctions is analyzed from 400 MHz to 3.2 GHz. The composite structure is excited by an

$\hat{x}$-polarized plane wave propagating toward the $\hat{z}$ direction. The structure is meshed such that the average edge length is ~1/10th of the smallest wavelength in all regions which results in $N = 128\ 788$ ($1\ 620$ junction edges) and N=$8\ 287\ 904$ edges ($12\ 960$ junction edges) at 400 MHz to 3.2 GHz, respectively. Fig. 3.4.1(a) shows that the CC-PMCHWT solver requires fewer iterations than the EH-PMCHWT one for all cases but the improvement is inferior compared to the results in Section 3.1.4.3. Fig. 3.4.1(b) shows the agreement between the CC-PMCHWT and EH-PMCHWT results: the relative difference in the VV-polarized bistatic RCS using the error norm in (2.1.25) is less than 0.41% and 0.48% at 400 MHz and 3.2 GHz, respectively. Fig. 3.4.1(b) also shows that the RCS results agree with that obtained by a finite-element boundary-integral equation solver at 400 MHz [37]. Table 3.4.1 summarizes the computational requirements and shows that the proposed solver reduces the total simulation time by a factor of ~2.6 and increases the memory requirement less than 2% compared to the one in Section 2.4 at 3.2 GHz.

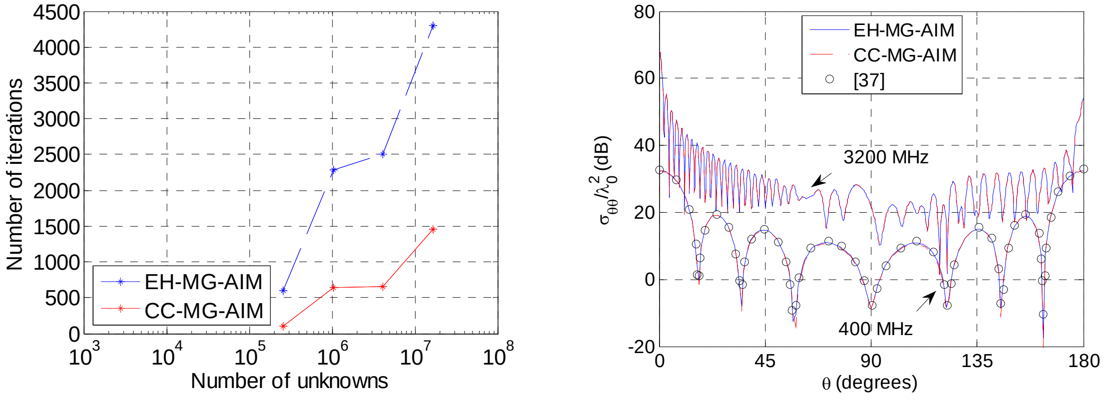

(a) (b)

Figure 3.4.1: CC- vs. EH-PMCHWT solvers for the composite structure in [37] as the frequency is increased. (a) Number of iterations needed for convergence. (b) Bistatic RCS at the $\phi = 0°$ plane at 400 MHz and 3.2 GHz.

Table 3.4.1: Computational requirements: CC- vs. EH-PMCHWT solvers for the composite structure as the frequency is increased.

Solver	EH-PMCHWT-MG-AIM		CC-PMCHWT-MG-AIM	
Frequency (MHz)	400	3200	400	3200
Fill Time (Hours)	4.2	184.1	6.2	219.1
Solve Time per Iteration (Hours)	7.9	13785	1.5	5167
Memory (GB)	6.5	395	6.6	395

Chapter IV Complex Scattering Applications

This chapter presents extensive numerical results to demonstrate the capabilities of the methods developed in Chapters II and III. Both EH- and CC-PMCHWT equations are used and solved with the multiple-grid AIM accelerated MOM to solve scattering problems relevant to wave propagation in forests and metamaterial structures.

4.1. WAVE PROPAGATION IN A MODEL FOREST

In this section, wave propagation in a model forest is analyzed in the HF frequency band, specifically at 40 MHz. The following forest model is derived from measurements [1, 39] in the Bastrop State Park forest in Texas, US, where the dominant tree species is the loblolly pine (*pinus taeda* L.). Given the complexity of the forest propagation environment, which contains a variety of materials and geometrical features at multiple length scales (e.g., tree leaves, branches, and trunks), the fidelity of the computational model must be carefully evaluated. In the literature, trees are commonly modeled as homogeneous dielectric cylinders for propagation and scattering studies by homogenizing/simplifying the material/geometrical properties [40, 41]. More complex models might be needed, however, because (i) in many species of trees, dielectric properties of the trunk strongly depend on its water content and exhibit significant radial variation, e.g., the loblolly pine trunk consists of inner heartwood and outer sapwood layers whose average water contents (the ratio of the mass of the moisture of the wood over its dry weight) are 33% and 110%, respectively [42], and (ii) branches and foliage can have significant impact on the scattered fields, especially for horizontal polarization [43]. While more complex material and geometrical models for trees may yield more accurate results, the model fidelity must be balanced with the computational cost. In the following, the multiple-grid AIM is used to quantify (i) the modeling errors and (ii) the computational requirements associated with different tree models.

4.1.1. Effects of Material and Geometrical Models

Three different dielectric models are evaluated for representing the Bastrop trunks, which were measured to be 20-m high and 0.3-m thick on average [1, 39]: A one-layer heartwood, a one-layer sapwood, and a two-layer dielectric cylinder model (Fig. 4.1.1). The thickness of the heartwood layer is a function of the tree age in general; for the Bastrop trees, the average heartwood thickness is 2/3 of the trunk diameter [44]. The heartwood and sapwood layers have ~33% and ~110% water content, respectively, and the wood density is $0.5\ \mathrm{g/cm^3}$ in the oven-dry condition [42]. Based on these assumptions and using the tables in [45], the permittivity and conductivity at 40 MHz are set to $\{\varepsilon_1, \sigma_1\} = \{50.59\varepsilon_0, 3.005\times 10^{-2}\ \mathrm{S/m}\}$ for the sapwood and $\{\varepsilon_2, \sigma_2\} = \{13.84\varepsilon_0, 6.397\times 10^{-3}\ \mathrm{S/m}\}$ for the heartwood layer; thus, the wavelengths in the two layers are $\lambda_1 \approx 0.14\lambda_0$ and $\lambda_2 \approx 0.27\lambda_0$. All trunk geometries are meshed by dividing the circumference into 8 subsections and setting the average vertical edge length to ~1/10th of the wavelength in the sapwood region. Thus, $N = N_0 = N_1 = 4584$ for the outer and inner region for the one-layer models and $N_0 = 4584$, $N_1 = 9072$, and $N_2 = 4536$ for the two layer model (of which $N_0^j = N_1^j = 16$ are junction edges at the top and bottom surfaces) for a total of $N = 9088$ edges. The AIM grid spacings are selected as $\{\Delta x_0, \Delta y_0, \Delta z_0\} = \lambda_0 / \{30, 30, 52\}$, $\{\Delta x_1, \Delta y_1, \Delta z_1\} = \lambda_0 / \{55, 55, 52\}$, and $\{\Delta x_2, \Delta y_2, \Delta z_2\} = \lambda_0 / \{37.5, 37.5, 52\}$; as a result, the one-layer models use $N_0^{\mathrm{C}} = 6\times 6\times 144$ and $N_1^{\mathrm{C}} = 9\times 9\times 144$ and the two-layer model uses $N_0^{\mathrm{C}} = 6\times 6\times 144$, $N_1^{\mathrm{C}} = 9\times 9\times 144$, and $N_2^{\mathrm{C}} = 6\times 6\times 144$ auxiliary grid points.

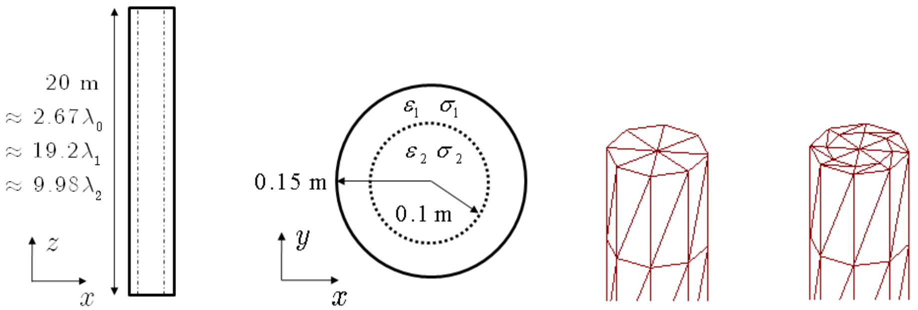

(a) (b) (c) (d)

Figure 4.1.1: One and two-layered trunk models and junctions. (a) The longitudinal cross section. (b) The transversal cross section. (c) Part of the mesh for the one-layer models. (d) Part of the mesh for the two-layer model.

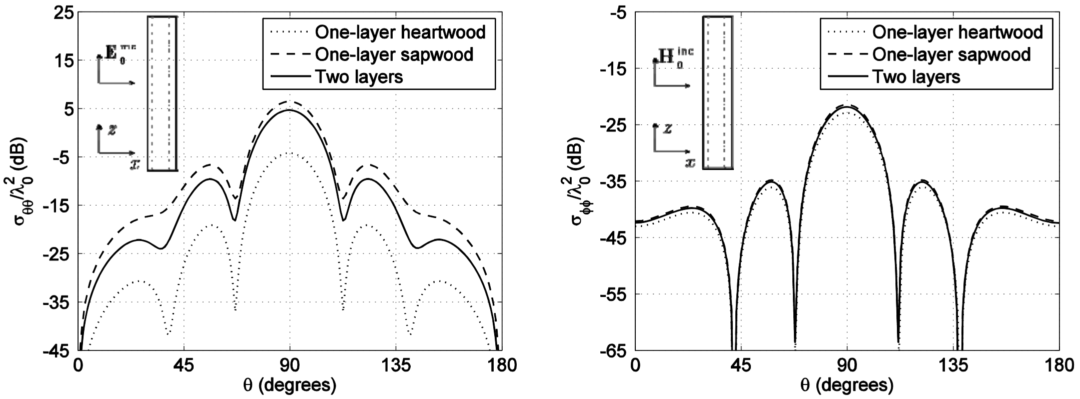

(a) (b)

Figure 4.1.2: Bistatic RCS for the three trunk models in the $x-z$ plane at 40 MHz: (a) The VV polarization. (b) The HH polarization.

Figure 4.1.2 compares the RCS patterns of the three models when they are excited by a normally incident plane wave. The VV patterns show significant differences (more than 10 dB difference in the backscattering direction) and the HH patterns appear to be less sensitive (less than 3 dB difference overall) to the trunk material. Indeed, using the two-layer model as the reference and measuring the RCS error over all angles as in (18), the VV- and HH-polarization errors $\{err_{\theta\theta}, err_{\phi\phi}\}$ for the one-layer heartwood and sapwood models are $\{86.63\%, 17.99\%\}$ and $\{53.47\%, 6.16\%\}$, respectively.

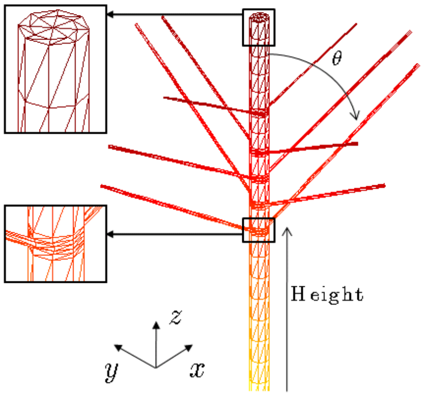

Figure 4.1.3: The two-layer trunk model with ten branches and part of its surface mesh.

To study the impact of branches, five pairs of primary branches are attached to the two-layer trunk model. The ten branches are modeled as sapwood-filled dielectric cylinders based on the physical characteristics of loblolly pine [46]. As shown in Fig. 4.1.3, these branches form five whorls, each of which has two symmetric branches. Neighbor whorls have 90° circumferential offset. As a result, three pairs of branches are parallel to the $x-z$ plane and two pairs are parallel to the $y-z$ plane. Branch pairs $1-5$ are at heights 16, 16.5, 17, 17.5, and 18.25 m (i.e., the bottoms of the branch-to-trunk connections are at these heights); have tilt angles θ of 58°, 60°, 61°, 62°, and 63°; and have diameters of 5.0, 5.5, 4.6, 3.8, and 2.8 cm, respectively. Each branch's length is set to 73.4 times its diameter based on the data in [46]. Thus, except for those in the first whorl, the higher the branch, the thinner, the shorter, and the more parallel to the ground it is. The structure is meshed by dividing the circumference of each trunk/branch cylinder into 8 subsections and setting the average edge length along the cylinders to ~1/10th of the wavelength in the sapwood region (smaller elements are used near the branch-trunk junctions) (Fig. 4.1.4). Thus, $N_0 = 9900$, $N_1 = 14388$, and $N_2 = 4536$ for a total of $N = 14404$ edges on the mesh. The AIM grid spacings are selected as before; as a result, $N_0^C = 36 \times 36 \times 144$, $N_1^C = 56 \times 54 \times 144$, and

$N_2^{\mathrm{C}} = 6 \times 6 \times 144$. Figure 4.1.4 plots the VV- and HH-polarized RCS patterns in the $x-y$ plane of the two-layer trunk model with and without the branches. It appears that the primary branches impact the HH pattern more significantly than the VV one: $\{err_{\theta\theta}, err_{\phi\phi}\} = \{0.52\%, 44.88\%\}$.

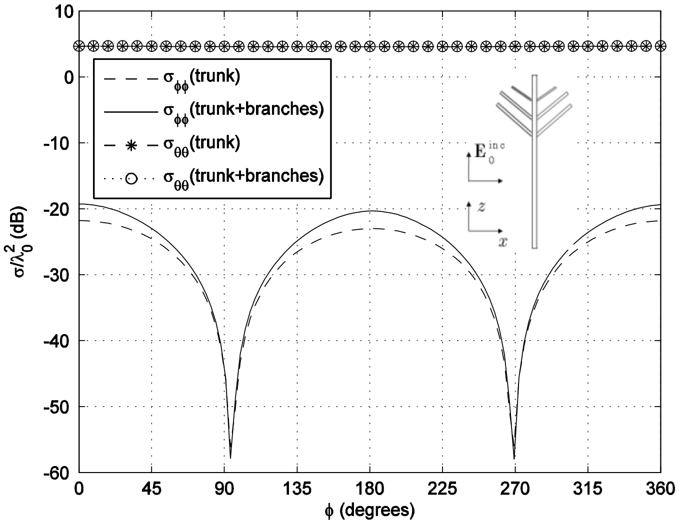

Figure 4.1.4: Bistatic RCS (VV and HH) for the two branch models in the $x-y$ plane at 40 MHz.

The above results show that the trunk materials and the branch geometries of the trees must be carefully modeled for analyzing propagation in a forest environment.

4.1.2. Tree Array—Computational Requirements

Next, the computational costs for different models are contrasted by analyzing radiation from a Hertzian dipole antenna inside an array of trees. Consider a uniform two-dimensional array of 4×20 trees on the $x-y$ plane with 7.8-m array spacing (Fig. 4.1.5). Each tree is modeled as either a one-layer sapwood trunk, a two-layer trunk, or a two-layer trunk with ten branches and meshed as in the previous subsection, i.e., $N = 366720$, $N = 727040$, and $N = 1152320$, respectively. Each model has

$K = 161$ different regions and thus 161 different AIM grids are used. AIM grids 1 through 160 are shifted versions of those in the previous subsection, whereas AIM grid 0 (for the external-most region) has more grid points, i.e., $N_0^C = 108 \times 640 \times 144$, $N_0^C = 108 \times 640 \times 144$, and $N_0^C = 128 \times 640 \times 144$ for the three models. All arrays are excited by either a z- or an x-oriented $0.1\lambda_0$-long Hertzian dipole located at the center of the array at a height of $z = 17.5$ m and the magnitudes of the incident and scattered co-polarized electric fields are observed as a function of the distance along the *y* direction in the center of the array (Fig. 4.1.6).The propagation results are consistent with the scattering results from the previous subsection. On the one hand, the scattered fields are affected more significantly by the trunk material than the branch geometry for the vertical polarization: The scattered fields for the one-layer model are up to ~2 dB higher and adding the branches has no visible effect (Fig. 4.1.6(b)). On the other hand, the scattered fields are affected more significantly by the branch geometry than the trunk material for the horizontal polarization: While the scattered fields for the one-layer model have up to ~5dB localized differences at the peak values with the two-layer model, adding branches causes ~10 dB change in the scattered fields (Fig. 4.1.6(c)). The computation costs of using each model is detailed in Table 4.1.1; the results show that from the lowest to highest fidelity tree model, the matrix fill time, matrix solve time per iteration, number of iterations, and memory requirement increase by factors of approximately 6, 6, 8, and 5, respectively. The results show that a one-layer trunk model with no branches should be an efficient and sufficiently accurate model for engineering analysis of vertically polarized wave propagation in loblolly pine forests, while a two-layer trunk model with branches might be necessary for analyzing horizontally polarized wave propagation.

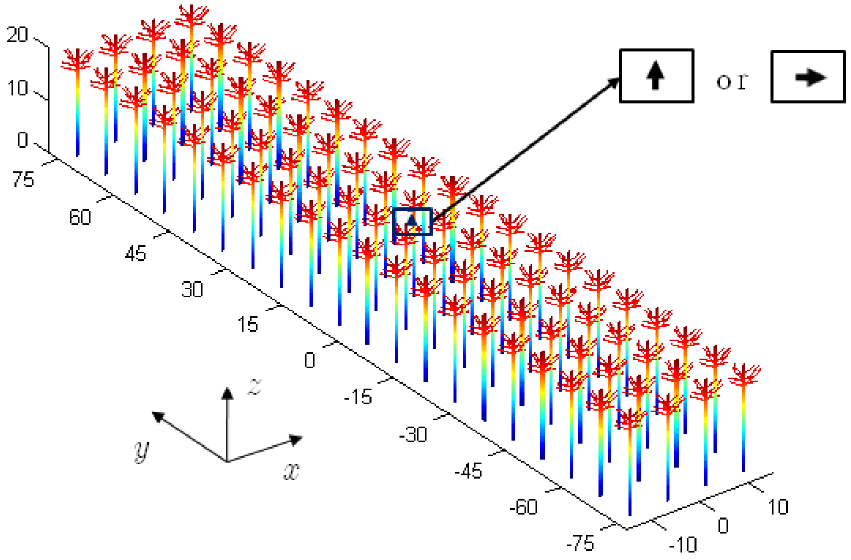

Figure 4.1.5: The 4×20 tree array and the vertically or horizontally oriented impressed $\lambda_0 / 10$ long Hertzian-dipole source located in the middle of the array at a height of 17.5 m.

Table 4.1.1: Computational requirements for the different tree models

Tree model (4×20 array)	Fill Time	Solve Time per Iteration	Number of Iterations	Memory
One-layer trunks	18544 s	1195 s	271	19.9 GB
Two-layer trunks	55872 s	2063 s	642	44.5 GB
Two-layer trunks+branches	117504 s	7232 s	2144	98.2 GB

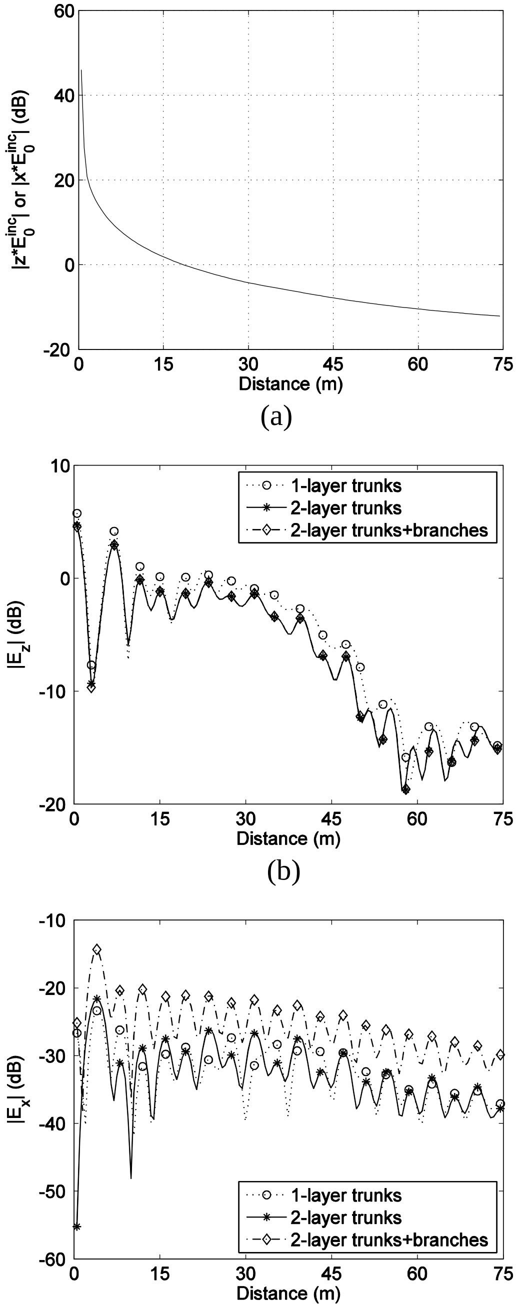

(a)

(b)

(c)

Figure 4.1.6: Magnitudes of co-polarized electric fields: (a) The incident electric field. (b) The z-directed electric field due to the z-directed antenna. (c) The x-directed electric field due to the x-directed antenna.

4.1.3. Tree Array—Comparison of Fast Solvers

Finally, the computational costs of CC-PMCHWT and EH-PMCHWT based solvers are contrasted by analyzing radiation from a Hertzian dipole antenna inside an array of trees. Consider again the array of 4×20 trees in Fig. 4.1.5. Each tree is modeled as a one-layer sapwood trunk with ten branches and meshed as in the previous subsection, i.e., $N = 1\ 584\ 000$. The AIM grids are identical to the ones in the previous subsection and the excitation is also the same. The magnitudes of the scattered electric fields found by both formulations are observed as a function of the distance along the *y* direction in the center of the array (Fig. 4.1.7).

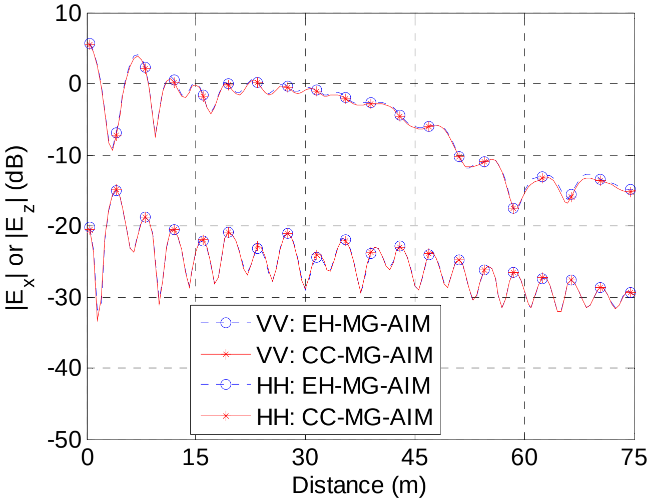

Figure 4.1.7: Magnitudes of co-polarized electric fields: The z-directed electric field due to the z-directed antenna (VV) or the x-directed electric field due to the x-directed antenna (HH).

Table 4.1.2: Computational requirements: CC- vs. EH-PMCHWT solvers

Solver	Fill Time	Solve Time per Iteration	Number of Iterations	Memory
EH-MG-AIM	68232 s	2457 s	2151	62.3 GB
CC-MG-AIM	146360 s	2922 s	461	67.9 GB

The computational costs of each solver is detailed in Table 4.1.2; the results show that the CC-PMCHWT solver increases the matrix fill time, matrix solve time per iteration, and memory requirement by approximately 110%, 15%, and 9%, respectively, but reduces the number of iterations by a factor of 3.7, and eventually reduces the total simulation time (setup and solution costs) by a factor of 3.6. The results show that the CC-PMCHWT and EH-PMCHWT solvers yield practically the same field distribution along the central line for both VV- and HH-polarized propagation.

4.1.4. Summary

This section demonstrated the applicability of the multiple-grid AIM scheme to complex scattering problems by analyzing HF-band wave propagation in an 80-tree forest model. The forest simulations quantified the modeling errors and computational costs associated with low- and high-fidelity tree models and illustrated the trade-off between model fidelity and analysis cost for the method. Moreover, the computational costs and convergence performance of CC-PMCHWT and EH-PMCHWT solvers were contrasted and the better performance of the CC-PMCHWT solver was observed. The results show that the EH-PMCHWT formulation requires more iterations as the model fidelity increases and this can be ameliorated by adopting the CC-PMCHWT formulation with little extra computational costs.

4.2. TRANSMISSION LOSS IN DIELECTRIC-ROD ARRAY

In this section, the multiple-grid AIM accelerated MOM solution of EH-PMCHWT equations with the incorporation of a PEC plane is applied to investigate wave propagation in a finite array of dielectric rods on a PEC ground plane. The simulations are carried out in a broad frequency band, specifically from 0.3 GHz to 4.0 GHz, and compared to the experimental data.

4.2.1. Experimental Setup

Figure 4.2.1: Experimental setup of the water straw array [39].

The A scale model was built in [39] to experimentally investigate HF-band wave propagation in forests. The structure consists of a 6×36 periodic array of plastic straws sealed at the bottom and filled with fresh water (Fig. 4.2.1). Each straw has a height of 205 mm and a diameter of 7.6 mm; the period is 60 mm in both directions. A metal ground plane is used to model earth; transmitting and receiving monopoles are embedded into the array to collect the transmission-loss data along the central observation line. Three pairs of monopoles with heights 100 mm, 50 mm, and 20 mm are used to cover the frequency band (all have radii of 0.5 mm). At each frequency, the transmitter is fixed at the center observation line with a shift of 6 periods from the end of the array; the receiver is moved away from the transmitter along the center observation line by changing the distance from 0.5 m to 1.5 m with a step of 0.025 m (41 observation positions). By varying the spacing between the transmitter and receiver and changing the operating frequency, the wideband transmission data S_{21} are recorded using a vector network analyzer. The transmission loss is then quantified as a function of the distance between the transmitter and receiver and the operating frequency and normalized by $\sqrt{1-|S_{11}|^2}$ and $\sqrt{1-|S_{22}|^2}$ to remove the mismatch effects of the transmitter and receiver, i.e.,

$$\text{Transmission Loss} = 20\log\frac{S_{21}}{\sqrt{(1-|S_{11}|^2)(1-|S_{22}|^2)}} \tag{4.2.1}$$

4.2.2. Simulation Model and Comparison to Experiments

In the following simulations, the metal ground plane is modeled as an infinite PEC plane using the Green function modification approach detailed in Section 3.2. The 6×36 periodic straws filled with fresh water are modeled as pure-water rods. Based on this assumption and using the tables in [45], the permittivity and conductivity of fresh water are linearly interpolated from $\{\varepsilon_1,\sigma_1\}=\{77.5\varepsilon_0, 2.069\times 10^{-2}\,\mathrm{S/m}\}$ at 0.3 GHz to $\{\varepsilon_1,\sigma_1\}=\{73.6\varepsilon_0, 4.083\,\mathrm{S/m}\}$ at 4.0GHz in the frequency band of interest. For the entire band, 38 frequency samples are simulated and the results for the remaining frequencies are linearly interpolated from these data.

For the low-frequency band (0.3-1.4 GHz), each rod cylinder circumference is divided into 8 subsections to resolve the circular cross section and the length is divided into 62 subsections meshed such that the average edge length is ~1/10th of the wavelength of 1.4 GHz in the rod; thus, the number of edges on each cylinder is the same ($N_1 = \ldots = N_{K-1} = N_0/(K-1) = 1664$) and $N=(K-1)N_1$. The AIM grid spacings are optimized at 1.4 GHz and selected as $\{\Delta x_0, \Delta y_0, \Delta z_0\} = \lambda_0/\{33,38,50\}$, and $\{\Delta x_1, \Delta y_1, \Delta z_1\} = \lambda_0/\{50,50,50\}$; as a result, $N_0^{\mathrm{C}} = 240\times 48\times 60$ for the external region and $N_1^{\mathrm{C}} = N_2^{\mathrm{C}} = \ldots = N_{217}^{\mathrm{C}} = 9\times 9\times 45$ auxiliary grid points.

For the middle-frequency band (1.5-2.5 GHz), each rod cylinder circumference is divided into 8 subsections to resolve the circular cross section and the length is divided into 136 subsections meshed such that the average edge length is ~1/10th of the wavelength of 2.5 GHz in the rod; thus, the number of edges on each cylinder is the same ($N_1 = ... = N_{K-1} = N_0 / (K-1) = 3296$) and $N = (K-1)N_1$. The AIM grid spacings are optimized at 2.5 GHz and selected as $\{\Delta x_0, \Delta y_0, \Delta z_0\} = \lambda_0 / \{32, 28, 40\}$, and $\{\Delta x_1, \Delta y_1, \Delta z_1\} = \lambda_0 / \{50, 50, 40\}$; as a result, $N_0^{\mathrm{C}} = 480 \times 64 \times 90$ for the external region and $N_1^{\mathrm{C}} = N_2^{\mathrm{C}} = ... = N_{217}^{\mathrm{C}} = 9 \times 9 \times 63$ auxiliary grid points.

For the high-frequency band (2.6-4.0 GHz), each rod cylinder circumference is divided into 12 subsections to resolve the circular cross section and the length is divided into 270 subsections meshed such that the average edge length is ~1/10th of the wavelength of 4.0 GHz in the rod; thus, the number of edges on each cylinder is the same ($N_1 = ... = N_{K-1} = N_0 / (K-1) = 9840$) and $N = (K-1)N_1$. The AIM grid spacings are optimized at 4.0 GHz and selected as $\{\Delta x_0, \Delta y_0, \Delta z_0\} = \lambda_0 / \{16, 14, 40\}$, and $\{\Delta x_1, \Delta y_1, \Delta z_1\} = \lambda_0 / \{50, 50, 40\}$; as a result, $N_0^{\mathrm{C}} = 480 \times 64 \times 140$ for the external region and $N_1^{\mathrm{C}} = N_2^{\mathrm{C}} = ... = N_{217}^{\mathrm{C}} = 12 \times 12 \times 120$ auxiliary grid points.

The transmitter and receiver are PEC thin wire antennas on the ground plane; the transmitter is excited by a delta-gap source at the bottom; the receiver is loaded with a $50\,\Omega$ resistor at the bottom. For each frequency, the transmitter is fixed at the center observation line with a shift of 6 periods from the end of the array; the receiver is moving away from the transmitter along the center observation line by changing the distance from 0.5 m to 1.5 m with a step of 0.025 m (41 observation positions). Three pairs of antennas with heights of 100 mm, 50 mm, and 20 mm are used for the entire band, which are divided into segments to ensure the length of each segment is less than 1/10th of the wavelength in free space. The transmission loss of each observation position can be evaluated as $10\log|I_r^2 R_r| \big/ [|V_t I_t|(1-|S_{22}|^2)]$, where I_r, R_r, V_t, and I_t represent the current on the receiver, the resistance load on the receiver, the voltage on the transmitter, and the current on the transmitter, respectively.

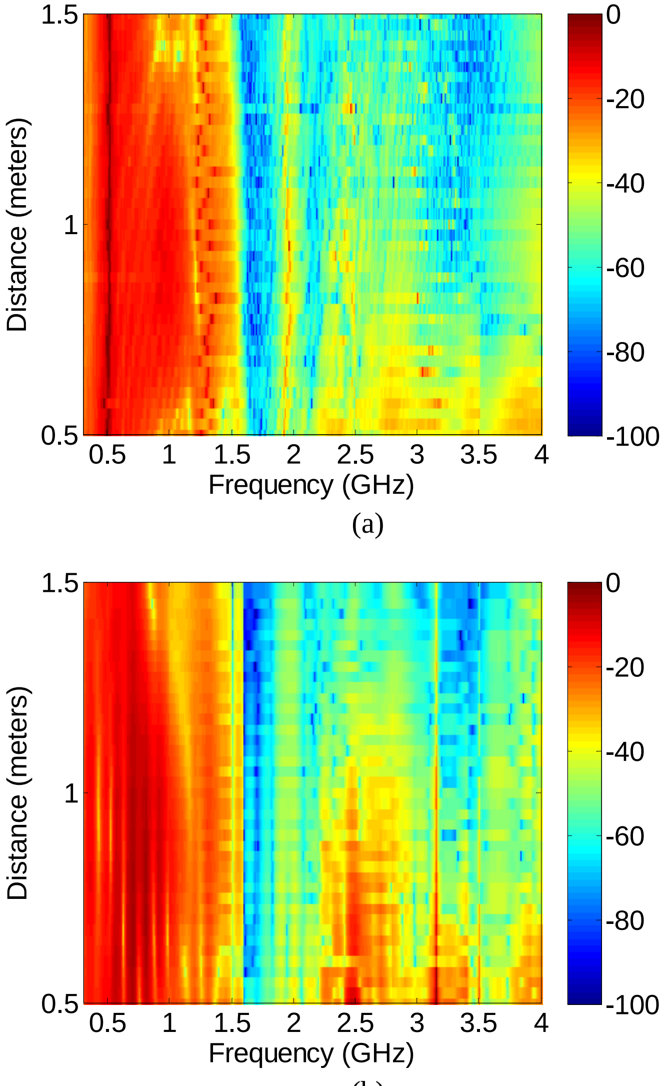

(a)

(b)

Figure 4.2.2: Transmission loss in the periodic dielectric-rods: (a) Measurement. (b) Simulation.

Figure 4.2.2 compares the transmission loss data found from measurements and simulations. The results shows good agreement, e.g., both results capture two stop-bands at 1.6-2.3 GHz and 3.0-3.7 GHz and a narrow pass-band at 2.0 GHz.

4.2.3. Computational Requirements

The computational costs of the EH-PMCHWT multiple-grid AIM scheme for different frequency bands are contrasted and detailed for three sample simulations in Table 4.2.1; the results show that from the low to high frequency, the matrix fill time, matrix solve time per iteration, and memory requirement linearly scale with the number of unknowns.

Table 4.2.1: Computational requirements for the different frequency bands

Frequency band	Fill Time	Solve Time per Iteration	Number of Iterations	Memory
0.3-1.4 GHz	31 488 s	309.6 s	1251	24.9 GB
1.5-2.5 GHz	50 304 s	757.4 s	1741	53.7 GB
2.6-4.0 GHz	222 048 s	1719.4 s	3451	111 GB

4.2.4. Summary

This section demonstrated the applicability of the EH-PMCHWT multiple-grid AIM scheme to complex scattering problems by analyzing wave propagation in a 6×36 periodic water straw array and correlating the results with independent measurements. The simulations showed good agreement with measurements and accurately predicted the pass/stop-band behavior. Moroever, the computational costs associated with simulations at different frequency bands were quantified.

4.3. WAVE PROPAGATION IN NATURAL FOREST

In this section, the multiple-grid AIM accelerated MOM solution of EH-PMCHWT equations with the incorporation of a PEC plane is applied to investigate wave propagation in natural forested environment with randomly distributed trees at HF/VHF band, specifically from 20 MHz to 45 MHz, and compared to experimental data.

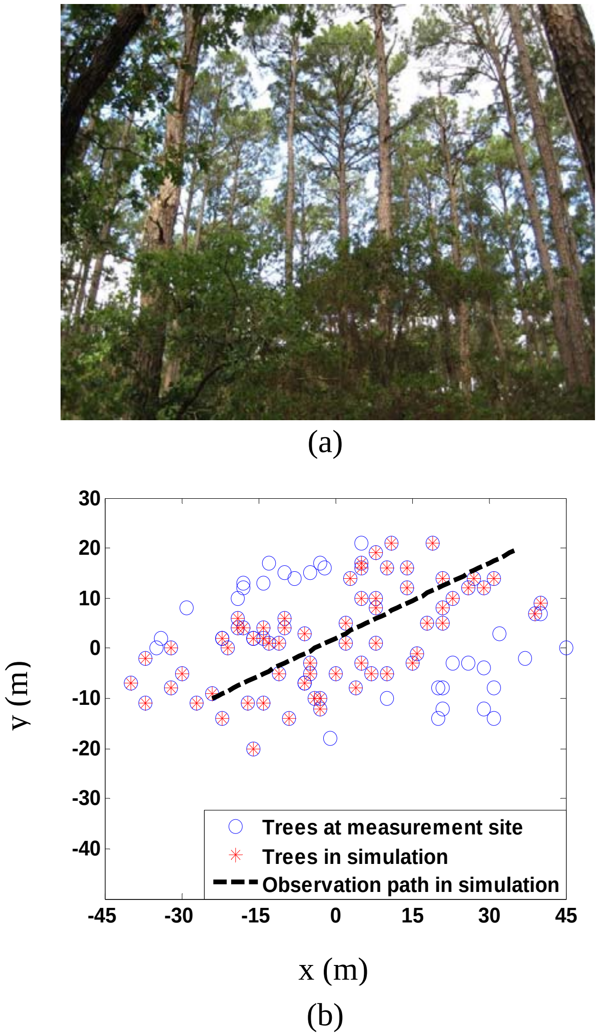

Figure 4.3.1: (a) Photo of the measurement site. (b) Tree distribution at the measurement site and the simulation setup.

The measurement was conducted in a loblolly-pine dominated forest in Bastrop State Park. The trees were in full foliage. Fig. 4.3.1 shows a photo of the trees and the positions of the trees that were recorded using a GPS receiver. The diameters of the trees were measured at the collection site and the heights of the trees were estimated using a clinometer. The average tree height, trunk diameter, and spacing were found to be approximately 20 m, 0.3 m, and 4.5 m, respectively.

The forest transmission-loss measurement setup was similar to the laboratory measurements in [39]: Identical vertical monopoles connected to a vector network analyzer (VNA) were used to transmit and receive power. A power amplifier was cascaded between the VNA and the transmitting antenna to amplify the transmit power. Three different antenna sets were employed to cover the 20-100 MHz frequency band and S_{21} (not time averaged) was recorded across the frequency band as the distance between the receiving and transmitting antennas was varied from 30 m to 60 m in steps of 1.5 m. The frequency step was 0.11875 MHz. For comparison and calibration, a similar measurement using the same setup was conducted in an open field at the University of Texas Pickle Research Center. When compared with the measurements conducted in an open field, a clear resonant behavior was observed in the forest data from 33 MHz to 42 MHz. In this band, the propagation constant of the dominant propagation mode could be smaller than that of free space and the attenuation was higher than in neighboring frequencies.

4.3.1. Material and Geometrical Modeling

The phenomena observed in the measurements were investigated by conducting full-wave simulations. In the simulations, the measurement setup was modeled as follows. Trees were modeled as identical homogenous dielectric cylinders above a perfectly conducting ground plane; the cylinder thickness and height were set to the average measured values for the trunks; and the cylinders represented by the red stars were positioned at the measured tree locations shown by the blue circles in Fig. 4.3.1 (b). As shown in Section 4.1.2 and [23], vertically polarized fields propagating through a forest of loblolly pine trees can be calculated sufficiently accurately with such a simple model at the HF/VHF frequency band, e.g., branches have little effect on the vertically polarized fields. The model forest was excited by impressed $0.1\lambda_0$ monopoles located at $\{x,y\}=\{\text{-}25.0,\text{-}10.7\}$ m in Fig. 4.3.1(b), where λ_0 denotes the wavelength in free space at the frequency of interest; the operating frequency was varied from 20 to 45 MHz using 1-MHz frequency steps (i.e., 26 different antennas were used); and the vertical electric fields were recorded along the path indicated by the black dash line in Fig. 4.3.1(b). Note that only 66 of the trees closest to the path were modeled because of the high computational demands of the full-wave simulation. The water content (the ratio of the mass of the moisture of the wood over its dry weight) and the wood density of loblolly pine is ~100% and 0.5g/cm^3, respectively. Using this information, the dielectric parameters of trees were interpolated from the data in [45] in the frequency band of interest: The relative permittivity linearly decreased from 54.3 to 48.3 and the conductivity linearly increased from 0.0258 to 0.0541 S/m as frequency increased from 20 to 45 MHz.

To minimize the computational demands, the frequency band of interest was divided into three sub-bands (20-30, 31-40, and 41-45 MHz) and three different triangular meshes were used to cover them; each mesh divided the cylinder circumference into 8 subsections and set the average vertical edge length to ~1/10th of the wavelength inside the dielectric cylinder at the highest frequency in the sub-band. These meshes resulted in $953\ 568$, $1\ 226\ 016$, and $1\ 492\ 128$ degrees of freedom for the model forest. The spacings of the auxiliary Cartesian grids used for accelerating the calculations in each region [23] were also chosen as ~1/10th of the wavelength in that region at the highest frequency of interest in the sub-band.

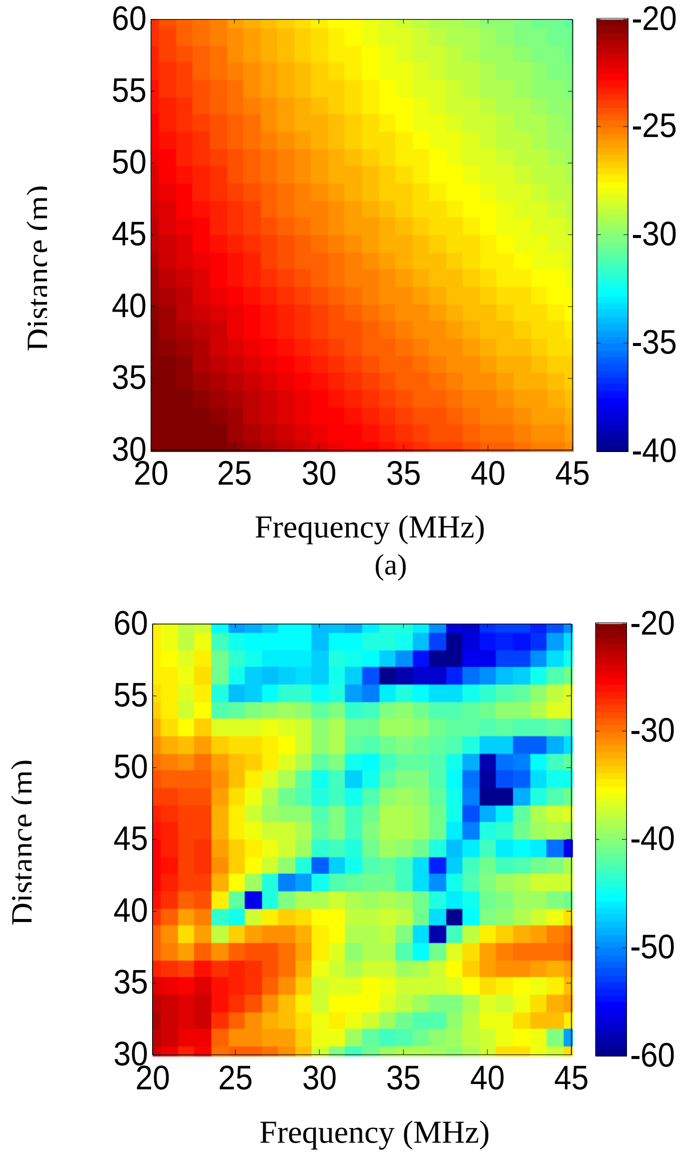

(a)

(b)

Figure 4.3.2: The transmission loss of (a) free space and (b) a simplified model of the forest.

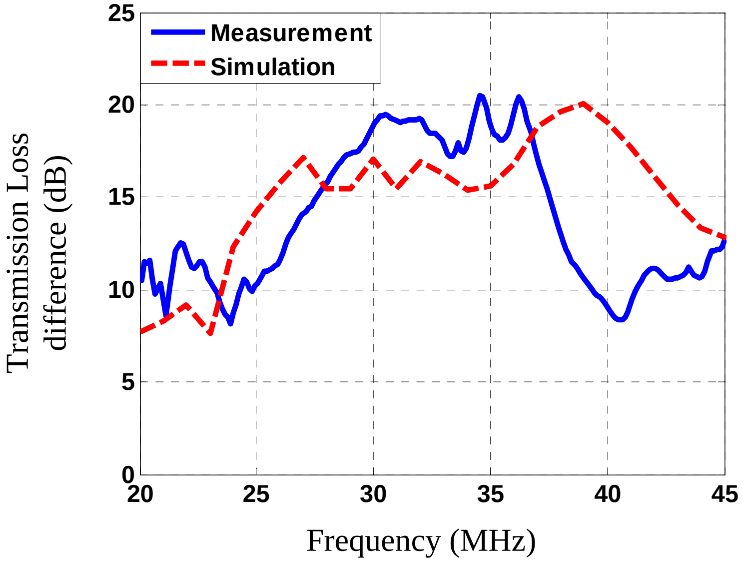

Figure 4.3.3: The averaged transmission loss difference in the resonance frequency: measurement vs. simulation.

Figs. 4.3.2(a) and (b) show the simulated transmission loss of the free space and the model forest, respectively. They confirm that the waves experience much higher loss in the forest. Next, the averaged transmission loss $\overline{\Delta S_{21}}$ for each frequency is then quantified as $\overline{\Delta S_{21}}\left(f\right)=\sum_{i=1}^{N}\Delta S_{21}\left(f,i\right)/N$, where N represents the number of observation points. $\overline{\Delta S_{21}}$ is computed in the 20-45 MHz frequency band and the results are plotted in Fig. 4.3.3. It is shown that the simulation is consistent with measurement. The simulated $\overline{\Delta S_{21}}$ is greater than 15 dB in the 28-43 MHz range. It should be pointed out that while the full-wave simulations capture the qualitative behavior in the measurement, detailed quantitative differences exist between the two because of the simplifications made in modeling the forest, e.g., the limited number of modeled trees, the use of identical trees, simplifications in geometry/material parameters, as well as the deterministic (single) simulation of the quasi-random propagation environment.

When compared with the measurement, a clear resonant behavior was observed from 33 to 42 MHz. In this band, the propagation constant of the dominant propagation mode could be smaller than that of free space and the attenuation was higher than in neighboring frequencies. Interestingly, the average tree spacing (4.5 m) was close to half-wavelength around 33 MHz, which offers a possible explanation of the observed resonance.

4.3.2. Summary

This section demonstrated the applicability of the EH-PMCHWT multiple-grid AIM scheme to complex scattering problems by analyzing wave propagation in a natural forest. The simulation results captured the resonance behavior of the transmission loss, which could be directly correlated to the permittivity-less-than-one behavior observed in natural forest.

4.4. METAMATERIAL HOMOGENIZATION PROBLEM

In this section, the multiple-grid AIM accelerated MOM solution of CC-PMCHWT equations is applied to investigate metamaterial homogenization problem. Metamaterials represent artificial composite structures based on specific subwavelength unit cells with appropriate placements for realizing exotic material properties not found in nature. Recently, metamaterials have been applied to electromagnetic and optical devices, such as antenna [47] and lens [48], to achieve breakthrough performances that conventional materials cannot reach. These exotic properties are achieved though sophisticated interaction and coupling effects between the tailored unit cells and are also usually dependent on external excitations. To take advantage of exotic properties of metamaterials, their effective response and equivalent bulk parameters must be accurately evaluated. The homogenization theory, developed in [49] and [50], can be applied to estimate the bulk effective material parameters of aggregated magnetodielectric particle arrays and similar near- and far-field distributions can be expected from such aggregated and homogenized metamaterials.

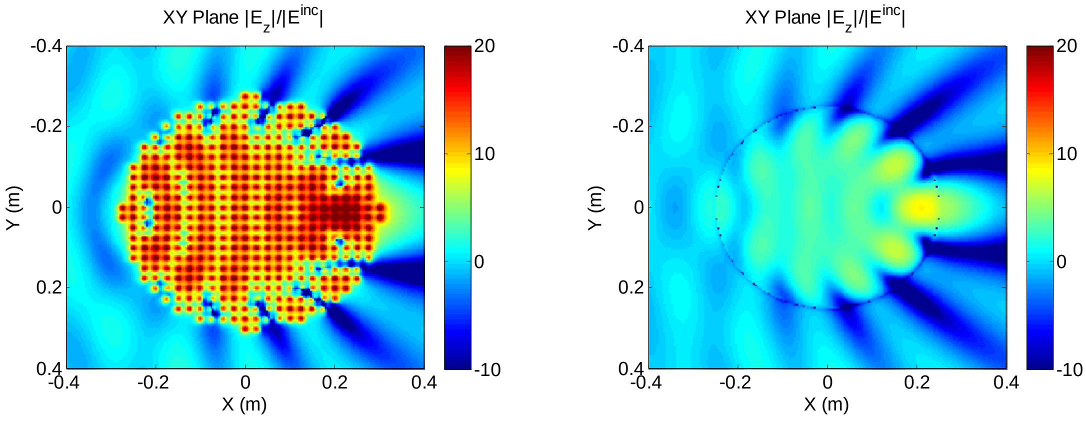

(a) (b)

Figure 4.4.1: The electric field distribution of (a) aggregated metamaterial, (b) homogenized metamaterial for a short disk in the double-positive material regime.

Consider a two-layer cylindrical aggregated metamaterial composed of 1696 magnetodielectric spheres (each layer has 848 spheres; the radius has 12 unit cells with an array period $d = 25\ \mathrm{mm}$), where each sphere has a radius of $a = 11.25\ \mathrm{mm}$, permittivity of $\varepsilon_1 = ... = \varepsilon_{1696} = 13.8\varepsilon_0$ and permeability of $\mu_1 = ... = \mu_{1696} = 11.0\mu_0$. The homogenized structure is a disk centered at the origin and is of radius 0.25 m and height 0.0475 m. Both structures are excited by a 1.0 GHz $\hat{z}$-polarized plane wave propagating toward $\hat{x}$ direction. The equivalent bulk parameters of the homogenized metamaterial disk are $\varepsilon_1 = 2.752\varepsilon_0$ and $\mu_1 = 2.752\mu_0$ at this frequency [51]. Both the small spheres and equivalent disk are meshed by setting the average edge length to be ~ $1/10$ of the minimum wavelength, which require $N = 1\,404\,288$ and $N = 10\,800$ edges, respectively. For the aggregated metamaterial, there are $K = 1697$ different regions; AIM grid 0 (for the external-most region) has $N_0^{\mathrm{C}} = 320 \times 320 \times 30$ gird points and the remaining AIM grids are of identical size (but at different locations) with $N_1^{\mathrm{C}} = ...N_{1697}^{\mathrm{C}} = 18 \times 18 \times 18$. For the homogenized metamaterial, the disk has $K = 2$ different regions and identical AIM grids with $N_0^{\mathrm{C}} = N_1^{\mathrm{C}} = 40 \times 40 \times 10$.

Figs. 4.4.1 (a)-(b) show the near-field distributions on the center transversal planes of the aggregated metamaterial and the homogenized metamaterial disk, respectively. The comparison demonstrates good agreement of field variations outside the metamaterial region; significant local differences exist inside the material region, but this is to be expected as the homogenization smooths out the small geometry features and field variations. The results validate the homogenization theory of [51] in the double-positive material regime.

Next, consider 3-D cubic aggregated metamaterials composed of the same magnetodielectric spheres as above (the same period, radius, and material parameters). The metamaterial arrays are of size $4 \times 4 \times 4$, $6 \times 6 \times 6$, and $10 \times 10 \times 10$ (shown in

Fig. 4.4.2). Both aggregated and homogenized models are excited by a 1.454 GHz $\hat{x}$-polarized plane wave propagating toward $-\hat{z}$. The equivalent bulky parameters of the homogenized metamaterial cube are $\varepsilon_1 = -0.9936\varepsilon_0$ and $\mu_1 = -0.6063\mu_0$ at this frequency. Both the spheres and equivalent cube are meshed by setting the average edge length to be ~$1/10$ of the minimal wavelength. Thus, the $4\times4\times4$, $6\times6\times6$, and $10\times10\times10$ aggregated spheres are meshed using $N = 105\ 984$, $N = 357\ 696$, and $N = 1\ 656\ 000$ edges, respectively; the corresponding homogenized cubes require only $N = 2\ 592$, $N = 5\ 832$, and $N = 16\ 200$ edges, respectively. For the three aggregated metamaterials, the spheres have $K = 65$, $K = 217$, and $K = 1001$, different regions and thus 65, 217, and 1001 different AIM grids are used. AIM grid 0 (for the external-most region) has $N_0^{\mathrm{C}} = 72\times72\times72$, $N_0^{\mathrm{C}} = 96\times96\times96$, or $N_0^{\mathrm{C}} = 160\times160\times160$ points for the $4\times4\times4$, $6\times6\times6$, and $10\times10\times10$ case, respectively, and $N_1^{\mathrm{C}} = \ldots N_K^{\mathrm{C}} = 20\times20\times20$ for all cases. For the homogenized metamaterial, the cube has 2 different regions and identical AIM grids, i.e., $N_0^{\mathrm{C}} = N_1^{\mathrm{C}} = 16\times16\times16$, $N_0^{\mathrm{C}} = N_1^{\mathrm{C}} = 20\times20\times20$, and $N_0^{\mathrm{C}} = N_1^{\mathrm{C}} = 32\times32\times32$ for all regions.

Figs. 4.4.3-4.4.5 demonstrates the near-field distributions on the center transversal planes on $x-y$, $x-z$ and $y-z$ planes and RCS patterns on $x-z$ and $y-z$ planes. The comparison demonstrates that although better agreement is achieved when more spheres are aggregated, homogenization gives satisfactory results even for a small collection of spheres. The good agreement of field variations both inside and near the aggregated metamaterial as well as the far-field patterns validates the homogenization theory in the double-negative material regime.

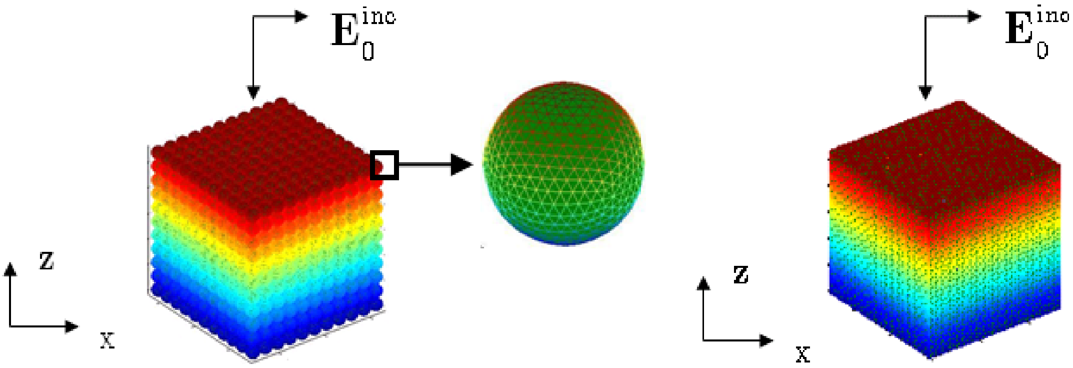

(a) (b)

Figure 4.4.2: Configuration of the aggregated and homogenized metamaterials. (a) The $10 \times 10 \times 10$ aggregated spheres. (b) The homogenized metamaterial cube.

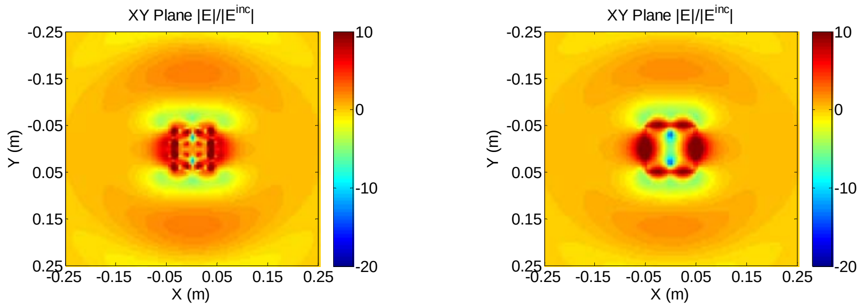

(a) (b)

Figure 4.4.3: The field distributions for the $4 \times 4 \times 4$ aggregated metamaterial and the corresponding homogenized metamaterial cube in the double-negative material regime. Total electric field distribution of the (a) aggregated and (b) homogenized metamaterial in the $x-y$ plane. Total magnetic field distribution of the (c) aggregated and (d) homogenized metamaterial in the $x-z$ plane. Total electric field distribution of the (e) aggregated and (f) homogenized metamaterial in the $y-z$ plane. The VV- and VH- RCS patterns for the aggregated and homogenized metamaterials in the (g) $x-z$ and (h) $y-z$ planes.

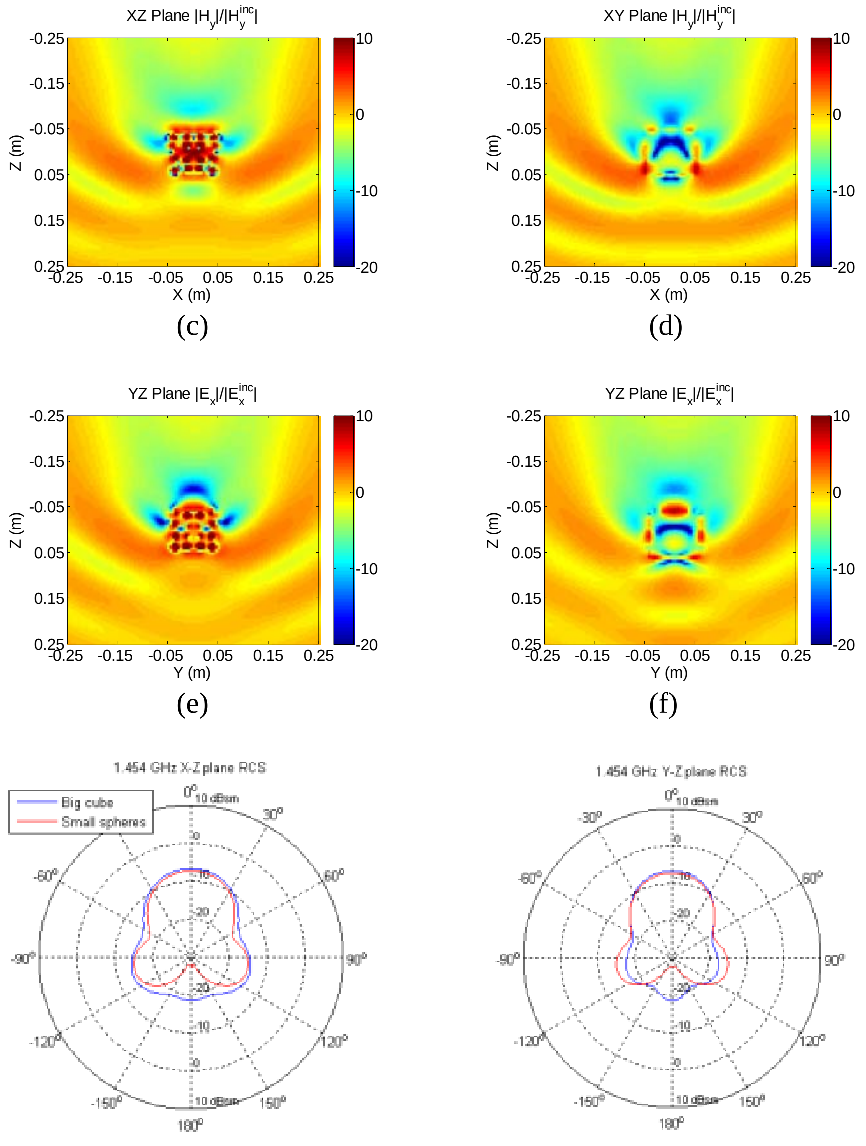

(c) (d)

(e) (f)

(g) (h)

Figure 4.4.3: Continued.

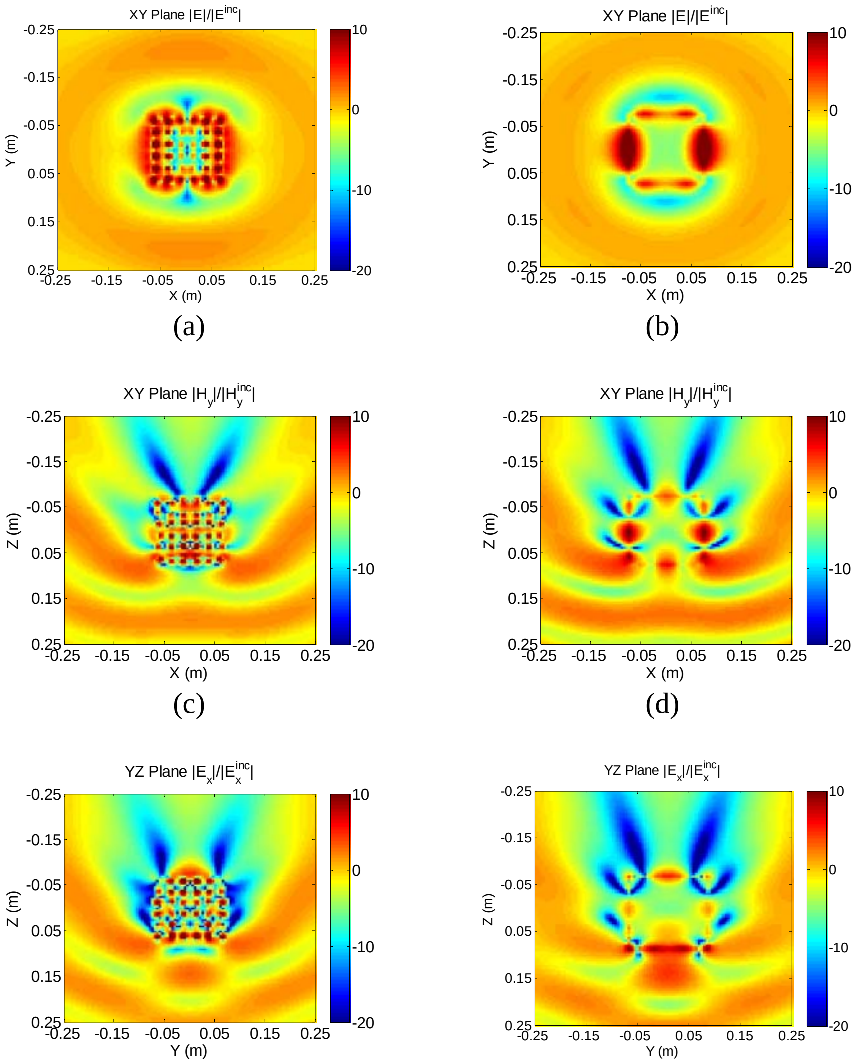

(a) (b)

(c) (d)

(e) (f)

Figure 4.4.4: The field distributions for the $6 \times 6 \times 6$ aggregated metamaterial and the corresponding homogenized metamaterial cube in the double-negative material regime. Total electric field distribution of the (a) aggregated and (b) homogenized metamaterial in the $x-y$ plane. Total magnetic field distribution of the (c) aggregated and (d) homogenized metamaterial in the $x-z$ plane. Total electric field distribution of the (e) aggregated and (f) homogenized metamaterial in the $y-z$ plane. The VV- and VH- RCS patterns for the aggregated and homogenized metamaterials in the (g) $x-z$ and (h) $y-z$ planes.

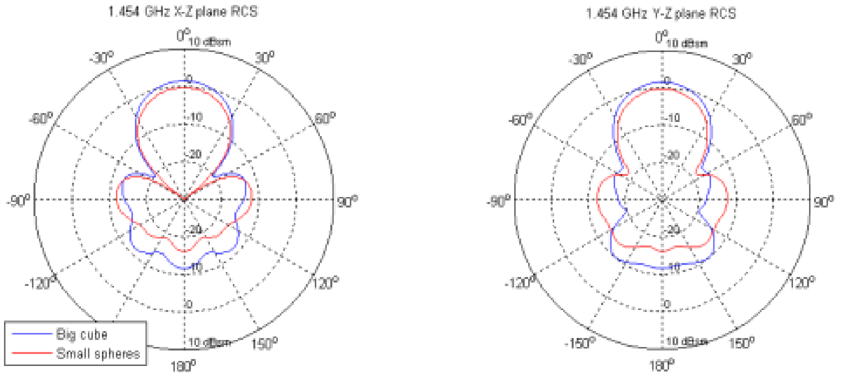

(g) (h)

Figure 4.4.4: Continued.

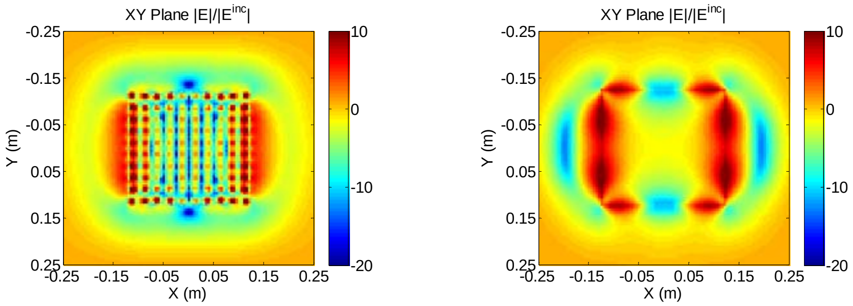

(a) (b)

Figure 4.4.5: The field distributions for the $10 \times 10 \times 10$ aggregated metamaterial and the corresponding homogenized metamaterial cube in the double-negative material regime. Total electric field distribution of the (a) aggregated and (b) homogenized metamaterial in the $x-y$ plane. Total magnetic field distribution of the (c) aggregated and (d) homogenized metamaterial in the $x-z$ plane. Total electric field distribution of the (e) aggregated and (f) homogenized metamaterial in the $y-z$ plane. The VV- and VH- RCS patterns for the aggregated and homogenized metamaterials in the (g) $x-z$ and (h) $y-z$ planes.

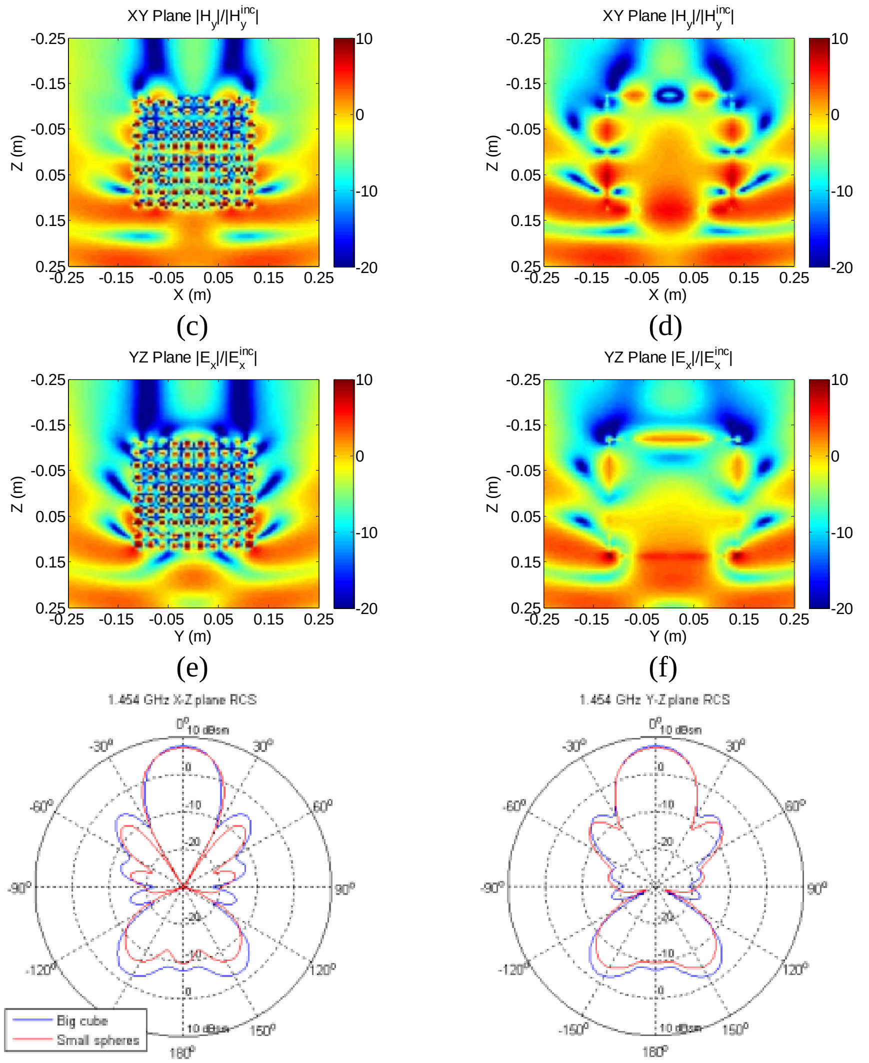

(c) (d)

(e) (f)

(g) (h)

Figure 4.4.5: Continued.

4.4.1. Computational Requirements

Next, the computational costs for simulating aggregated and homogenized metamaterials with various sizes are contrasted and detailed in Tables 4.4.1; the results show that obviously the homogenized metamaterials are much cheaper to analyze. Fig. 4.4.6 plots the matrix fill, solve time per iteration, and the memory cost as a function with respect to the problem size for the 6 metamaterial homogenization simulations. Fig.

4.4.6(a) shows that the matrix fill time scales as $O(N)$; Fig. 4.4.6(b) shows that the solve time per iteration scales as $O(N \log N)$ and Fig. 4.4.6(c) shows that the memory cost scales as $O(N)$.

Table 4.4.1: Computational requirements for the disk metamaterials

Configuration	Fill Time	Solve Time per Iteration	Number of Iterations	Memory
Aggregated	409 920 s	12 250 s	251	74.4 GB
Homogenized	3 260 s	5.56 s	1211	0.99 GB

Table 4.4.2: Computational requirements for various cubic metamaterials

Configuration		Fill Time	Solve Time per Iteration	Number of Iterations	Memory
4^3	Aggregated	14 880 s	268.2 s	606	4.61 GB
	Homogenize	404 s	0.76 s	206	0.13 GB
6^3	Aggregated	73 728 s	779.2 s	586	15.2 GB
	Homogenize	832 s	3.04 s	216	0.26 GB
10^3	Aggregated	240 832 s	9491.2 s	866	67.7 GB
	Homogenize	2 144 s	20.58 s	286	0.66 GB

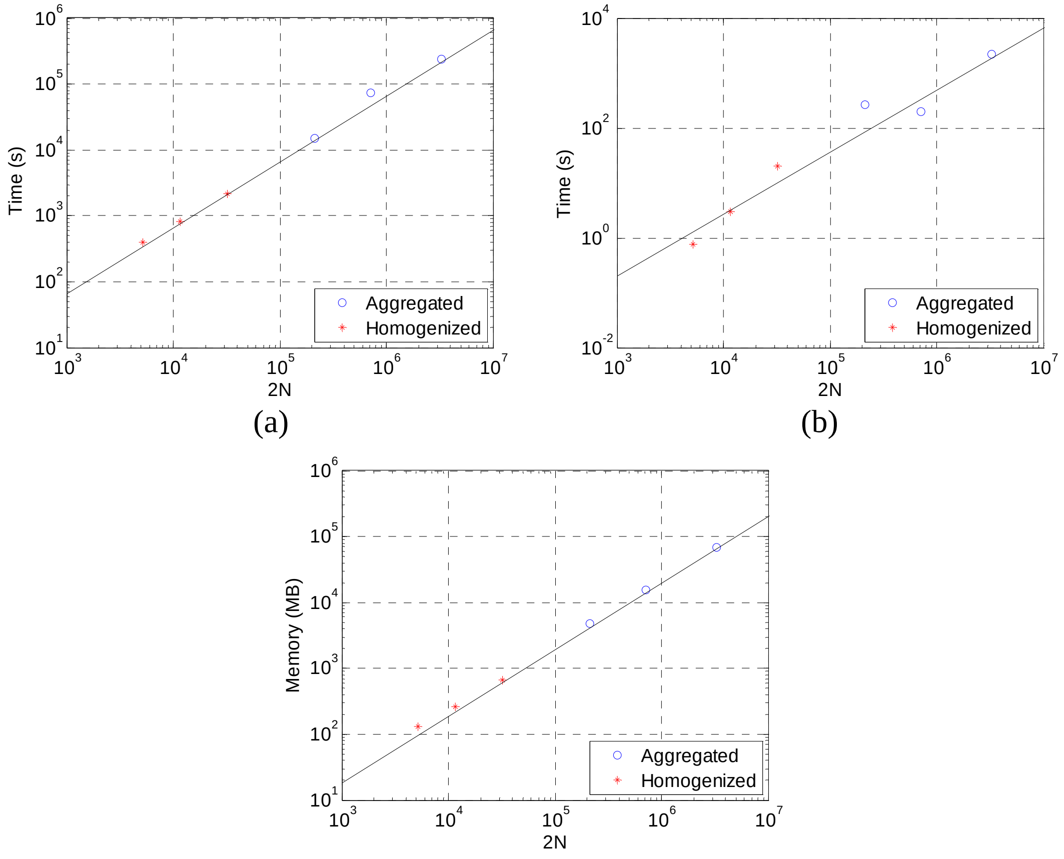

(a)

(b)

(c)

Figure 4.4.6: Computational costs for metamaterial homogenization simulations. (a) Matrix fill time. (b) Solve time per iteration. (c) Memory. The straight line is parallel to $O(N \log N)$ in (b); while that is parallel to $O(N)$ in (a) and (c).

4.4.2. Summary

This section demonstrated the applicability of the multiple-grid AIM scheme to complex scattering problems by analyzing wave scattering of large-scale aggregated spheres and the homogenized metamaterials. The results validated and quantified the accuracy of the homogenization theory for finite 3-D structures.

4.5. METAMATERIAL CLOAKING PROBLEM

In this section, the multiple-grid AIM accelerated MOM solution of CC-PMCTHWT equations is applied to a metamaterial cloaking problem. Recently, theoretical investigations [52-54] have highlighted that the scattering cancellation mechanism can be effectively used to design lossless plasmonic or metamaterial covers, which can reduce the RCS for spherical and cylindrical objects. One of the unique properties is that the reduction of RCS is insensitive to the possible losses or other imperfections in structures. This capability provides numerous potential applications, e.g, the design of low-observable targets. More recently, this approach was extended to cloak multiple objects placed in close proximity of each other, or even joined together [54], which provides a possible approach to make collections of objects transparent even when the total physical size of the system is larger than the wavelength.

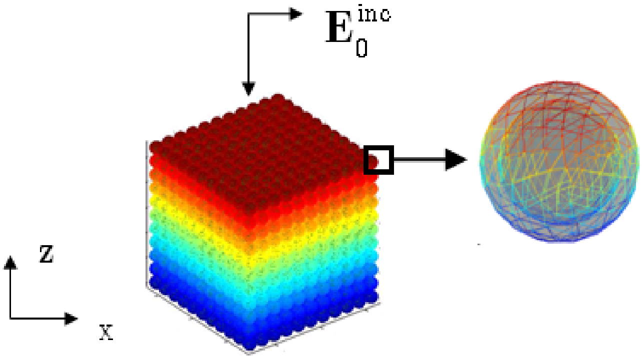

Figure 4.5.1: Configuration of the aggregated $10 \times 10 \times 10$ PEC spheres. Each sphere is coated with a thin layer of a metamaterial cloak.

Consider a three-dimensional array of PEC spheres, each of which is coated with a metamaterial cloak, as shown in Fig. 4.5.1. The PEC has a radius of $0.2\lambda_0$; the coating region has a radius of $0.218\lambda_0$; the period of spheres is $0.5\lambda_0$; the metamaterial cloaks have permittivity of $(0.1 - j0.015)\varepsilon_0$ and permeability of $5.1\mu_0$. The aggregation sizes increases from $4 \times 4 \times 4$, $8 \times 8 \times 8$, to $10 \times 10 \times 10$. These coated spheres are excited by a 120 MHz $\hat{x}$ -polarized plane wave propagating toward $-\hat{z}$. Both the PEC spheres and metamaterial cloaking surfaces are meshed by setting the average edge length to be ~ $1/10$ of the minimal wavelength. Thus, the $4\times4\times4$, $8\times8\times8$, and $10\times10\times10$ aggregated PEC spheres with metamaterial cloaking regions are meshed using $N = 69\ 888$, $N = 559\ 104$, and $N = 1\ 092\ 000$ edges, respectively; the corresponding aggregated PEC spheres without metamaterial cloaking regions require only half of them, respectively. For the aggregated spheres with cloaking regions, the spheres have $K = 129$, $K = 1025$, and $K = 2001$, different regions and thus 65, 217, and 1001 different AIM grids are used. AIM grid 0 (for the external-most region) has $N_0^{\mathrm{C}} = 60\times60\times60$, $N_0^{\mathrm{C}} = 120\times120\times120$, or $N_0^{\mathrm{C}} = 150\times150\times150$ points for the $4\times4\times4$, $8\times8\times8$, and $10\times10\times10$ case, respectively, and the rest regions are executing standard MOM calculations for all cases. For the aggregated spheres without cloaking regions, the spheres have only $K = 1$ region and thus 1 AIM grid is used. AIM grid 0 (for the external-most region) has $N_0^{\mathrm{C}} = 60\times60\times60$, $N_0^{\mathrm{C}} = 120\times120\times120$, or $N_0^{\mathrm{C}} = 150\times150\times150$ points for the $4\times4\times4$, $8\times8\times8$, and $10\times10\times10$ case, respectively.

Fig. 4.5.2-4.5.4 demonstrates the near-field distributions on the center transversal planes and RCS patterns on $x-z$ and $y-z$ planes of the $4\times4\times4$, $8\times8\times8$, and $10\times10\times10$ aggregated PEC spheres. The comparison demonstrates the metamaterial cloaking greatly weakens near-field interactions and highlights the significant reduction in RCS: The total RCS of $4\times4\times4$, $8\times8\times8$, and $10\times10\times10$ PEC spheres are 11.09 dB, 18.63 dB, and 20.69 dB; whereas the total RCS for the corresponding coated PEC spheres are -0.89 dB, 7.70 dB, and 10.18 dB; the metamaterial cloaking achieves a reduction of total RCS by 93.7%, 91.92%, and 91.09%, respectively. These numerical results validate that the scattering cancellation mechanism can be effectively extended to cloak multiple objects even when the total physical size of the system is larger than multiple wavelengths (the physical size of the $10\times10\times10$ array is more than 5 wavelengths).

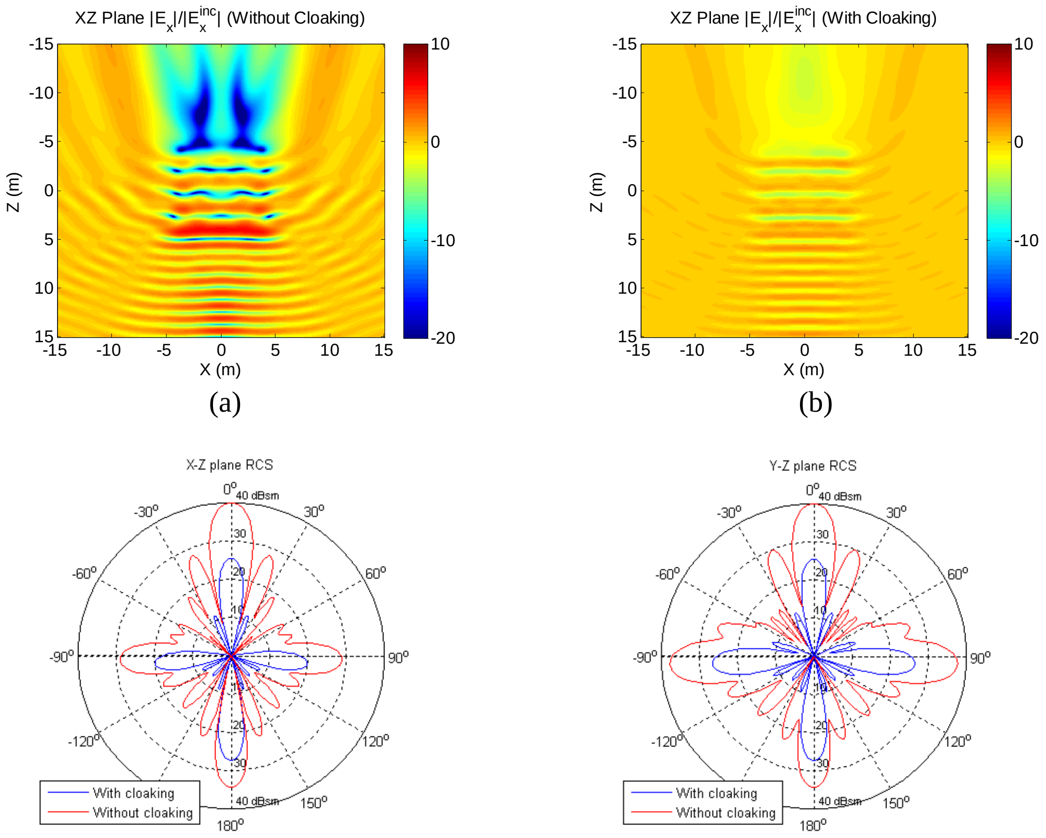

(a) (b)

(c) (d)

Figure 4.5.2: The field distributions for the $4\times4\times4$ aggregated PEC spheres without and with metamaterial cloaking. Total electric field distribution of the (a) PEC spheres and (b) PEC spheres with metamaterial cloaking in the $x-z$ plane. The VV- and VH- RCS patterns for the PEC spheres without and with metamaterial cloaking in the (c) $x-z$ and (d) $y-z$ planes.

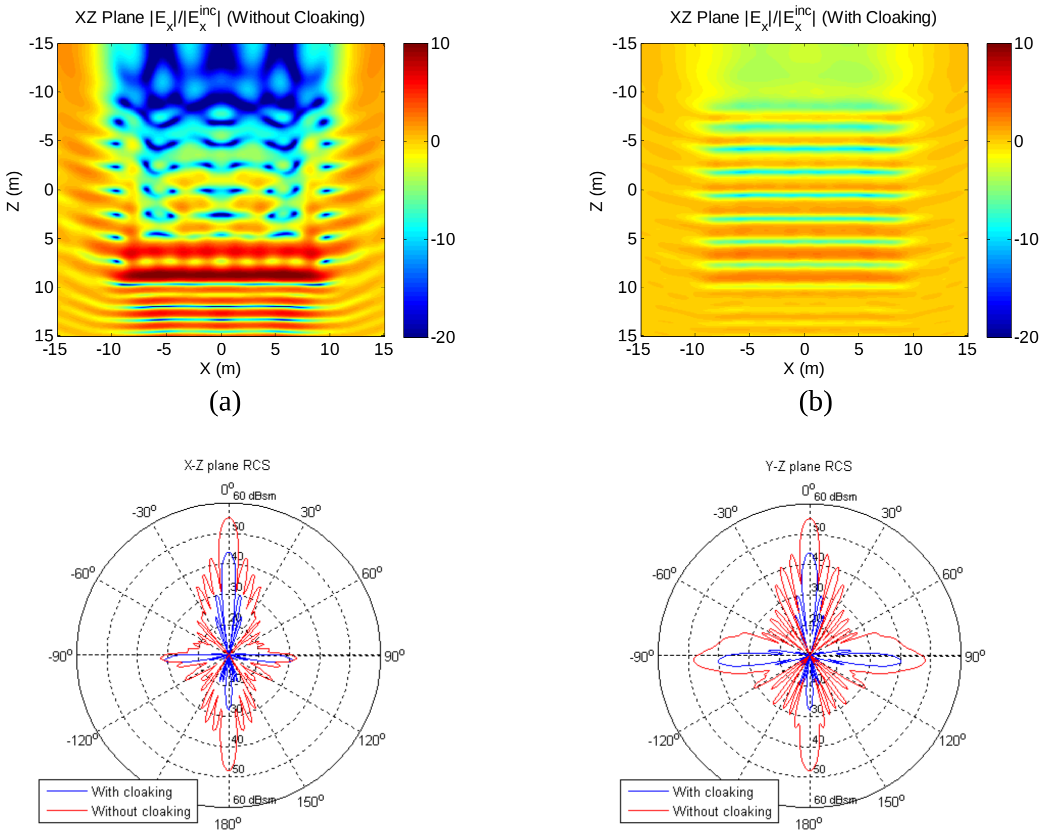

(a) (b)

(c) (d)

Figure 4.5.3: The field distributions for the $8 \times 8 \times 8$ aggregated PEC spheres without and with metamaterial cloaking. Total electric field distribution of the (a) PEC spheres and (b) PEC spheres with metamaterial cloaking in the $x-z$ plane. The VV- and VH- RCS patterns for the PEC spheres without and with metamaterial cloaking in the (c) $x-z$ and (d) $y-z$ planes.

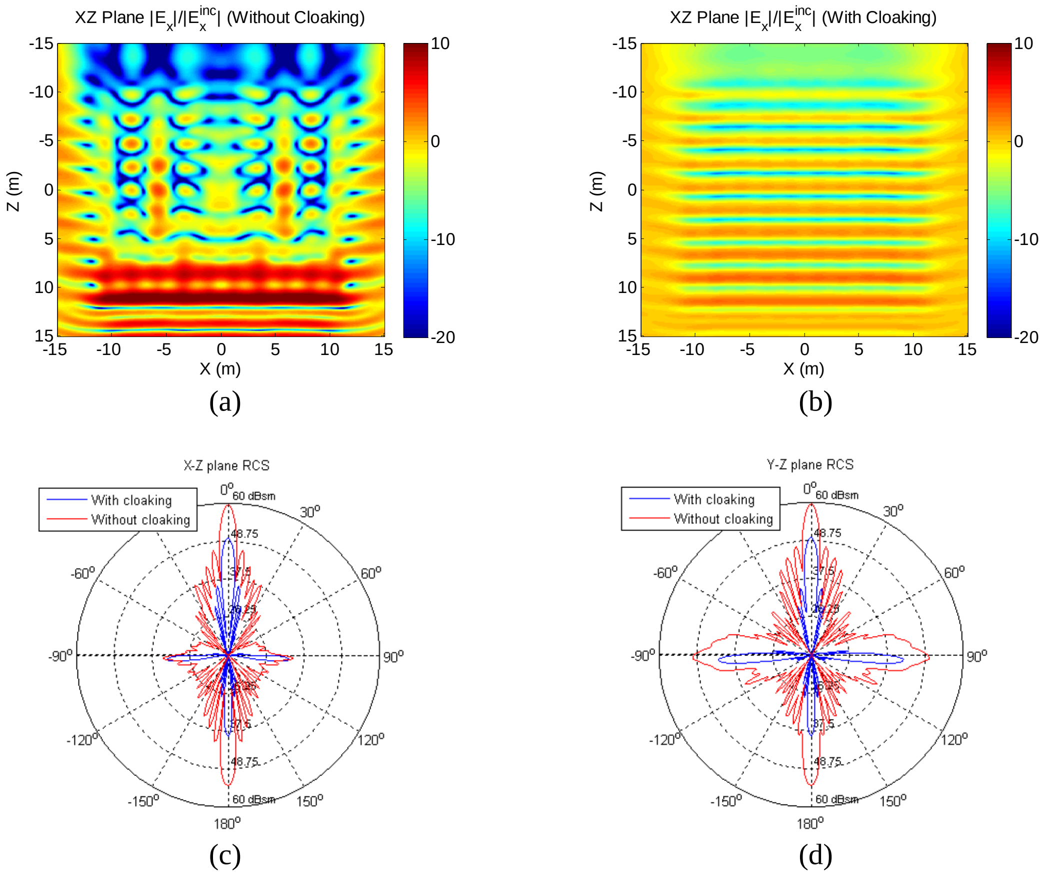

(a) (b)

(c) (d)

Figure 4.5.4: The field distributions for the $10\times10\times10$ aggregated PEC spheres without and with metamaterial cloaking. Total electric field distribution of the (a) PEC spheres and (b) PEC spheres with metamaterial cloaking in the $x-z$ plane. The VV- and VH- RCS patterns for the PEC spheres without and with metamaterial cloaking in the (c) $x-z$ and (d) $y-z$ planes.

4.5.1. Computational Requirements

The computational costs for simulating PEC spheres with or without cloaking are contrasted and detailed in Table 4.5.1; the results show that the cloaking regions increase the problem sizes; therefore, increases all costs, i.e. the matrix fill time, matrix solve time per iteration, number of iterations, and memory requirement. Fig. 4.5.5 plots the matrix fill, solve time per iteration, and the memory cost as a function with respect to the problem size for the 6 metamaterial cloaking simulations. Fig. 4.5.5(a) shows that the matrix fill time scales as $O(N)$; Fig. 4.5.5(b) shows that the solve time per iteration scales as $O(N \log N)$, and Fig. 4.5.5(c) shows that the memory cost scales as $O(N)$ for all simulations, and adding the cloaking regions almost double the memory cost.

Table 4.5.1: Computational requirements for the various PEC spheres

Configuration		Fill Time	Solve Time per Iteration	Number of Iterations	Memory
4^3	Without cloaking	1 368 s	6.4 s	21	0.92 GB
	With cloaking	9 136 s	22.8 s	81	3.19 GB
8^3	Without cloaking	13 080 s	710 s	106	5.76 GB
	With cloaking	72 740 s	2 260 s	141	24.9 GB
10^3	Without cloaking	21 384 s	1 242 s	151	12.9 GB
	With cloaking	142 740 s	4 417 s	181	51.5 GB

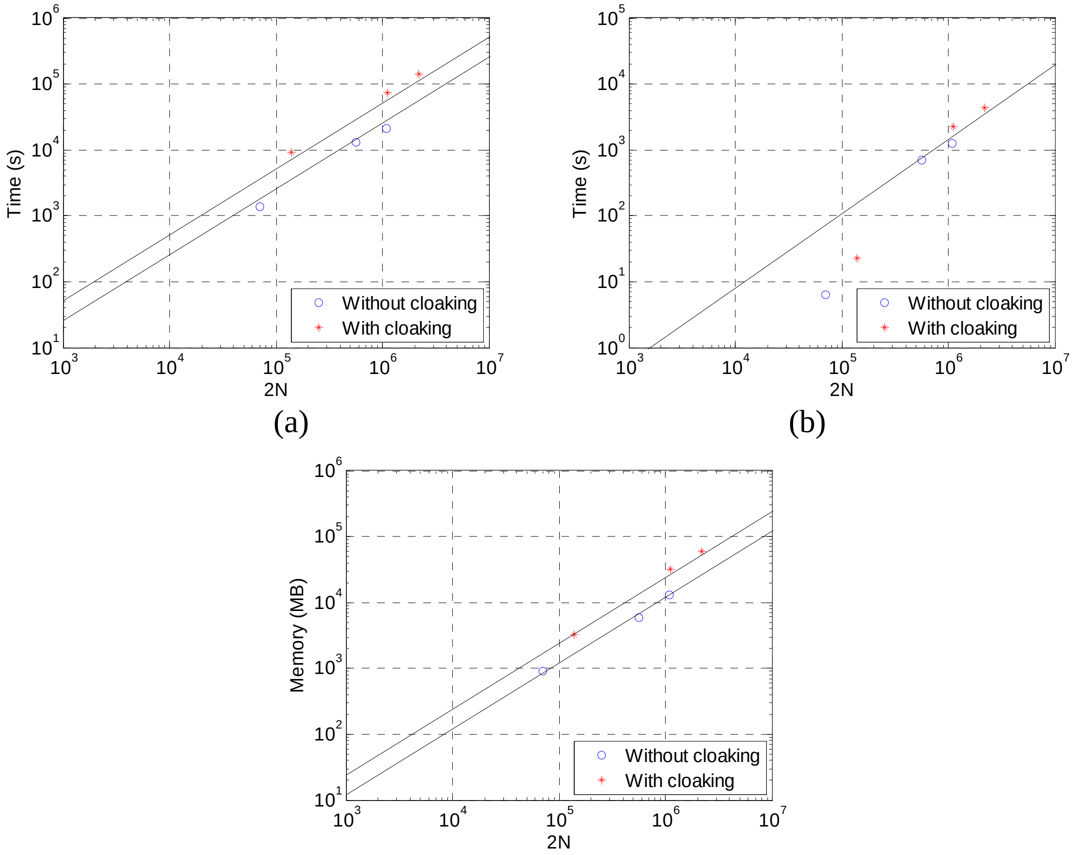

(a) (b)

(c)

Figure 4.5.5: Computational costs for metamaterial cloaking simulations as the number of spheres is increased from 64 to 1000. (a) Matrix fill time. (b) Solve time per iteration. (c) Memory. The straight line is parallel to $O(N \log N)$ in (b); while that is parallel to $O(N)$ in (a) and (c).

4.5.2. Summary

This section demonstrated the applicability of the multiple-grid AIM scheme to complex scattering problems by analyzing wave scattering from PEC spheres with metamaterial cloaks. The simulation results highlight the potential of metamaterial cloaks for reducing scattering from a collection of thousands of small objects whose total physical size are multiple wavelengths.

Chapter V Conclusions

This dissertation presented a fast electromagnetic solver for the analysis of scattering from general large-scale composite structures. The solver's efficiency is derived from the multiple-grid AIM scheme for accelerating the iterative MOM solution and the better-conditioned combined-field type surface integral equations. The proposed solver was first presented in detail for piecewise homogeneous structures composed of magnetodielectric regions. It was then extended to account for several other structures that are encountered in practical scenarios; extensions were presented for PEC/PMC regions, an infinite PEC/PMC plane, metamaterial regions, and material-PEC junctions. The multiple-grid AIM employs multiple auxiliary grids that have different locations, grid spacings, and associated projection, propagation, and interpolation operators that can be independently optimized for computations relevant to each piecewise homogeneous region. The better conditioned CC-PMCHWT equations generally double the matrix fill time, slightly increase the matrix solve time and memory requirement, but yield faster convergence than EH-PMCHWT ones. A variety of complex applications—including wave propagation in natural forested environments, design of metamaterials, and application of metamaterials to radar cross section reduction—were presented to validate the proposed solver's accuracy and efficiency and to demonstrate its generality, practicality, and usefulness for complex electromagnetic engineering problems.

The multiple-grid AIM scheme is most effective for piecewise homogeneous structures composed of regions with small changes in their constitutive parameters, i.e., low-contrast problems. The method is less effective, however, for high-contrast problems that have large variations in mesh density and edge lengths on the surfaces bounding the piecewise homogeneous regions. This is a limitation of the AIM directly stemming from its reliance on a single uniform grid in each region. Two- and multi-scale extensions of the algorithm that are in development can potentially overcome this limitation by introducing multiple (multi-scale) grids in each region [55].

As demonstrated in this thesis, the improvement from CC-PMCHWT equations, while significant, is problem dependent. Moreover, the accuracy of CC-PMCHWT-based solvers might be degraded by the high-order singularity present in the Green functions of the rotated integral equations. This inaccuracy problem of the CC-PMCHWT equations can be significant for piecewise homogeneous structures with recursive regions, e.g., layered spheres, as the interactions between the disjoint surfaces of two neighboring layers are strong. One way to potentially overcome this limitation is to introduce curl-conforming testing functions for the rotated integral equations so that the high-order singularity can be eliminated by moving the curl-operation onto the testing functions [56, 57]. In the mean time, the practical implementation of methods for solving these equations should keep the option of reverting back to EH-PMCHWT equations for validation and comparison. Fortunately, this is rather easily accomplished as the CC-PMCHWT equations can be easily reduced to the EH-PMCHWT ones.

Reference

[1] Y. Li, M.-F. Wu, A. E. Yılmaz, and H. Ling, “Investigation of short-range radiowave propagation at HF/VHF frequencies in a forested environment,” *IEEE Antennas and Wireless Propagat. Lett.,* vol. 8, pp. 1182-1185, 2009.

[2] H. C. Strifors and G. C. Gaunaurd, "Scattering of electromagnetic pulses by simple-shaped targets with radar crosssection modified by a Dielectric Coating," *IEEE Trans. Antennas Propagat.*, vol. 46, no. 9, pp. 1252-1262, Sep. 1998.

[3] A. Alu and N. Engheta, "Polarizabilities and effective parameters for collections of spherical nanoparticles formed by pairs of concentric double-negative, single-negative, and/or double-positive metamaterial layers," *J. Appl. Phys.*, vol. 97, no. 9, p. 094310, May 2005.

[4] E. K. Miller, "A selective survey of computational electromagnetics," *IEEE Trans. Antennas Propagat.,* vol. 36, no. 9, pp. 1281-1305, Sep. 1988.

[5] A. J. Poggio and E. K. Miller, *Integral Equation Solution of Three Dimensional Scattering Problems*. Elmsford, NY: Permagon, 1973.

[6] Y. Chang and R. F. Harrington, "A surface formulation for characteristic modes of material bodies," *IEEE Trans. Antennas Propagat.*, vol. 25, no. 6, pp. 789-795, Nov. 1977.

[7] T. K. Wu and L. L. Tsai, "Scattering from arbitrarily-shaped lossy dielectric bodies of revolution," *Radio Sci.*, vol. 12, no. 5, pp. 709-718, Sep.-Oct. 1977.

[8] E. Bleszynski, M. Bleszynski, and T. Jaroszewicz, "AIM: Adaptive integral method for solving large-scale electromagnetic scattering and radiation problems," *Radio Sci.*, vol. 31, no. 5, pp. 1225-151, Sep./Oct. 1996.

[9] E. Topsakal, M. Carr, J. Volakis, and M. Blezsynski, "Galerkin operators in adaptive integral method implementations," *Proc. Microwaves Antennas Propagat.*, vol. 148, no. 2, pp. 79-84, Apr. 2001.

[10] X. C. Nie, L. W. Li, N. Yuan, T. S. Yeo, and Y. B. Gan, "A fast analysis of electromagnetic scattering by arbitrarily shaped homogeneous dielectric objects," *Microwave Opt. Tech. Lett.*, vol. 38, no. 1, pp. 30-35, July 2003.

[11] W.-J. Zhao, L.-W. Li, and Y.-B. Gan, "Efficient analysis of antenna radiation in the presence of airborne dielectric radomes of arbitrary shape," *IEEE Trans. Antennas Propagat.*, vol. 53, no. 1, pp. 442-449, Jan. 2005.

[12] M. A. Carr, E. Topsakal, J. L. Volakis, and D. C. Ross, "Adaptive integral method applied to multilayer penetrable scatterers with junctions," in *Proc. IEEE Antennas Propagat. Soc. Int. Symp.*, July 2001, pp. 858-861.

[13] P. Yla-Oijala and M. Taskinen, "Application of combined field integral equation for electromagnetic scattering by dielectric and composite objects," *IEEE Trans. Antennas Propagat.*, vol. 53, no. 3, pp. 1168-1173, Mar. 2005.

[14] P. Yla-Oijala, M. Taskinen, and S. Jarvenpaa, "Surface integral equation formulations for solving electromagnetic scattering problems with iterative methods," *Radio Sci.*, vol. 40, p. RS6002, Nov. 2005.

[15] A. E. Yılmaz, J.-M. Jin, and E. Michielssen, "A stable time-domain integral equation formulation for composite structures," in *Proc. IEEE Antennas Propagat. Soc. Int. Symp.*, July 2006, pp. 2963-2966.

[16] O. Ergul and L. Gurel, "Efficient solutoin of the electric and magnetic current combined-field integral equation with the multilevel fast multipole algorithm and block-diagonal preconditioning," *Radio Sci.*, vol. 44, p. RS6001, Nov. 2009.

[17] R. S. Chen, Y. Q. Hu, Z. H. Fan, D. Z. Ding, D. X. Wang, and K. N. Yung,"An efficient surface integral equation solution to EM scattering by chiral objects above a lossy half space," *IEEE Trans. Antennas Propagat.*, vol. 57, no. 11, pp. 3586-3593, Nov. 2009.

[18] J. Rivero, J. M. Taboada, L. Landesa, F. Obelleiro, and I. Garcia-Tunon, “Surface integral equation formulation for the analysis of left-handed metamaterials,” *Opt. Exp.*, vol. 18, no. 15, pp. 15876-15886, 2010.

[19] J. M. Putnam and L. N. Medgyesi-Mitschang, "Combined field integral equation formulation for inhomogeneous two- and three-dimensional bodies: the junction problem," *IEEE Trans. Antennas Propagat.*, vol. 39, no. 5, pp. 667-672, May 1991.

[20] L. N. Medgyesi-Mitschang, J. M. Putnam, and M. B. Gedera, "Generalized method of moments for three-dimensional penetrable scatterers," *J. Opt. Soc. Am. A*, vol. 11, no. 4, pp. 1383-1398, Apr. 1994.

[21] P. Yla-Oijala, M. Taskinen, and J. Sarvas, "Surface integral equation method for general composite metallic and dielectric structures with junctions," *Prog. Electromagn. Res.*, vol. 52, pp. 81-108, 2005.

[22] M. Carr, E. Topsakal, and J. L. Volakis, "A procedure for modeling material junctions in 3-D surface integral equation approaches," *IEEE Trans. Antennas Propagat.*, vol. 52, no. 5, pp. 1374-1379, May 2004.

[23] M. F. Wu, G. Kaur, and A. E. Yilmaz, “A multiple-grid adaptive integral method for multi-region problems,” *IEEE Trans. Antennas Propagat.*, vol. 58, no. 5, pp. 1601-1613, May 2010.

[24] S. M. Rao, D. R. Wilton, and A. W. Glisson, "Electromagnetic scattering by surfaces of arbitrary shape," *IEEE Trans. Antennas Propagat.*, vol. 30, no. 3, pp. 409-418, May 1982.

[25] A. E. Yılmaz, J.-M. Jin, and E. Michielssen, "Time domain adaptive integral method for surface integral equations," *IEEE Trans. Antennas Propagat.,* vol. 52, no. 10, pp. 2692-2708, Oct. 2004.

[26] X. C. Nie, L. W. Li, and N. Yuan, "Precorrected-FFT algorithm for solving combined field integral equations in electromagnetic scattering," *J. Electromagn. Waves Appl.,* vol. 16, no. 8, pp. 1171-1187, 2002.

[27] D. Wulf and R. Bunger, "An efficient implementation of the combined wideband MLFMA/LF-FIPWA," *IEEE Trans. Antennas Propagat.,* vol. 57, no. 2, pp. 467-474, Feb. 2009.

[28] M. F. Wu, K. Yang, and A. E. Yilmaz, "Efficient incorporation of a PEC/PMC plane in the multiple-grid adaptive integral method," *IEEE Trans. Antennas Propagat.*, vol. 59, no. 1, pp. 314-319, Jan. 2011.

[29] X. Millard, and Q. H. Liu, "A fast volume integral equation solver for electromagnetic scattering from large inhomogeneous objects in planarly layered media," *IEEE Trans. Antennas Propagat.*, vol. 51, no. 9, pp. 2393-2401, Sep. 2003.

[30] J. R. Philllips, Ph.D. Dissertation, MIT, 1997.

[31] N. Engheta and R. W. Ziolkowski, "A positive future for double-negative metamaterials," *IEEE Trans. Microw. Theory Tech.*, vol. 53, no. 4, pp. 1535–1556, 2005.

[32] M. F. Wu, X. X. Liu, A. Alu, and A. E. Yilmaz, "A surface integral equation fast solver for composite structures with metamaterial regions," in *Proc. IEEE Antennas Propagat. Soc. Int. Symp.*, July 2011, pp. 2688-2691.

[33] W. C. Chew, "Some reflections on double negative materials," *Prog. Electromagn. Res.*, vol. 51, pp. 1–26, 2005.

[34] Y. A. Liu and W. C. Chew, "Stability of surface integral equation for left-handed materials," *IET Microw. Antennas Propag.,* vol. 1, no. 1, pp.84-89, 2007.

[35] D. L. Smith, L. N. Medgyesi-Mitschang, and D. W. Forester, "Surface integral equation formulations for left-handed materials," *Prog. Electromagn. Res.*, vol. 51, pp. 27-48, 2005.

[36] A. Herschlein, J. V. Hagen, and W. Wiesbeck, "A generalized integral equation formulation for mixed dielectric-PEC scatters," *Radio Sci.,* vol. 37, no.4, p. 1058, July 2002.

[37] Y. Lin, J.-H. Lee, J. Liu, M. Chai, J. A. Mix, and Q. H. Liu, "A hybrid SIM-SEM method for 3D electromagnetic scattering problems," *IEEE Trans. Antennas Propag.*, vol. 57, no. 11, pp. 3655–3663, Nov. 2009.

[38] X. Q. Sheng, J.-M. Jin, J. Song, and W. C. Chew, "Solution of combined-field integral equation using multilevel fast multipole algorithm for scattering by homogeneous bodies," *IEEE Trans. Antennas Propagat.*, vol. 46, no. 11, pp. 1718-1726, Nov. 1998.

[39] Y. Li and H. Ling, "Investigation of Wave Propagation in a Dielectric Rod Array," *IEEE Trans. Antennas Propagat.*, vol. 58, no. 12, pp. 4025-4032, Dec. 2010.

[40] Y. Ziade, H. Roussel, M. Lesturgie, and W. Tabbara, "A coherent model of forest propagation application to detection and localization of targets using the DORT method," *IEEE Trans. Antennas Propagat.*, vol. 56, no. 4, pp. 1048-1057, Apr. 2008.

[41] L. Li, Z. Liu, X. Dong, and L. Carin, "MLFMA analysis of scattering from multiple target in the presence of a half-space," *IEEE Trans. Antennas Propagat.*, vol. 51, no. 4, pp. 810-819, Apr. 2003.

[42] "*Wood Handbook—Wood as an Engineering Material*". Gen. Tech. Rep., FPL-GTR-113, Madison, WI, U.S. Dept. of Agriculture, Forest Services, Forest Products Laboratory, Mar. 1999.

[43] L.-W. Li, J.-H. Koh, T.-S. Yeo, K.-S. Leong, and P.-S. Kooi, "Analysis of radiowave propagation in a four-layered anisotropic forest environment," *IEEE Trans. Antennas Propagat.*, vol. 37, no. 4, pp. 1967-1979, July 1999.

[44] A. Clark III, “Characteristics of timber stands containing sufficient heartwood for cavity excavation by red-coackaded woodpecker clans,” in *Proc. 7th Biennial South. Silvicult. Res. Conf.*, Nov. 1992, pp. 621-626.

[45] G. I. Torgovnikov, *Dielectric Properties of Wood and Wood-Based Materials*. NY: Springer-Verlag, 1993.

[46] E. S. Kasischke, N. L. Christensen Jr., and E. M. Haney, “Modeling of geometric properties of loblolly pine tree and stand characteristics for use in radar backscatter studies,” *IEEE Trans. Geosci. Remote Sensing*, vol. 32, no. 4, pp. 800-822, July 1994.

[47] E. Lier, D. H. Werner, C. P. Scarborough, Q. Wu and J. A. Bossard, “An octave-bandwidth negligible-loss radiofrequency metamaterial,” *Nature Materials*, vol. 10, no. 3, pp.216-222, Jan. 2011.

[48] Z. Liu, H. Lee, Y. Xiong, C. Sun, and X. Zhang, “Far-field optical hyperlens magnifying sub-diffraction-limited objects,” *Science*, vol. 315, no. 5819, pp. 1686-1686, Mar. 2007.

[49] A. Alù, “Restoring the physical meaning of metamaterial constitutive parameters,” *Phys. Rev. B*, vol. 83, no. 8, p. 081102, Feb. 2011.

[50] A. Alù, “First-principle homogenization theory for periodic metamaterial arrays,” *Phys. Rev. B*, in press.

[51] X. X. Liu, M. F. Wu, A. Yilmaz, and A. Alu, "Homogenization of metamaterials and far field radiation," in preparation.

[52] A. Alù and N. Engheta, “Achieving transparency with plasmonic and metamaterial coatings,” *Phys. Rev. E*, vol. 72, no, 1, p. 016623, July 2005.

[53] A. Alù, and N. Engheta, “Plasmonic materials in transparency and cloaking problems: mechanism, robustness, and physical insights,” *Opt. Express*, vol. 15, no. 6, pp. 3318-3332, Mar. 2007.

[54] A. Alù, and N. Engheta, “Cloaking and transparency for collections of particles with metamaterial and plasmonic,” *Opt. Express*, vol. 15, no. 12, pp. 7578-7590, June 2007.

[55] A. E. Yılmaz, “A two-scale AIM for fast solution of volume integral equations,” in *Proc. Appl. Comp. Electromagnetics Symp.*, Mar. 2009, pp. 511–516.

[56] S. Yan, J.-M. Jin, and Z. Nie, "On the Testing of the Identity Operator and the Accuracy Improvement of the Second-Kind SIEs," in *Proc. IEEE Antennas Propagat. Soc. Int. Symp.*, July 2011, pp. 1-4.

[57] K. Cools, F. P. Andriulli, D. De Zutter, and E. Michielssen, "Accurate and conforming mixed Discretization of the MFIE," *IEEE Antennas and Wireless Propagat. Lett.*, vol. 10, pp. 528-531, 2011.

Publication

Journal Papers

[1] X. X. Liu, **M. F. Wu**, A. E. Yilmaz, and A. Alu, "Homogenization of metamaterials and far field radiation," in preparation.

[2] **M. F. Wu**, and A. E. Yilmaz, “A fast and well-conditioned integral equation solver for composite structures,” in preparation.

[3] **M. F. Wu**, K. Yang, and A. E. Yilmaz, “Efficient incorporation of a PEC/PMC plane in the multiple-grid adaptive integral method,” *IEEE Trans. Antennas Propagat.*, vol.59, no.1, pp. 314-319, Jan. 2011.

[4] **M. F. Wu**, G. Kaur, and A. E. Yilmaz, “A multiple-grid adaptive integral method for multi-region problems,” *IEEE Trans. Antennas Propagat.*, vol. 58, no. 5, pp. 1601-1613, May 2010.

[5] Y. Li, **M. F. Wu**, A. E. Yilmaz, and H. Ling, “Investigation of short-range radiowave propagation at HF/VHF frequencies in a forested environment,” *IEEE Antennas Wireless Propagat. Lett.*, vol. 8, pp. 1182-1185, 2009.

[6] **M. F. Wu**, F.-Y. Meng, Q. Wu, J. Wu and J.-C. Lee, "An approach for small omnidirective microstrip antenna based on the backward wave property of the double negative medium substrate," *Applied Physics A: Material Science & Processing*, vol. 87, no. 2, pp. 193-198, 2007.

[7] **M. F. Wu**, F.-Y. Meng, J.-H. Fu, Q. Wu, and J. Wu, "Novel miniaturized planar left-handed metamaterial transmission lines verified by the backward wave property," *Acta Physica Sinica*, Vol. 57, No. 2, pp. 822-826, 2008.

[8] Q. Wu, F.-Y. Meng, **M. F. Wu**, and L.-W. Li, “A new approach to the analysis of macro effect of the wires array in metamaterial,” *Acta Electronica Sinica*, Vol. 35, No. 8, pp. 1472-1475, 2007.

[9] **M. F. Wu**, F.-Y. Meng, Q. Wu, and J. Wu, “Investigation on the Miniaturization of the Microstrip Antenna Based on the Backward Wave Property of Left-Handed Medium,” *Acta Physica Sinica*, Vol. 55, No. 12, pp. 6368-6373, 2006.

[10] **M. F. Wu**, F.-Y. Meng, Q. Wu, and J. Wu, “Design of Left-Handed Microstrip Based on DGS and Double Layers SRRs Structures,” *Acta Physica Sinica*, Vol. 55, No. 11, pp.5790-5794, 2006.

[11] Q. Wu, **M. F. Wu**, F.-Y. Meng, J. Wu, and L.-W. Li, “Research on the SRR LHM Based on Transmission Line Theory,” *Chinese Journal of Radio Science*, Vol. 21, No. 3, pp. 310-314, 2006.

Conference Abstracts and Presentations

[1] **M. F. Wu** and A. E. Yilmaz, "A well-conditioned multiple-grid AIM-accelerated PMCHWT solver for composite structures," *USNC/URSI*, Toronto, July 2010.

[2] Y. Li, **M. F. Wu**, A. E. Yilmaz, and H. Ling, "Analysis of wave propagation mechanisms in large-scale dielectric rod arrays," *USNC/URSI*, Washington, July 2011.

[3] **M. F. Wu**, K. Yang, and A. E. Yilmaz, "Efficient incorporation of PEC/PMC planes in the multiple-grid adaptive integral method," *USNC/URSI*, June 2009.

Extended Papers in Conference Proceedings

[1] **M. F. Wu**, X. X. Liu, A. Alu, and A. E. Yilmaz, "A surface integral equation fast solver for composite structures with metamaterial regions," *IEEE AP-S*, Washington, July 2011.

[2] Q. Wu, **M. F. Wu**, F.-Y. Meng, and L.-W. Li, “A Double Negative Medium Supporting Backward Waves with Application to Microstrip Antennas,” *International Symposium on Antennas and Propagation*, Singapore, Nov. 2006.

[3] Q. Wu, **M. F. Wu**, F.-Y. Meng, J. Wu and L.-W. Li, “A Novel Broadband Double Negative Medium Substrate Design for Microstrip Antenna Miniaturization,” *IEEE AP-S and USNC/URSI*, New Mexico, USA, July 2006.

[4] Q. Wu, F.-Y. Meng, **M. F. Wu**, J. Wu and L.-W. Li, “Design of Planar LHM with Broadband and Miniaturized Cell,” *IEEE AP-S and USNC/URSI*, New Mexico, USA, July 2006.

[5] Q. Wu, **M. F. Wu**, F.-Y. Meng, J. Wu, and L.-W. Li, “Modeling the Effects of an Individual SRR by Equivalent Circuit Method,” *IEEE AP-S and USNC/URSI*, Washington, DC, USA, July 2005.

[6] Q. Wu, F.-Y. Meng, **M. F. Wu**, J. Wu, and L.-W. Li, “Research on the Macro Effect of the Thin Wire Array in Metamaterial by Equivalent Circuit Method,” *IEEE AP-S and USNC/URSI*, Washington, DC, USA, July 2005.

[7] **M. F. Wu**, F.-Y. Meng, Q. Wu, J. Wu and L.-W. Li, “Miniaturization of a Patch Antenna with Dispersive Double Negative Medium Substrates,” *Asia-Pacific Microwave Conference*, Suzhou, China, Dec. 2005.

[8] **M. F. Wu**, F.-Y. Meng, Q. Wu, J. Wu and L.-W. Li, “A Compact Equivalent Circuit Model for the SRR Structure in Metamaterials,” *Asia-Pacific Microwave Conference*, Suzhou, China, December 2005.

[9] F.-Y. Meng, **M. F. Wu**, Q. Wu, J. Wu and L.-W. Li, “Analysis and Calculation of Effective Permittivity for a Left-Handed Metamaterial,” *Asia-Pacific Microwave Conference*, Suzhou, China, December 2005.

[10] **M. F. Wu**, F.-Y. Meng, Q. Wu, J. Wu and L.-W. Li, “SRRs’ Artificial Magnetic Metamaterials Modeling Using Transmission Line Theory,” *PIERS*, Hangzhou, China, August 2005.

[11] F.-Y. Meng, Q. Wu, **M. F. Wu**, J. Wu and L.-W. Li, “Research on the Negative Permittivity Effect of the Thin Wires Array in Metamaterial by Transmission Line Theory,” *PIERS*, Hangzhou, China, August 2005.

Vita

Mingfeng Wu was born in Jiangxi province, China in 1983. He received the Bachelor of Engineering and Master of Science degrees both in electrical engineering from Harbin Institute of Technology, Harbin, China, in July 2005 and July 2007, respectively. He started graduate studies at the University of Texas, Austin, TX in 2007.

His current research interests include computational electromagnetics, electromagnetic periodic structures, and wave propagation and scattering.

Permanent Address: 3607 Greystone Dr, APT. 1021
Austin, TX, 78731

This thesis was typed by the author.